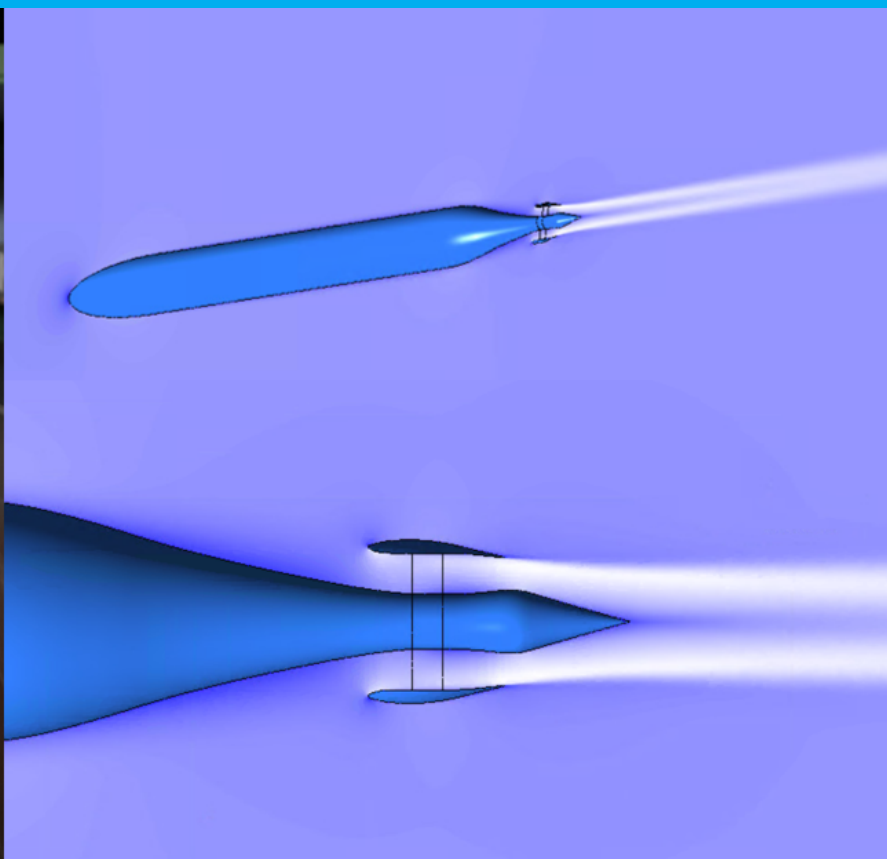
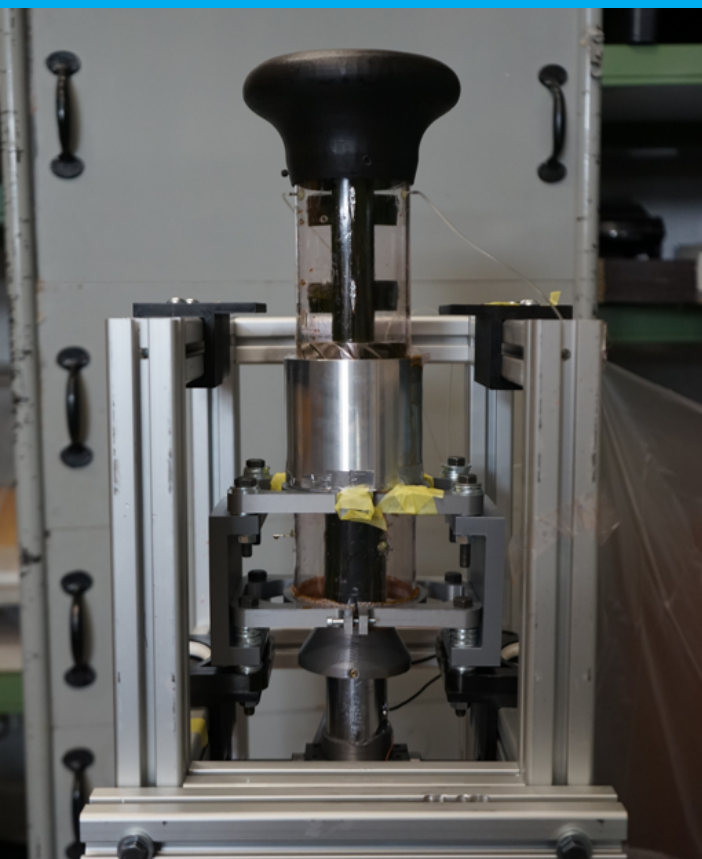


The Effect of Fan Performance in a Propulsive Fuselage Con- cept Configuration

A combined experimental and
numerical investigation

E.M. Raijmakers



The Effect of Fan Performance in a Propulsive Fuselage Concept Configuration

A combined experimental and numerical investigation

by

E.M. Raijmakers

in partial fulfilment of the requirements for the degrees of
Master of Science
In Aerospace Engineering
at the Delft University of Technology,
to be defended publicly on Friday November 12th, 2021 at 9:30 AM.

Student number: 4297032
Thesis committee: dr. A. Gangoli Rao, TU Delft, supervisor
Prof. dr. ing. G. Eitelberg, TU Delft
dr. D. Ragni, TU Delft

An electronic version of this thesis is available at <http://repository.tudelft.nl/>.

Preface

This thesis has been written in partial fulfilment of the requirements for the degrees of Master of Science in Aerospace Engineering.

The thesis work has been like a genuine relationship, including all its ups and downs, where I learned a lot about the topic and even more about myself.

I would like to thank Arvind Gangaoli Rao for many discussions over coffee and for his many motivational speeches. My thanks also go out to Biagio Della Corte who has supported me in and outside the lab and has been available for many discussions which definitely helped me a lot. Another personal thank you goes out to Martijn van Sluis who helped out in taming ANSYS fluent. Moreover, I would also like to thank the staff of the FPP group for their sharp and justified feedback on my work and the personnel of the LTT for their help and flexibility during my experimental campaigns.

Aside from the TU Delft staff, I also need to thank my family and friends. I want to thank my parents and my sister for always listening to my talk about work with enthusiasm. My urban family has also supported me a lot; I want to thank Niek and Bas for many motivational words. A special mention goes out to my four-legged friends Loeki and Sky for conversations on science and progress. Last but not least, a massive thank you goes out to my significant other, Pieter, who always believes in me.

*E.M. Raijmakers
Delft, October 2021*

Contents

List of Figures	vii
List of Tables	xi
Nomenclature	xiii
Abstract	xvii
1 Introduction	1
1.1 Previous Research on Boundary Layer Ingestion.	1
1.2 Research Motivation & Objective	3
1.3 Thesis Outline	5
2 Theoretical Background	7
2.1 Boundary Layer Ingestion Theory.	7
2.2 Power Balance Method.	11
3 Uninstalled Fan Test Rig	17
3.1 Purpose	17
3.2 Experimental Setup	18
3.3 Measurement Techniques	21
3.3.1 Scaling Parameters	22
3.3.2 Instrumentation	24
4 Uninstalled Fan Performance	25
4.1 Fan Behaviour	25
4.2 Azimuthal Variation	28
4.3 Installation Effects	28
4.4 Tail Installation	33
5 Propulsive Fuselage Concept Numerical Setup	37
5.1 Purpose of Simulations	37
5.2 Model & Meshing.	38
5.3 Sensitivity Study	42
5.4 Actuator Volume	46
5.5 Normalized Power Balance Terms	47
6 Performance of the Propulsive Fuselage Concept	49
6.1 Bare Fuselage Comparison	49
6.1.1 Boundary Layer Analysis.	50
6.1.2 Power Balance Analysis	50
6.2 Effect of Uninstalled Fan Operation.	52
6.2.1 Boundary Layer Analysis.	52
6.2.2 Power Balance Analysis	55

7	Conclusions & Recommendations	59
7.1	Conclusions.	59
7.2	Observations	60
7.3	Recommendations for Future Research	62
A	Uninstalled Fan Performance in a Constant Diameter Duct	65
A.1	Fan Behaviour	65
A.2	Flow Symmetry.	66
A.3	Velocity Triangles.	68
A.4	Discussion of Results.	69
B	Isolated Fan Test Rig Schematics	73
C	Enclosure Geometry	75
D	CFD Solver inputs	77
D.1	Default constants Spalart - Allmaras method	77
D.2	Default constants $k - \omega$ SST method	77
D.3	Default constants improved $k - \omega$ method	77
E	Normalization Verification	79
F	Numerical Flow Visualization	81
	Bibliography	83

List of Figures

1.1	Graphical representation of the Boeing BWB concept.	3
1.2	Graphical representation of the NASA D8 transport concept.	3
1.3	Graphical representation of Onera's NOVA concept.	3
1.4	Graphical representation of the Centerline concept.	3
1.5	Graphical representation of NASA's STARC-ABL concept.	3
2.1	Example of the propulsive fuselage concept.	7
2.2	Graphical representation of the boundary layer ingestion effect on the propulsive jet.	9
2.3	Indication of kinetic energy benefit with respect to thrust generation due to boundary layer ingestion.	10
2.4	Effect of an actuator disk on the boundary layer.	11
2.5	Control volume for power balance method as proposed by Drela.	12
2.6	Control volume for boundary layer ingestion with integrated wings.	12
2.7	Graphical representation of the power balance method.	14
3.1	The uninstalled fan test rig displayed in M-tunnel.	19
3.2	Schematic representation of the uninstalled fan test rig.	19
3.3	Improvement in maximum achievable flow coefficient per recommended case.	21
3.4	Station numbering in uninstalled test fan test rig.	21
3.5	Axial traversing system in uninstalled fan rig.	22
3.6	Azimuthal station numbering in uninstalled fan test rig.	22
4.1	Normalized fan characteristic map of the uninstalled fan.	26
4.2	Illustration of pitot probe angle versus incoming velocity angle.	26
4.3	Corrected fan characteristic map versus design fan characteristic map	26
4.4	Fan blade loading coefficient profiles at various flow coefficient settings.	27
4.5	Azimuthal variation in velocity at fan inlet (station 1).	28
4.6	Azimuthal variation in blade loading coefficient at fan exit (station 3).	28
4.7	Experimental installed setup	29
4.8	Experimental uninstalled setup.	29
4.9	Radial variation in inlet flow coefficient, installed versus uninstalled.	30
4.10	Radial variation in exit blade loading coefficient, installed versus uninstalled.	31
4.11	Radial variation in exit blade loading coefficient, installed versus uninstalled, corrected for stream tube height.	31
4.12	Radial variation of incoming incidence angle, installed versus uninstalled.	32
4.13	Schematic representation of tail position and measurement location in uninstalled fan rig.	33
4.14	Total pressure coefficient profile of tail wake versus normalized wake width. A comparison between wind tunnel and fan test rig data.	34
4.15	Azimuthal mass averaged blade loading ation, tail-on versus tail-off.	35
4.16	Azimuthal mass averaged downstream total pressure variation, tail-on versus tail-off.	35

4.17 Radial variation in exit blade loading efficient at $\theta = 0$, tail-on versus tail-off.	36
4.18 Radial variation in exit blade loading coefficient at $\theta = 90$, tail-on versus tail-off.	36
4.19 Radial variation of blade incidence angle, on versus tail-off.	36
4.20 Oil flow visualisation of tail wake effect on the fan's tip section.	36
5.1 Graphical representation of test setup used by B. Della Corte.	39
5.2 Dimensions numerical geometry input [mm].	39
5.3 Velocity distribution for a turbulent boundary layer.	40
5.4 Graphical representation of the mesh enclosure with a body of influence.	41
5.5 Graphical representation of the actuator volume.	46
5.6 Polynomial function overlap at $\phi = 0.5$	47
5.7 Polynomial function overlap at $\phi = 0.7$	47
5.8 Schematic representation of control volume used for the power balance analysis.	47
6.1 Axisymmetric body without shroud.	50
6.2 C_{P_t} boundary layer profiles of the fuselage.	51
6.3 $\frac{u}{V_\infty}$ boundary layer profiles of the bare fuselage.	51
6.4 Axial variation in C_{F_x} , bare fuselage.	51
6.5 Axial variation in $C_{\dot{E}}$ and $C_{\dot{e}}$, bare fuselage.	51
6.6 C_{P_t} boundary layer profiles at $\frac{x}{L_{fus}} = 0.91$, ered case.	53
6.7 C_{P_t} boundary layer profiles at $\frac{x}{L_{fus}} = 0.91$ including powered and bare fuselage data.	53
6.8 $\frac{u}{V_\infty}$ boundary layer profiles at $\frac{x}{L_{fus}} = 0.91$, ered case.	53
6.9 $\frac{u}{V_\infty}$ boundary layer profiles at $\frac{x}{L_{fus}} = 0.91$ including powered and bare fuselage data.	53
6.10 C_{P_t} boundary Layer Profiles at $\frac{x}{L_{fus}} = 0.97$	54
6.11 $\frac{u}{V_\infty}$ boundary Layer Profiles at $\frac{x}{L_{fus}} = 0.97$	54
6.12 Axial variation of axial momentum flux C_{F_x}	57
6.13 Axial variation of axial kinetic energy deposition rate $C_{\dot{E}_a}$	57
6.14 Axial variation of radial kinetic energy position rate $C_{\dot{E}_r}$	58
6.15 Axial variation of tangential kinetic energy deposition rate $C_{\dot{E}_t}$	58
6.16 Axial variation of pressure work $C_{\dot{E}_p}$	58
6.17 Axial variation of total mechanical power output, $C_{\dot{e}}$ and total kinetic energy deposition $C_{\dot{E}}$	58
6.18 Evaluation of composition of the total mechanical power output to the flow at $\frac{x}{L_{fus}} = 1.05$	58
A.1 Initial uninstalled fan test rig compressor map.	66
A.2 Normalized fan performance map of uninstalled fan test rig.	66
A.3 Normalized fan performance map CFX data	66
A.4 Illustration of downstream stall cell.	67
A.5 Variation of static wall pressure at station 1.	68
A.6 Variation of static wall pressure at station 3.	68
A.7 Fan map including unsteady regime.	69
A.8 Indication of flow reversal upstream of the fan.	70

A.9	Improvement in maximum achievable flow coefficient per recommendation.	72
C.1	Enclosure Inlet [mm].	75
C.2	Enclosure Side View [mm].	75
E.1	Difference due to normalization in C_{P_t} , bare fuselage.	79
E.2	Difference due to normalization in $C_{\dot{E}_p}$, bare fuselage.	79
E.3	Difference due to normalization in $C_{\dot{E}}$ and $C_{\dot{e}}$, bare fuselage.	79
E.4	Difference due to normalization in $C_{\dot{E}_a}$, bare fuselage.	79
E1	Contour plot of $\frac{u}{V_\infty}$ at $\phi = 0.5$	81
E2	Contour plot of C_{P_t} at $\phi = 0.5$	81

List of Tables

3.1	Main Output Parameters Experimental Campaign	22
3.2	Support Measurement Parameters Experimental Campaign	22
4.1	Difference in flow coefficient between CFD design and uninstalled fan test rig corrected fan map data.	27
4.2	Azimuthal variation in mass averaged blade loading between tail-on and tail-off case.	34
5.1	First cell layer height of the prism layers.	40
5.2	Results of the mesh convergence study.	41
5.3	Results for the mesh convergence study including a body of influence.	42
5.4	Results of the sensitivity analysis for turbulence model selection.	44
5.5	Results of sensitivity analysis for turbulence intensity setting.	45
5.6	Results of the sensitivity analysis for curvature correction and Sutherland's law.	45
5.7	Input coefficients for polynomial functions.	46
A.1	Difference in wall static pressure at various RPM settings.	67
A.2	Difference in inflow angle for $\phi = 0.4$	68
A.3	Difference in inflow angle for $\phi = 0.32$	69
A.4	Difference in inflow angle for $\phi = 0.28$	69

Nomenclature

Symbols

A	area
b	span
c	chord
d	diameter
D	drag
E	energy
\dot{E}	mechanical energy flow rate out of control volume
f	frequency
F	force
H	shape factor
k	kinetic turbulence energy
KE	kinetic energy
L	length
M	momentum
\dot{m}	mass flow
\hat{n}	unit normal vector, out of control volume
n	unit normal vector
p	pressure, polynomial input
P	power
PR	pressure ratio
r	radial position
R	radius
Re	Reynolds number
q_d	dynamic pressure
s	distance
S	surface, Sutherland's constant
t	time
T	thrust
T_∞	temperature in free stream
\bar{T}	averaged temperature
u, v, w	Cartesian component of $V - V_\infty$
U, V, W	Cartesian components of V
\bar{u}	mean velocity
u'	fluctuating motion
u^*	friction velocity
ν	eddy viscosity
V	fluid velocity vector, volume

\dot{W}_T	thrust power
W	weight
y^+	dimensionless height of boundary layer
Y_n	normalized radial position

Greek Symbols

β	blade incidence angle
δ	boundary layer thickness
δ_1	displacement thickness
δ_2	momentum thickness
Δ	quantity relative to free stream
ν	kinematic viscosity
τ	shear stress
ρ	density
μ	dynamic viscosity, molecular eddy viscosity
Π	blade loading
η	efficiency
η_p	propulsive efficiency
ϕ	flow coefficient
Φ	viscous dissipation rate, temperature ratio
$\dot{\epsilon}$	total mechanical power output
θ	azimuthal position
λ	wavelength
ω	specific dissipation rate

Coefficients

$C_{\dot{\epsilon}}$	total mechanical power outflow coefficient
$C_{\dot{E}}$	kinetic energy flux coefficient
c_f	friction coefficient
C_{Fx}	axial momentum flux coefficient
c_p	pressure coefficient
C_{p_t}	total pressure coefficient

Subscripts

∞	free stream
a	ambient, axial
i	inlet
j	jet
k	propulsor mechanical energy flow rate
p	pressure
r	radial
s	static
S	shaft
t	total, turbulent, tangential
u	trailing edge vortex potential
v	profile drag
V	volumetric
w	wake, wave
x	axial

Acronyms

BLI	Boundary Layer Ingestion
MTOW	Maximum Take Off Weight
KE	Kinetic Energy
LTT	Low Turbulence Tunnel
PIV	Particle Image Velocimetry
RANS	Reynolds Averaged Navier Stokes

Abstract

Aviation is an important connecting factor for humankind. Its presence has increased social and economic opportunities but also comes with its drawbacks. In light of the global climate crisis that humanity is facing, current trends in aviation are alarming, mainly because the number of flights worldwide is increasing rapidly. Since the aviation industry is a large producer of CO_2 , NO_x and noise, it contributes significantly to this climate crisis. The impact of aviation on the environment thus has to be reduced.

Because of the discussed crisis, research on sustainable aviation has received an impulse. One of the topics of interest in the search for sustainable aviation alternatives is boundary layer ingestion. Boundary layer ingestion proves to be a promising technology because it reduces the power requirement of the propulsor and, therefore, can reduce fuel consumption and the generation of emissions that pollute the air.

This research focuses explicitly on boundary layer ingestion in an aft fuselage installed propulsor. It aims to investigate the interaction between the fan and a propulsive fuselage concept. A combination of experimental and numerical work is used to achieve this. The experimental work focuses on the effect of fan installation in a propulsive fuselage concept. Parameters of interest are the flow coefficient, blade loading and incidence angle distribution. The numerical effort focuses on the effect of the fan on the propulsive fuselage concept. The boundary layer profile behaviour and the axial variation in power balance terms are utilised to investigate this.

In the experimental part of this thesis, an uninstalled fan test rig has been built to measure the uninstalled fan performance. This same fan has been used in previous experimental research on a propulsive fuselage concept [17]. The results show that the flow coefficient of the fan installed in the propulsive fuselage concept drops by 27.66% when compared with the uninstalled fan. The drop in flow coefficient causes the fan to shift to a less efficient point on the characteristic map. The mass averaged blade loading at $\phi = 0.5$ is reduced by 2.2%. Comparing installed and uninstalled fan data shows that the incoming boundary layer positively influences the fan's hub region. The increase in blade loading (4.8%) results from a rise in blade incidence angle due to the incoming boundary layer, which increases the lift of the inboard blade section.

In the numerical work, simulations are used to investigate the effect of the fan on the propulsive fuselage performance. The uninstalled fan data retrieved from the fan test rig has been utilised as an input for the actuator volume implemented in the CFD model. The results of the CFD model were compared with experimental data available from a previous related study, with a fan subjected to losses due to the incoming boundary layer [17]. Comparison of CFD and experimental data shows that the fan operation significantly impacts the inlet profile of the boundary layer entering the fan, increasing the total pressure by 11.7%. The fan operating under the influence of the incoming boundary layer deals with a 10.9% reduction in momentum addition to the flow. Power balance analysis has shown that the numerical increase in axial momentum flux is very high 332% because the experimental reference operates without momentum excess. Sequentially, other power balance deltas are high as well. The power balance analysis revealed that the increase in thrust (10.2%) comes with a disproportionate increase in axial kinetic energy deposition rate (16%). Because the numerical model does not include swirl and creates a momentum excess, the total me-

chanical power output in the flow was increased by 57% while reducing the kinetic energy deposition rate by 27%.

To summarise, this research has investigated the interaction between the fan and a propulsive fuselage concept. The effect of installation on the fan was small in terms of blade loading. In the hub region, a rise in blade loading has been identified. The numerical study on the effect of the fan on the propulsive fuselage performance has shown that the fan operation influences the boundary layer and propulsive jet. Upstream influences have to be taken into account while optimising the fan. Furthermore, the jet wake should be monitored closely to reduce kinetic energy deposition caused by the momentum excess.

1

Introduction

Aviation has been connecting humankind ever since the Wright flyer first took flight. Since commercial aviation was regulated in the Air Commerce Act of 1926, it has been a growing business that is not slowing down.

In its short existence, aviation has managed to contribute to roughly 2% of the total CO_2 production worldwide, with numbers still rising. During the 1980s oil crisis, the aviation industry has tried to reduce its dependency on fossil fuels because of the extremely high oil prices. These efforts, however, evaporated when the crisis was resolved and oil was back at its regular pricing.

In the last few decades, it has become apparent that a new crisis has impacted the aviation industry, the climate crisis. Because of the large amounts of fossil fuels humanity has been using, the air has become polluted, and, globally, the climate has begun to change. At the time of writing, Turkey and Greece are pestered with wildfires destroying ecosystems, massive heatwaves have struck Canada, and disastrous floods occurred in The Netherlands, Belgium, and Germany. Governments have tried to make agreements to stop global warming at 2 degrees Celsius, which is very ambitious.

In order to reduce the impact of aviation on this climate crisis, challenging goals have been set in the ACARE 2050 and Flightpath 2050 programmes [1, 16]. To achieve these goals CO_2 emissions need to be reduced by 75% in 2050, NO_x emissions need to be cut by 90% and noise by 65% with respect to the levels of typical new aircraft in the year 2000. Research is conducted on many methods to reduce or change aircraft fuel consumption, such as electric flight, next-generation aircraft configurations, and bio- or synthetic fuels. In this thesis, however, the focus will lie on implementing boundary layer ingestion in a propulsive fuselage concept configuration called CENTERLINE.

CENTERLINE is a turbo-electric distributed propulsion concept built upon a regular wing and tube aircraft structure. The design features two main turbofan engines mounted on the wings and a turbo-electric propulsor in the back of the aircraft. The CENTERLINE concept uses aft-fuselage integrated boundary layer ingestion propulsion, also known as the propulsive fuselage concept.

The use of boundary layer ingestion can positively affect the reduction of the fuel consumption of an aircraft. In essence, it reduces the power requirement of the aircraft, which in its turn reduces the amount of fuel needed and thus pollution created.

1.1. Previous Research on Boundary Layer Ingestion

The concept of boundary layer ingestion has been around for quite some time. It was A.M.O. Smith who in 1947 had the notion that the implementation of boundary layer ingestion or utilizing the boundary layer air can reduce fuel burn for aircraft [50]. These findings are derived from maritime technology where the wake of the hull is utilized to increase efficiency [51]. In the last decades, investigations have been ongoing in this field of research, but it is only in the past few years that

boundary layer ingestion is again seen as a reasonable and feasible solution for making flights more efficient.

In 2009, M. Drela introduced a new way of bookkeeping for boundary layer ingestion applications [38]. In the power balance method, the equations are energy-based instead of momentum-based. The latter means that the effect of the low momentum flow entering the propulsor can be considered. The power balance method is widely accepted in the field of boundary layer ingestion and has been cited in many works [11, 25, 27, 37, 43].

Another way of bookkeeping is called the exergy analysis method for boundary layer ingestion and was first introduced by Arntz et al. [9]. The big difference between the power balance method and the exergy analysis method is that the exergy analysis method takes into account the thermal management of the aircraft [9].

Boundary layer ingestion has been a topic of many research projects in the past couple of years. A wide variety of novel aircraft concepts have been investigated, combining various methods of boundary layer ingestion. The two main categories are partial and fully engulfed boundary layer ingestion.

The blended wing body concepts mostly use partial boundary layer ingestion, where the propulsor is sunken into the airframe, as shown in figure 1.1. Examples of blended wing body concepts with boundary layer ingestion are the Boeing BWB-450, Boeing N2A-ext, and the N3-X [20, 26, 35]. The expected fuel burn reduction for these concepts ranges from 3-8 %.

Another aircraft concept that uses partial boundary layer ingestion is the NASA D-8. This aircraft has aft-mounted propulsors, as shown in figure 1.2. The flight mission of this concept is the same as that of an A320 [57]. The NOVA concept is an unconventional concept introduced by Onera [32]. Here, the partial boundary layer ingesting propulsors are mounted on the side of the fuselage, as depicted in figure 1.3.

Two projects in the axisymmetric fuselage category are CENTERLINE and STARC-ABL. In the CENTERLINE project, depicted in figure 1.4, a proof of concept is provided for the axisymmetric fuselage with boundary layer ingestion concept [48]. The goal of the CENTERLINE project was to maximize the benefit of the aft fuselage wake filling. The latter has been achieved by installing two wing-mounted geared turbofan engines, which provide the residual thrust needed in the mission. The aft turbo-electric fan will provide the wake filling power. According to Seitz et al. [49] this concept can potentially reach a fuel burn reduction of 3.2-4.7%.

A similar project researching the propulsive fuselage concept is the STARC-ABL, shown in figure 1.5. The main goal of this concept was to investigate if turbo-electric propulsion, such as shown in next-gen aircraft designs, can also be used on conventional single-aisle aircraft and whether benefit could be drawn from such a configuration in terms of fuel burn reduction [60]. According to Welstead et al., this concept can achieve a fuel burn reduction of 9% when in an economic mission and 15.2% when flying the design mission in combination with a 3.8% reduction in MTOW, which can lead to structural benefits [61]. In the investigation of Yildirim et al. on the optimisation of the STARC-ABL design, it is stated that these numbers are only feasible for cruise flight [64].

Aside from the system based research introduced above, work is available on many detailed aspects of boundary layer ingestion. For example, the investigation of Lv uses the power balance method of Drela to investigate the power conversion of boundary layer ingestion concepts, both numerically and experimentally [36]. A second example is the work of Della Corte et al. that has contributed to the knowledge of boundary layer ingestion testing in a fully integrated model [15, 17].

More research on the detailed analysis of boundary layer ingestion is included in the research motivation in the next section. In section 1.2, the specific contributions to numerical and experimental

research are presented, along with the grey areas in boundary layer ingestion research.



Figure 1.1: Graphical representation of the Boeing BWB concept [20].

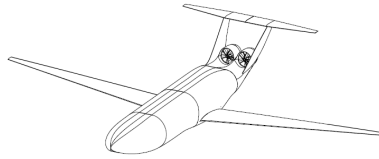


Figure 1.2: Graphical representation of the NASA D8 transport concept [57].



Figure 1.3: Graphical representation of Onera's NOVA concept [32].



Figure 1.4: Graphical representation of the Centerline concept [19].



Figure 1.5: Graphical representation of NASA's STARC-ABL concept [61].

1.2. Research Motivation & Objective

State-of-the-art research on the topic of boundary layer ingestion has shown that this concept has the potential to reduce the fuel burn of aircraft by 3.2% to 4.7% in an axisymmetric configuration [49].

As shown in the previous section, much research has focused on the system-level implementation of boundary layer ingestion and its benefits [48, 60, 61]. The system-level research has created an understanding of the potential gains that boundary layer ingestion can produce. Since the depicted gains are considerable, boundary layer ingestion has to be studied in greater detail to quantify profits and understand which mechanisms play a role in achieving said benefit.

Many works have focused on the numerical study of boundary layer ingestion concepts. For example, the works of Baskaran and Chaves have studied the application of the power balance method of Drela and exergy analysis by Arntz et al. [8] on propulsive fuselage concepts numerically [11, 14].

Other numerical work focused on the improvement of the propulsive efficiency and the optimisation of fuselage shape while dealing with a constant pressure jump [13].

Numerical studies focusing on the aerodynamic flow field have been limited mainly to the non-axisymmetric cases, as shown in the works of Geiselhart et al. and Giuliani & Chen [20, 21].

Numerical work completed on a propulsive fuselage concept flow field mainly focuses on the minimisation of inlet distortion, as shown in Kenway [30]. Specific research on the fan tip leakage in boundary layer ingestion applications is performed by Yang et al. [63].

The knowledge gained from the numerical works presented is of great value; however, it has rarely been validated with experimental work. Moreover, most of the works presented assume a perfect axisymmetric inflow or strive to reduce inflow distortion. It is thus vital to understand if the assumption of axisymmetry holds for aft propulsive boundary layer ingestion research and what the effect of non-uniform inflow is on the fan performance.

In the field of experimental research on boundary layer ingestion, limited exploration has been carried out. Large demonstrators like the D8 double bubble or BWB-450 have been tested to proof the overall feasibility of boundary layer ingestion [34, 57]. Others, like Atinault et al., focused on the

effect of wake ingestion in both experimental and numerical setups [10]. Wake ingestion is a simplified form of boundary layer ingestion where no potential flow interaction occurs.

These examples, however, do not dig into the understanding of the aerodynamic flow field. The work of Gunn and Hall does map the aerodynamic flow field of a boundary layer ingesting fan. The incoming disturbance is, nevertheless, non-axisymmetrical [24]. A study performed by Pardo has shown the building of a fan test rig to perform blade optimisation on a boundary layer ingestion fan [41]. This work, however, does not give any in-depth information on the interaction between the boundary layer and the fan. The previous is the case because the boundary layer is imposed on the fan by an upstream mesh instead of a curved body like a fuselage.

The most recent addition to the experimental work on axisymmetric boundary layer ingestion is that of Della Corte et al. [17]. This work focuses on the interaction between the fuselage boundary layer and the boundary layer ingesting fan by the use of an experimental demonstrator.

To summarise, little research has been conducted on the axisymmetric fuselage configuration with boundary layer ingestion in the experimental field. At the moment of writing, no work has been published comparing the fan performance of an uninstalled fan with one installed in a boundary layer ingestion configuration. To better understand the aerodynamic behaviour of the boundary layer and the fan, it is essential to investigate the case mentioned above.

As shown in the previous overview, much effort has been put into analysing boundary layer ingestion from a system-based approach. The overview of knowledge gained in previous research shows a gap in the understanding as to how the boundary layer ingestion fan performs in a fully integrated boundary layer ingestion setup with respect to its uninstalled performance.

This work aims to bring more clarity to the grey areas discussed. In this research, isolated fan performance data will be mapped with the help of an uninstalled fan test rig. The uninstalled data will be compared with the available performance data of the fan in an installed configuration. This comparison demonstrates the aerodynamic effect of installation in a propulsive fuselage concept on the fan.

Moreover, this work proposes a method to combine experimental and numerical data for building a CFD model of a propulsive fuselage concept body. The numerical work is compared with available experimental data to show how the fan operation affects the flow surrounding the propulsive fuselage. To the author's knowledge, this combination of experimental and numerical inputs has not been attempted before in a boundary layer ingestion setting.

The available experimental data is collected from low-speed wind tunnel testing. The data from the fan test rig is also obtained at a lab scale. Consequently, the Reynolds and Mach numbers do not match the full-flight conditions. Therefore, this research has focused on the qualitative results that explain the physical mechanisms involved in fan and fuselage flow interactions for a propulsive fuselage concept.

Concluding, there is little knowledge available on the effect of boundary layer ingestion on an aft installed propulsive fuselage concept propulsor. This research aims to expand on the knowledge available in the field of propulsive fuselage concepts by using both experimental and numerical methods. The experimental work will consist of an uninstalled fan test rig, and the numerical work will cover the development of a method to study the effect of the propulsor on the propulsive fuselage performance. The research question of this thesis has thus been formulated as follows:

What effect does the flow interaction between a fan and a propulsive fuselage concept have on their respective aerodynamic performance?

The research objective is divided into sub-questions which are investigated throughout this study:

- How does the incoming boundary layer influence the fan's inflow conditions and its addition of work to the flow?
- How does the fan operation influence both the boundary layer and propulsive jet of the propulsive fuselage concept?

1.3. Thesis Outline

This thesis is divided into seven main chapters, including this introduction.

Chapter 2 will introduce the reader to relevant knowledge concerning boundary layer and boundary layer ingestion theory and introduces the power balance method.

The experimental part of this thesis will be discussed in chapters 3 and 4. In chapter 3, the fan test rig will be introduced along with the measuring methodology. Chapter 4 will continue by presenting the results of the experimental campaign completed with the fan test rig. Results include an analysis of the aerodynamic fan behaviour, the azimuthal performance variation, effects of installation, and a section dedicated to the effect of tail wake on the fan. The numerical part of this thesis is presented in chapters 5 and 6. Chapter 5 introduces the numerical setup, its verification and validation processes, and the experimental data in the numerical setup. The introduction of the numerical setup is followed by chapter 6, where the results of the numerical simulations are presented. These results are divided into the bare fuselage analysis and the propulsive fuselage analysis. This thesis is concluded by chapter 7. This last chapter will summarise the main observations from this thesis, draw the main conclusions, and offers recommendations for future work.

2

Theoretical Background

This chapter presents a summary of the theoretical background deemed necessary for boundary layer ingestion research. The chapter will give a general introduction on how boundary layer ingestion works, its benefits and drawbacks. This chapter also provides an overview of the power balance method, the preferred method for analysing the performance of boundary layer ingestion concepts. The case-specific theory will be presented in its corresponding chapters when needed.

2.1. Boundary Layer Ingestion Theory

A boundary layer is present around every object placed in a free stream, which ultimately results in the body experiencing drag. Boundary layer ingestion is a technique where the inlet of the propulsor or the propulsor itself is placed in the boundary layer of the body [27]. This work uses an axisymmetric inflow case where the entire boundary layer of the body is fed to the propulsor as is demonstrated in figure 2.1.

It is important to note that a differentiation is made between boundary layer and wake ingestion. The term boundary layer ingestion describes the ingestion of the actual boundary layer attached to the body of interest. Whereas wake ingestion investigates the ingestion of the wake behind the body by the propulsor, here, the distance between the propulsor and the body is large enough to avoid any potential flow interaction. The differentiation between the two is essential since evaluating the pressure deficiencies for the two cases differs. However, in literature, it is common to classify wake ingestion as a simplified form of boundary layer ingestion.

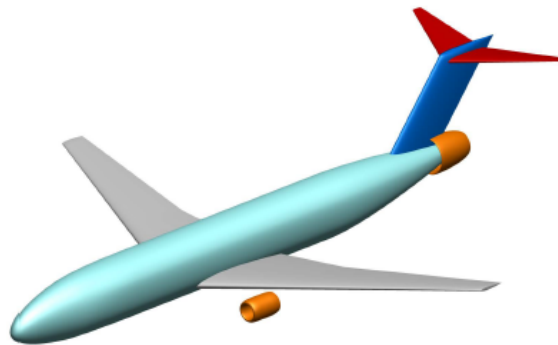


Figure 2.1: Example of the propulsive fuselage concept [60]. Concept illustrated with conventional under the wing propulsors and an aft boundary layer ingestion propulsor.

As stated above, when implementing boundary layer ingestion, the boundary layer present around a body is fed to the inlet of the propulsor. The boundary layer fluid has a lower momentum than the free stream. Therefore, fluid ingested by the propulsor will have a lower total pressure than the free stream, which can potentially reduce the fuel consumption of an aircraft.

One of the reasons why boundary layer ingestion has the potential to make aviation more fuel-efficient is that the ingestion of the low momentum fluid leads to a reduction of the power requirement of the aircraft [25]. If, for example, the presence of the lower momentum fluid leads to a lower velocity in the propulsive stream tube, less power is required to impart a given momentum [57]. Betz uses equation 2.1 [12] for this situation to show that with a reduction in inlet velocity and a lower power input, the same thrust can be delivered. Theoretically, less shaft power is thus required to produce the same thrust when implementing boundary layer ingestion.

$$P = \frac{TV_\infty}{\eta_p} \quad (2.1)$$

Another way to explain the benefit of boundary layer ingestion is given in the work of Plas [42]. Usually, the wake drag generated by the body of the aircraft creates a momentum deficit, as is shown in figure 2.2 [42]. The conventional propulsor will need to create a momentum excess to balance this deficit, whereas the boundary layer ingestion case does not.

In equation 2.2 [42] the power required for a propulsor without boundary layer ingestion is shown. One can see that this relation is a function of the difference in kinetic energy between the exit of the propulsor and the free stream. The actual power required from the engine in cruise, however, is the power to counteract the total drag, as is shown in equation 2.3. When the ideal case for 100% boundary layer ingestion is considered, the jet stream momentum can exceed the free stream momentum when operating in cruise, as is shown in equation 2.4. Implementing this change into equation 2.2 gives equation 2.5, the power requirement for an engine with boundary layer ingestion. Here one can see that since $u_j > u_w$, $P_{no-BLI} > P_{BLI}$ and thus, the power requirement has been lowered [42].

$$P_{no-BLI} = \frac{\dot{m}}{2}(u_j^2 - u_\infty^2) \quad (2.2)$$

$$P_{useful} = \dot{m}(u_j - u_\infty)u_\infty \quad (2.3)$$

$$\dot{m}(u_j - u_w) = \dot{m}(u_\infty - u_w) \quad (2.4)$$

$$P_{BLI} = \frac{\dot{m}}{2}(u_\infty^2 - u_w^2) \quad (2.5)$$

The explanation about the origin of the reduction in power requirement for boundary layer ingestion mainly focused on reducing the momentum deficit. Another way of looking at boundary layer ingestion can be derived from the fact that the power supplied by the engine is a function of the kinetic energy difference in the flow.

Due to the lower inlet momentum imposed on the face of the propulsor, the kinetic energy difference required to generate a similar amount of thrust is lower, as is shown in figure 2.3. This figure was constructed using data from the research of Lv et al. [37]. The figure shows the difference in the

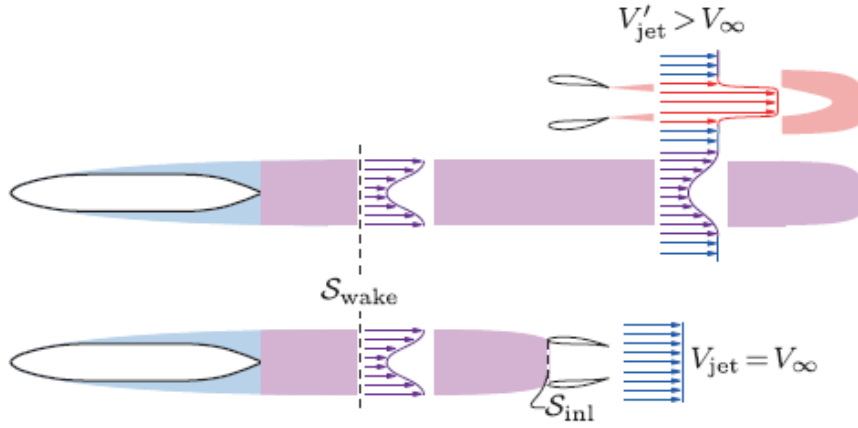


Figure 2.2: Graphical representation of the boundary layer ingestion effect on the propulsive jet [25].

power requirement as dictated in equation 2.6. Here, one can see that lowering the inlet velocity has a quadratic effect on the kinetic energy and thus the power requirement.

In equation 2.7 the required thrust power is shown, which scales as a linear product with V_{in} , this makes the boundary layer velocity the dominant term. Thus, when using a lower inlet momentum, less kinetic energy is needed from the propulsor with respect to a conventional engine configuration because of the reduction of the moment deficit.

The lowering of the inlet velocity of the engine and the outlet or jet velocity ultimately increases the propulsive efficiency of the engine when assessing the 'Froude Efficiency' or propulsive efficiency, shown in equation 2.8. When examining equation 2.8, one can see that the propulsive efficiency is displaying normal behaviour when the velocity in the free stream is higher than that in the boundary layer flow at the inlet. However, in an ideal case where perfect wake filling would take place and the outlet jet flow is equal to the free stream, the efficiency can become unity or even higher than unity, which is called the 'efficiency paradox'[36]. To be able to assess the performance of boundary layer ingestion configurations, the power balance method has been developed. A detailed discussion on this method is present in section 2.2.

$$KE = \dot{m}(v_j^2 - v_{in}^2) \quad (2.6)$$

$$\dot{W}_T = \dot{m}(v_j - v_{in})v_{in} \quad (2.7)$$

$$\eta_{propulsive} = \frac{V_{\infty} T}{P} \quad (2.8)$$

Aside from the fact that boundary layer ingestion can lower the power requirement of the aircraft, some other beneficial effects should be considered, as is shown in the works of Hall et al., Lv and Plas [[25], [36], [43]].

The first benefit is that the decreased wake energy losses cause the propulsive efficiency, $\eta_{propulsive}$, to increase [25]. This wake which is created by the airframe is accounted for in the profile drag.

Since the wake-energy flow rate is reduced [36] due to the re-energising of the wake, the wake mixing losses are lowered because less kinetic energy is wasted [43]. As shown in equation 2.6 a decreased jet velocity, due to reduced mixing losses, decreases the kinetic energy and increases the propulsive efficiency of equation 2.8. Note that this is most beneficial when ideal wake or boundary layer filling is used [36].

On top of the decrease in wake losses, the jet mixing losses created by the velocity deficiency between the outlet jet and the free stream are reduced as well [25]. As was shown in figure 2.2 the

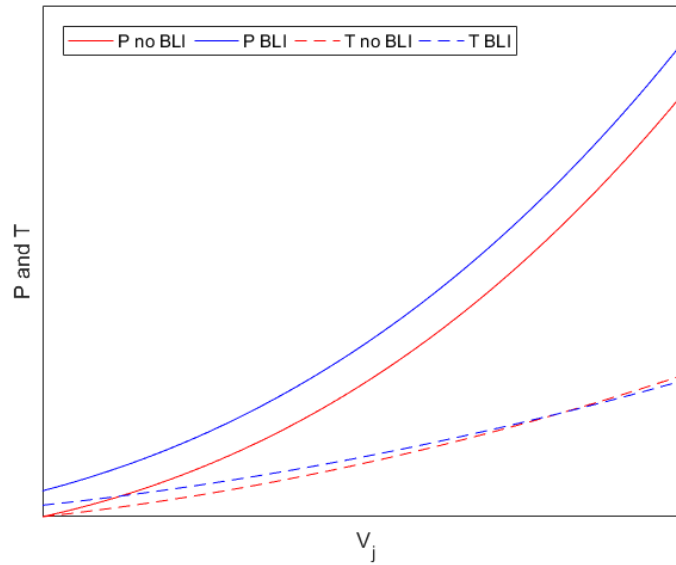


Figure 2.3: Indication of kinetic energy benefit with respect to thrust generation due to boundary layer ingestion.

momentum deficiency and thus the velocity difference at the outlet is reduced, which leads to fewer stresses between the free stream and the jet. The latter reduces dissipation losses and thus improves efficiency.

When considering the thrust and drag bookkeeping of the aircraft, propulsors utilising boundary layer ingestion can have some secondary benefits with respect to conventional aircraft. For example, the installation penalty of the engine can be reduced because no pylons have to be present, which reduces the wetted surface area needed to fit an engine. The propulsion integration can also help in smoothing the area distribution and thus reduces both clean and interference drag of the engine installation [25, 36].

Boundary layer ingestion can, despite its propulsive benefits, cause detrimental interaction effects. One negative effect on the engine and aircraft performance is the distortion of the incoming flow over the fan face.

In a boundary layer ingestion configuration, there is a risk of developing a stall cell, as stated in the work of Giuliani and Chen [21]. In order to prevent stalling of the fan blades, measures such as an adequate blade design or passive and active flow control can be taken into account to avoid the development of such a cell. When considering an axisymmetric boundary layer design as shown in figure 2.1 little distortion is seen by the fan because, as stated in Kenway and Kiris, 'the propulsor sees essentially radially symmetric inflow conditions' [30]. Nonetheless, downwash from the wings and the presence of the vertical tail should not be forgotten as sources of possible distortion when evaluating this design [30].

Keeping track of and reducing the latter distortions for designs incorporating boundary layer ingestion is of great importance because the induced vibrations and reduced stall margin can lead the engine into surge and ultimately flame out and power loss [27].

Another adverse effect of the implementation of boundary layer ingestion can be attributed to the change in aircraft performance because the propulsor and airframe may interact, resulting in boundary layer dissipation before the propulsor or even separation [25]. The effects of this can either be positive or negative, as shown in the work of L.H. Smith [51]. The previous is the case be-

cause the power saving is dependent on the disk loading, the shape factor and the wake recovery. When the shape factor is high, the power saving is high as well; however, the flow, in this case, is near separation. The shape factor H is the ratio of displacement thickness and momentum thickness, as shown in equation 2.9 [59]. Here equation 2.10 denotes the displacement thickness describing the loss of mass flow due to the presence of the boundary layer. Equation 2.11 shows the momentum thickness, which describes the corresponding loss of momentum [44, 59]. In the equations above, u is the velocity component within the boundary layer and u_∞ is the velocity component of the free stream.

In terms of the boundary layer itself, there are also changes when utilising boundary layer ingestion. The viscous drag of the body or fuselage is increased slightly because the flow is accelerated towards the actuator. The latter increases the velocity gradient of the flow and thus increases stresses [36]. In addition to this, the fan has an upstream influence on the boundary layer. The upstream influence causes a variation in the total pressure distribution and thus changes the profile of the boundary layer [23]. The latter causes an increase in the pressure drag of the body. Figure 2.4 gives a visual representation of the change in the velocity gradient of the boundary layer.

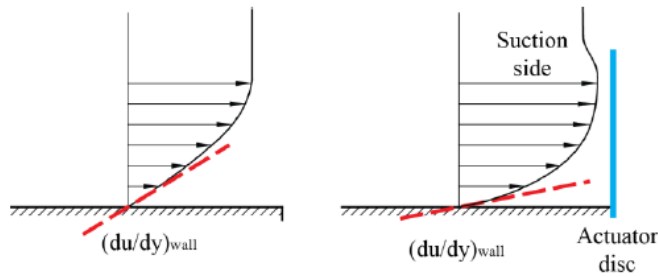


Figure 2.4: Effect of an actuator disk on the boundary layer. Normal boundary layer on a flat plate (left), boundary layer with actuator disc on a flat plate (right) [36].

$$H = \frac{\delta_1}{\delta_2} \quad (2.9)$$

$$\delta_1 = \int_0^\infty \left(1 - \frac{u}{u_\infty}\right) dz \quad (2.10)$$

$$\delta_2 = \int_0^\infty \frac{u}{u_\infty} \left(1 - \frac{u}{u_\infty}\right) dz \quad (2.11)$$

2.2. Power Balance Method

The merits of comparison discussed in the previous section can give ambiguous results for an integrated propulsor aircraft configuration because of their inability to distinguish between thrust and drag parameters properly. The Power Balance Method proposed by Drela [38] however, offers an outcome because it is based on mechanical power analysis.

The Power Balance Method describes all elements of power which play a role in propulsion and is, therefore, an adequate analysis tool for the performance of boundary layer ingestion. What distinguishes the power balance method from other methods is that it focuses on energy conservation instead of momentum conservation. The latter reduces the amount of information needed, which simplifies calculations [46].

The power balance method starts with selecting a proper control volume for analysis, which takes into account body, propulsor and free stream, as shown in figure 2.5. Note that for the control volume, two boundaries are shown, namely the inner boundary, S_B , positioned at the body [38] that

The elements on the right-hand side of the equation denote the power consumed, as mentioned above. As shown in equation 2.16 the 'Mechanical energy flow rate out of the control volume' or \dot{E} can be split into multiple elements [38]. The first term $W\dot{h}$ or $-F_x V_\infty$ is reversible and shows the power consumed to gain potential energy, or in other words, to gain altitude [11]. The first irreversible term, \dot{E}_a shown in equation 2.17, is given to be the 'Wake streamwise kinetic energy deposition rate' or, in other words, the axial kinetic energy which is discharged through the Trefftz plane [11, 38]. The next irreversible term is \dot{E}_v shown in equation 2.18. This term describes the 'Wake transverse kinetic energy deposition rate', which is similar to \dot{E}_a but now the kinetic energy flow through the Trefftz plane due to the normal velocity is considered [11, 38]. \dot{E}_p denotes the 'Wake pressure-defect work rate', thus the power leaving the control volume through the Trefftz plane as a result of the pressure defect in the fluid, as is shown in equation 2.19 [11, 38]. The last irreversible term of \dot{E} is, \dot{E}_w which can be described as the 'Wave pressure-work and kinetic energy outflow rate', which shows the energy resulting from pressure deficiencies and kinetic energy flows leaving through the side cylinder plane [38].

With the three equations mentioned, the irreversible power consumption of the aircraft can be captured; note that all elements should be present in order to gain an understanding of how the system works [11]. The sum of the three irreversible terms is equal to the product of the inverse drag and the free stream velocity [38].

$$\dot{E} = W\dot{h} + \dot{E}_a + \dot{E}_v + \dot{E}_p + \dot{E}_w \quad (2.16)$$

$$= -F_x V_\infty + \dot{E}_a + \dot{E}_v + \dot{E}_p + \dot{E}_w$$

$$\dot{E}_a = \iint_{TP} \frac{1}{2} \rho u^2 (V_\infty + u) dS \quad (2.17)$$

$$\dot{E}_v = \iint_{TP} \frac{1}{2} \rho (v^2 + w^2) (V_\infty + u) dS \quad (2.18)$$

$$\dot{E}_p = \iint_{TP} (p - p_\infty) u dS \quad (2.19)$$

In equation 2.16 the term for potential energy was mentioned. It is composed of the product of the net axial force and the free stream velocity. In equation 2.20 the expression for this axial force is shown. This expression can also be split up into different elements, as shown in 2.21 [38]. Here, F_v denotes the contribution of profile drag, as is shown in equation 2.22. F_u covers part of the induced drag, as shown in equation 2.23. F_w , equation 2.24, is the contribution of the wave drag in supersonic flow [38].

$$F_x = \iint_{TP} -[(p - p_\infty) + \rho(u - V_\infty)u] dS + \iint_{SC} -\rho(u - V_\infty)v dS \quad (2.20)$$

$$F_x = F_v + F_u + F_w \quad (2.21)$$

$$F_v = \iint_{TP} -[(p - p_\infty) + \frac{1}{2} \rho (V_\infty^2 - V^2) - \frac{1}{2} \rho u^2] dS \quad (2.22)$$

$$F_u = \iint_{TP} \frac{1}{2} \rho (v^2 + w^2) dS \quad (2.23)$$

$$F_w = \iint_{SC} -\rho(u - V_\infty)v dS \quad (2.24)$$

The last term in equation 2.12 which has to be discussed is the 'viscous dissipation rate', Φ , shown in equation 2.25. This term describes the amount of kinetic energy converted to heat due to friction with the body in the laminar or viscous sublayer. As shown in figure 2.7 there are various forms of dissipation to consider. In cruise flight, the airframe dissipation consists of three terms as shown in equation 2.26 [46], since wave dissipation will not be taken into account for this study. The losses from the propulsor should also be taken into account; these losses usually arise from mixing, tip and other mechanical and turbomachinery losses.

$$\Phi = \iiint_{CV} (\vec{\tau} \cdot \nabla) \vec{V} dV \quad (2.25)$$

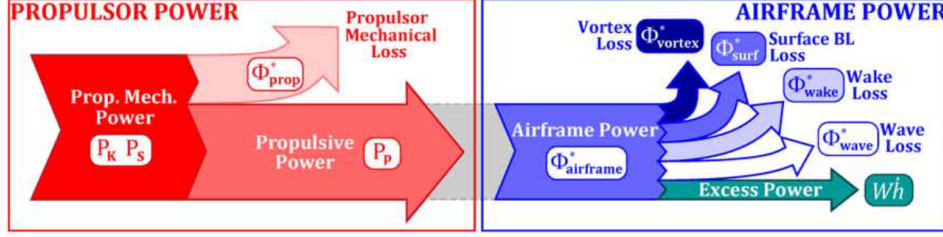


Figure 2.7: Graphical representation of the power balance method [46].

$$\Phi_{airframe} = \Phi_{vortex} + \Phi_{surface} + \Phi_{wake} \quad (2.26)$$

Having sorted out the framework of the power balance method, it is important to find out how it can function as a metric of comparison, but most importantly how it can be used to understand the efficiency paradox. The latter is done by evaluating the total change in power which the implementation of boundary layer ingestion has caused, as is shown in equation 2.27 [38]. The change in power is determined by the sum of change in irreversible consumption and all factors of dissipation. The potential energy will not make a difference here because aircraft with the same mission profile will often be compared, so the altitude and cruise speed will not change.

$$\Delta P = \sum \Delta \dot{E} + \sum \Delta \Phi \quad (2.27)$$

In section 2.1 it was already established that the propulsive efficiency is given by equation 2.8, which can also be written in the form of equation 2.28. In the work of Baskaran, the propulsive efficiency of a normal propulsor and boundary layer ingestion propulsor are compared by filling in the corresponding power balance method terms in equation 2.28. After some manipulation, the propulsive efficiency for a free stream propulsor is as given in equation 2.29, where the efficiency will always remain lower or be equal to unity. The result for an ideal wake filling, boundary layer ingestion propulsor is found in equation 2.30, which will always be equal or above unity. The previous is because extra power 'added' to the equation does not come from the propulsor itself.

In addition to this, an improved efficiency definition has been proposed in the work of Hall et al. [25] as is shown in equation 2.31. This definition eliminates both the nuisance of defining the net-thrust and the efficiency paradox since the jet dissipation will be higher or equal to zero.

$$\eta_{propulsive} = \frac{TV_{\infty}}{P_{propulsor}} \quad (2.28)$$

$$\eta_{propulsive} = \frac{TV_{\infty}}{TV_{\infty} + \dot{E}_a} \quad (2.29)$$

$$\eta_{propulsive} = \frac{P_{propulsor} + \dot{E}_a}{P_{propulsor}} \quad (2.30)$$

$$\eta_{propulsive} = \frac{P_K - \Phi_{jet}}{P_K} \quad (2.31)$$

3

Uninstalled Fan Test Rig

Studying the fan performance of a boundary layer ingesting fan requires mapping of the isolated fan performance. To this end, an uninstalled fan test rig has been designed, produced, and validated to determine the actual aerodynamic performance of the fan used in the installed propulsive fuselage experiments.

This chapter will introduce the purpose of the fan test rig in section 3.1. The design of the setup will be discussed in section 3.2, followed by the measurement techniques used in section 3.3.

3.1. Purpose

An experimental campaign has been conducted to obtain information about installation effects imposed on the fan in a propulsive fuselage concept configuration. In order to do so, an isolated fan test rig, designed for this thesis, is used in combination with installed data retrieved from B. Della Corte [17]. This section will serve as an introduction to justify the experimental campaign.

As stated in chapter 1, the research question will be answered through the means of numerical simulations in combination with experimental data. The experimental data is retrieved with the use of an uninstalled fan test rig, and will serve multiple purposes, as listed below:

- Measure the fan characteristic map to determine the operating range of the fan in uninstalled conditions.
- Assess the effect of installation in a propulsive fuselage concept on the fan blade loading.
- Assess the effect of an incoming tail wake on the fan blade loading.
- Create an actuator volume input for the numerical model to investigate installation effects further, based on the uninstalled fan data.

The first point of interest was to create a fan characteristic map of the fan experimentally since only CFD data of the design was available. In the campaign of B. Della Corte, a scaled model of the CENTERLINE fan with a diameter of 76.15 mm was used to 'drive' the propulsive fuselage model. The uninstalled fan test rig discussed in this thesis uses the same fan. The experimental campaign with the uninstalled fan test rig will be relevant to measure the design performance against the actual performance of the fan. The retrieved data will be used to determine the actual operating range of the fan and its performance in terms of blade loading.

Since the research goal is to assess the effect of installation on the aerodynamic fan performance in a propulsive fuselage concept, point two focuses on answering the research question through a comparison of experimental data.

In- and outflow data obtained in the installed and uninstalled test cases will be compared to learn how the blade loading and flow coefficient profiles differ. Comparing the radial distributions of these variables can give an insight into how the installation affects the fan.

As shown in figure 2.1, installation in a propulsive fuselage configuration causes the fan to be impacted by the presence of upstream aerodynamic lifting surfaces such as the vertical tail. The tail wake induces a non-axisymmetric distortion onto the fan, which could alter its behaviour.

In this campaign, the upstream wake will be handled separately from the distortions introduced by the fuselage or shroud. A tailpiece will be placed in the uninstalled fan test rig to map the effect of an incoming tail wake on the fan performance. Comparison of the tail-on and tail-off cases can give an insight into how the fan is affected by the installation of upstream elements.

The last point is to create an actuator volume input, based on the uninstalled fan data, for the numerical model to investigate installation effects further. In the numerical simulations, an actuator volume model is used to gain insight into the performance of the propulsive fuselage concept. Since a reasonable estimation of the pressure profile of the fan is needed, the experimental campaign will be used to retrieve the necessary data. This data will be presented in the form of the isolated pressure profile downstream of the fan.

Without data on the fan's behaviour and performance in isolated conditions, it is hard to single out behaviour caused purely by boundary layer ingestion or other elements of the installation. The lack of information would make it hard to implement an accurate actuator volume model in the numerical simulations since the pressure ratio would have to be predicted from the required thrust.

With the knowledge obtained from the experimental campaign, it is easier to differentiate which effects result from installed elements such as the shroud or other obstacles and which are a result of boundary layer ingestion.

3.2. Experimental Setup

In this section, the design of the uninstalled fan test rig discussed in section 3.1 will be introduced, along with details on design choices and the validation of the setup.

The uninstalled fan test rig shown in figure 3.1 is a static configuration, meaning that the turning of the fan induces all mass flow. The fan is placed in a Plexiglass tube to exclude any effects caused by the design of a shroud. The tip clearance amounts to 1.4% of the fan diameter.

The Plexiglass tube is fitted with a bell mouth inlet to ensure a uniform flow inside the tube and avoid any adverse pressure gradients at the edges of the tube inlet. The bell mouth inlet is a non-optimised design and merely creates a lip for the flow to follow rather than stalling at a corner. The inlet only converges up to the point where it matches the inner diameter of the tube. Checks have been performed with tufts to ensure the functionality of the inlet.

The fan is placed two fan diameters away from the inlet to ensure an undisturbed flow at the fan inlet. Six symmetrical struts are placed upstream of the fan to support the internal structure; they are assumed not to have a considerable effect on the flow field because of their thickness (1 mm).

The tube is made out of Plexiglass to allow the setup to be used for various flow visualisation techniques such as oil flow visualisation and PIV. The visibility of the experimental setup gives the re-

searcher a safer work environment and a better basis for calibrations, which are carried out with the use of lasers.

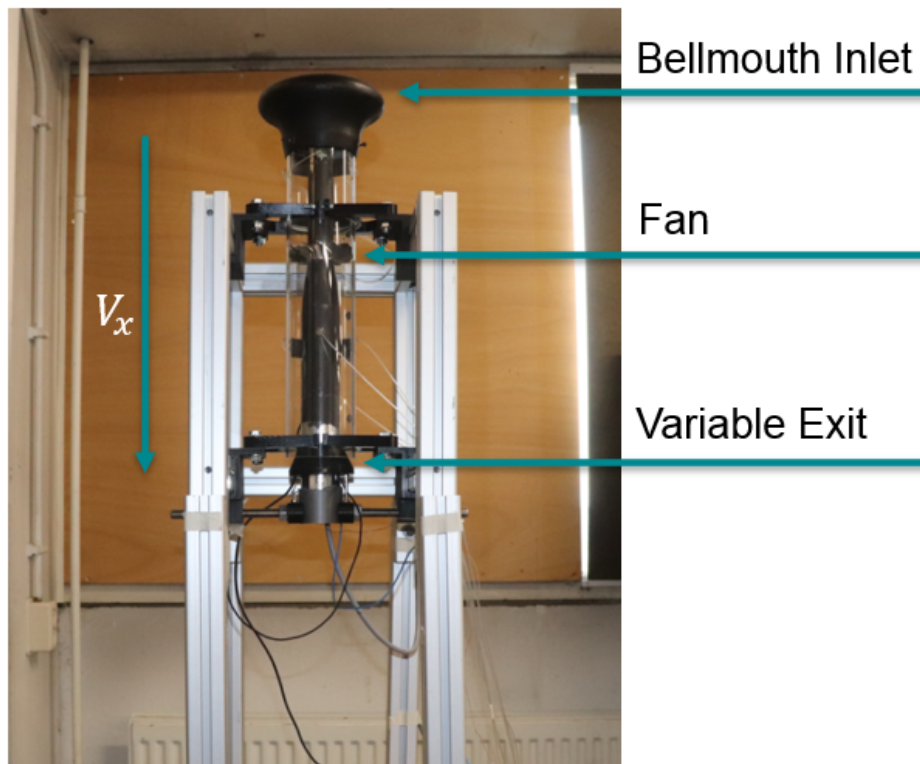


Figure 3.1: The uninstalled fan test rig displayed in M-tunnel.

In the baseline or 'clean' case, use will be made of a stationary 'nose' upstream of the fan to guide the flow into the fan without inducing swirl. Note that this nose is replacing the conventional spinner cone and will not be turning. In the tail-on case, the stationary 'nose' will be fitted with a disturbance in the form of a NACA0012 airfoil. The airfoil is included to examine the effect of an upstream disturbance on the fan performance. Figure 3.2 shows a schematic representation of the clean inlet.

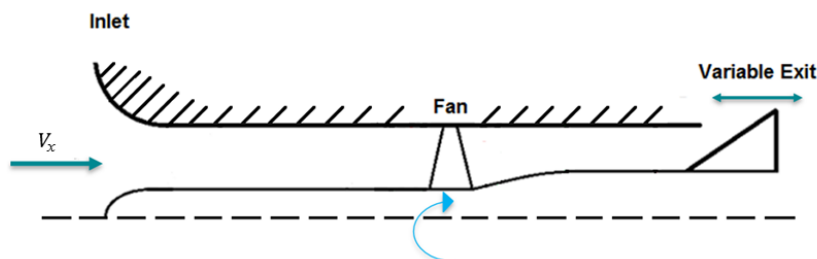


Figure 3.2: Schematic representation of the uninstalled fan test rig. View is turned 90 degrees concerning the actual orientation.

As mentioned in the previous paragraph, struts support the nose piece. The inclusion of the struts has two purposes: (i) the nose needs some structural attachment to the tube to stay in position, (ii) it can damp out vibration-induced motion of the nose and thus decrease noise in the readings of the equipped sensors. Although not optimal from an aerodynamic point of view, the struts serve a

structural purpose.

The struts used for the setup are NACA0012 airfoils with a thickness of 1 mm. The latter design choice ensures a uniform flow with minimal wake formation caused by the support structure. Various symmetrical airfoils have been compared in xfoil to determine which one had the least intense wake formation; NACA0012 came out as the best airfoil for this test.

Downstream of the fan, the core structure will remain the same for both cases. The core structure consists of the nacelle downstream of the fan, including its interior equipment, which will be introduced below.

The driving component downstream of the fan is the electrical drive. The selected electrical drive is a Lehner 1950 Carline brush-less motor connected to the fan using a shaft extension fitted over the drive's original shaft. The shaft extension has been balanced in order to ensure stable operation.

A nacelle is placed around the Lehner 1950 Carline motor and fitted with a spherical ball bearing to remove any vibrations induced by the shaft extension. An adaptor piece is mounted on the back of the motor, which can attach the torque and thrust sensors sequentially. The nacelle has been designed to make a smooth transition in the frontal area over the length of the setup, avoiding the introduction of any adverse pressure gradients.

The last aerodynamic addition to the setup is the variable exit, as shown in figure 3.2. The variable exit is a cone that can slide over the nacelle body. Moving the cone will vary the outlet area and thus the mass flow rate. The part is 3D printed and contains markings to indicate at which area ratio the setup is being operated.

The experimental setup has a vertical configuration. The configuration is vertical to avoid any effects of gravity on the measurements, especially while performing PIV or oil flow visualisation. In order to mount the setup vertically, a rig needed to be placed around the setup, as is shown in figure 3.1. The frame consists out of metal beams produced by ITEM. The structure which holds the tube consists out of 3D printed clamps fitted with rubber padding, which hold the tube vertically and take out vibrations if needed. A metal rod supports the weight of the tube and is attached to the frame by 3D printed holders. The rod is attached to a 3D printed basket in which the nacelle sits. The nacelle and tube can thus be turned freely within the frame, making it easier to perform measurements at different azimuthal locations.

The initial constant diameter duct configuration introduced in this section could not obtain the mass flow rate needed to extract the experimental data required. The reduced mass flow rate was a consequence of flow blockage introduced by stalling downstream elements and streamline contraction due to the converging nature of the tube. A design study was performed to map the different effects of the recommendations on the achievable flow coefficient. In figure 3.3 the various cases are represented with their maximal achievable mass flow. The list below shows the different cases depicted in figure 3.3.

- Case 1, constant diameter duct design.
- Case 2, reduced downstream tube length.
- Case 3, flow aligned support struts.
- Case 4, removal of support struts.
- Case 5, constant area duct design.

In figure 3.3 one can see that the operating range in terms of ϕ in case 5 is doubled. For this reason, the remainder of this report uses the setup as shown in case 5. More information on the analysis of the flow blockage and recommendations can be found in appendix A.

Appendix E presents schematics of the uninstalled fan test rig.

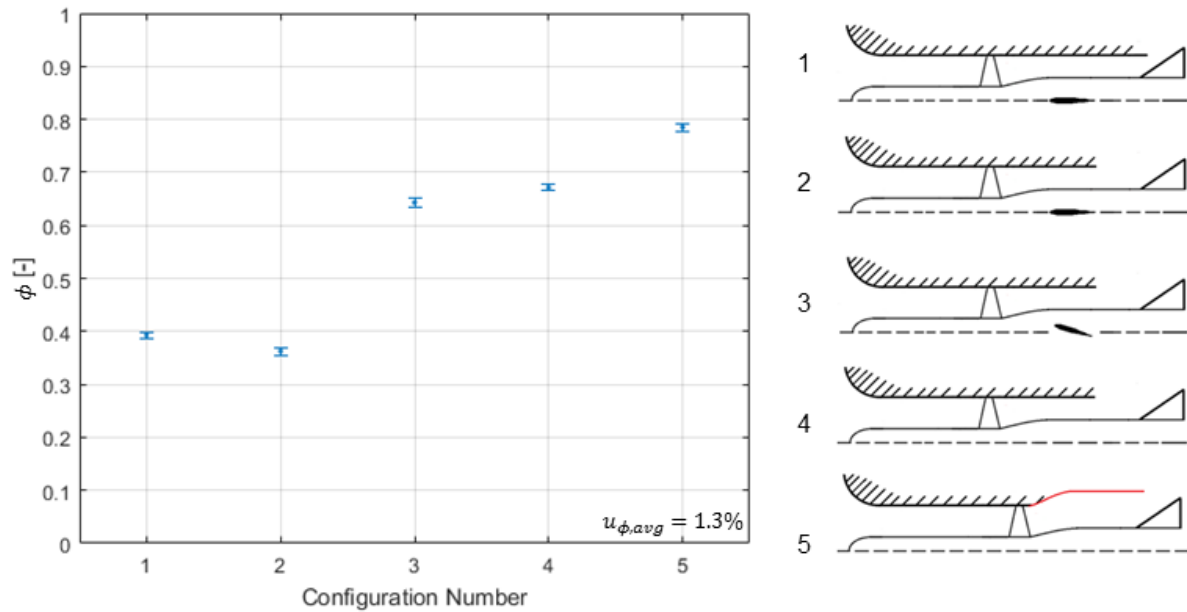


Figure 3.3: Improvement in maximum achievable flow coefficient per recommended case.

3.3. Measurement Techniques

On top of the design of the experimental setup’s structure, the proper measurement equipment had to be selected. In order to do so, it is essential to list which main parameters need to be monitored. In table 3.1 the required outputs of the experiment are listed. Support measurements and calculations will have to be performed to retrieve the values for these parameters. Table 3.2 lists the measured and calculated values note that the means that measurements will be taken at multiple locations, as is shown in figure 3.4.

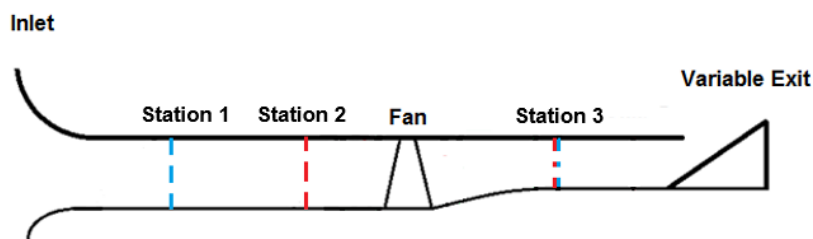


Figure 3.4: Station numbering in uninstalled test fan test rig. The blue lines indicate wall static measurements. The red lines indicate traversing pitot measurements.

Six static pressure ports are installed to measure the static pressure at stations 1 and 3. The pressure ports will measure both the static pressure at the wall upstream and downstream of the fan. This data can be used to monitor if the flow is behaving axisymmetric. The port’s azimuthal locations are evenly spaced; this means that their locations are 0° , 120° , and 240° as shown in figure 3.6.

Parameter	Symbol	Unit
Flow Coefficient	ϕ	[-]
Fan Pressure Ratio	PR	[-]
Blade Loading Distribution	Π	[-]
Corrected mass flow rate	\dot{m}_{corr}	$\frac{kg}{s}$

Table 3.1: Main Output Parameters Experimental Campaign

Parameter	Symbol	Unit	Type
Δ Static pressure*	Δp_s	Pa	Measured
Δ Total pressure*	Δp_t	Pa	Measured
Ambient pressure	p_a	Pa	Measured
Ambient temperature	T_a	K	Measured
Air density	ρ	$\frac{kg}{m^3}$	Measured
Power supplied	$P_{supplied}$	W	Measured
Torque	τ	Nm	Measured
Thrust	T	F	Measured
Rotational speed	ω	RPM	Measured
Velocity	V	m/s	Calculated
Mass flow rate	\dot{m}	kg/s	Calculated

Table 3.2: Support Measurement Parameters Experimental Campaign

Total pressure will be measured with the use of a manual axial traversing system. The traversing system will be measuring different radial positions upstream and downstream of the fan, as is shown in figure 3.5.



Figure 3.5: Axial traversing system in uninstalled fan test rig.

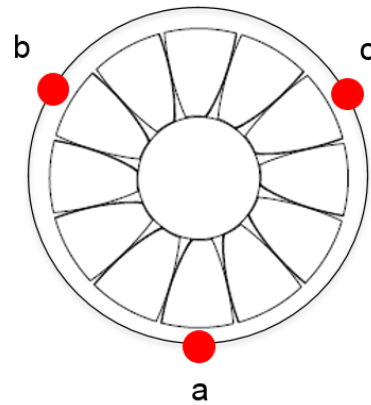


Figure 3.6: Azimuthal station numbering in uninstalled fan test rig.

3.3.1. Scaling Parameters

The pressure measurements are the most important source of data for this experiment. Upstream static and total pressure measurements from station two are used to calculate the axial flow velocity upstream in the tube. This is done with the use of formulas 3.1, 3.2, 3.3, and 3.4 [2]. Another important parameter that can be derived from the pressure measurements is the fan pressure ratio. This reading uses the difference in total pressure upstream and downstream of the fan in stations 2 and

3, as is shown in equation 3.5.

$$p_t = p_s + \frac{1}{2} \rho_a V_x^2 \quad (3.1)$$

$$p_t = p_{t,a} + \Delta p_t \quad (3.2)$$

$$p_s = p_{s,a} + \Delta p_s \quad (3.3)$$

$$V_x = \sqrt{\frac{2(p_t - p_s)}{\rho_a}} \quad (3.4)$$

$$PR_{ref} = \frac{p_{t,3}}{p_{t,2}} \quad (3.5)$$

With the axial velocity known, one can now derive the mass flow rate in the upstream part of the tube, equation 3.6. For the mass flow rate to be used correctly in a compressor map or fan map, the mass flow rate will need to be corrected for varying ambient conditions, equations 3.7, 3.8, and 3.9. Since the reference condition is sea level operation, $T_{a,ref} = 288.15$ K and $p_{a,ref} = 101,325$ Pa [29].

$$\dot{m} = \rho_a A_2 V_x \quad (3.6)$$

$$\dot{m}_{corr} = \dot{m} \frac{\sqrt{\Phi}}{\delta} \quad (3.7)$$

$$\Phi = \frac{T_a}{T_{a,ref}} \quad (3.8)$$

$$\delta = \frac{p_a}{p_{a,ref}} \quad (3.9)$$

Since the setup operates at low speed and has a small experimental scale, it is hard to compare the fan characteristics with the metrics mentioned above. Non-dimensional parameters can be used to gain a better overview of how the behaviour of the fan compares to another scale of operation.

The flow coefficient and load coefficient are used to evaluate the flow behaviour. The formulation of the equations is the same as in the work of S. Tambe et al. [55] which uses a similar setup. The flow coefficient indicates the mass flow capacity of the fan as shown in equation 3.11 and the load coefficient indicates the work capability of the fan as is shown in equation 3.10 [47]. Here, V_x denotes the axial velocity of the flow coming into the fan, and U_{mid} is the tangential velocity of the fan itself. $p_{t,2}$ and $p_{t,3}$ indicate the station at which the total pressure has been extracted.

$$\phi = \frac{V_x}{U_{mid}} \quad (3.10)$$

$$\Pi = \frac{p_{t,3} - p_{t,2}}{0.5 \rho_a U_{mid}^2} \quad (3.11)$$

The power provided will be measured using a data acquisition module linked to the power supply of the electrical drive. The supplied power is monitored to see if any irregularities indicate electrical failures.

3.3.2. Instrumentation

Torque will be measured using a 'Transducer techniques', RTS series, RTS-25 torque sensor. The torque sensor is connected to the motor with the use of an adaptor piece. The torque sensor has a measuring range that is accurate below applied torques of 0.17 Nm. This specific torque sensor has been chosen since it has reasonable accuracy and has a small diameter, which is beneficial for the size of the test section.

The thrust measurements will take place with the help of the Futek Miniature S-Beam Jr. Load Cell. The selection of the thrust sensor was based on availability in the lab. Since the thrust sensor was accurate up to 4.5 N, it is a good match for the experiment.

Data acquisition was completed with the use of Labview and MGMPPro Monitoring. Labview was responsible for logging all the data displayed in table 3.1, except for the RPM. Data was logged time-averaged to compensate for fluctuations in the readings. The measurements were completed time-averaged over 15 seconds with a frequency of 5000 Hz.

The MGMPPro monitoring tool was used for logging the time-accurate data of the RPM of the electrical drive. The RPM was measured continuously throughout a run, and timestamps of the time-averaged data are used to retrieve data later on.

Measuring points were altered by changing the power supplied to the electrical drive and adjusting the tube's exit area.

4

Uninstalled Fan Performance

Following the design of the fan test rig, this chapter will focus on the results obtained in the experimental campaign conducted. In section 4.1, the behaviour of the fan in the setup will be compared to that of its numerical design. The axisymmetric assumption will be tested in section 4.2. Section 4.3 will focus on the difference in the aerodynamic performance of the fan in terms of flow coefficient and blade loading due to the effect of the installation. In section 4.4, the effect of the inclusion of a tail wake will be investigated.

4.1. Fan Behaviour

A compressor map is often used to assess the performance of an axial fan. A classic compressor map shows both the trend of pressure ratio versus mass flow rate and the isentropic efficiency of the system. Due to the low pressure ratio of the fan used in this experiment (around 1.005-1.015), there is little to no heat added to the flow. This, in combination with the lab's considerable temperature fluctuations, caused the estimation of the isentropic efficiency to be impossible. In estimating the fan's performance, only the work addition versus the flow capacity of the system is taken into account.

In the constant area duct experiment, the measured flow coefficient range spanned from 0.4 to 0.8. The previous range indicates that the design condition of $\phi = 0.7$ fits in the fan characteristic map shown in figure 4.1. One can identify a peak in aerodynamic blade loading at $\phi = 0.6$, which reduces when the flow coefficient increases. The high angle slope of the map conforms with the fact that the fan has a high blade solidity [18].

The behaviour on the right side of the peak shows a slight dip and thus exhibits more concave than convex behaviour. In an ideal case, one would expect the line to be straight. In a non-ideal case, the curve would be a bit more convex depending on the intensity of the losses in the system.

Since no stator vanes are present in the system, the swirl angle downstream of the fan can differ per operating condition. The dip in the map shows the limitation of the use of a standard pitot probe. Calibration runs show that the angle of the flow downstream can vary between 20 and 40 degrees, varying with both the radial position and flow coefficient. Figure 4.2 shows a representation of the pitot probe at different angles. The pitot probe has some tolerance in its alignment with the flow but not enough to capture the flow as precise as preferred. Figure 4.3 shows a corrected fan characteristic map. Corrected means that the traversing data of the 20 and 40-degree cases have been combined to create a more realistic map. One can see that the behaviour of the map is now concave, as expected. Another observation is that the blade loading values slightly overshoot the design. It is shown that the slope of the blade loading trend is roughly the same, but the onset of the stall margin

happens at a higher flow coefficient, shifting the experimental case slightly to the right on the flow coefficient axis. Hence, the fan's performance is as expected in terms of blade loading. However, the flow coefficient is on average 5.36% higher to achieve this.

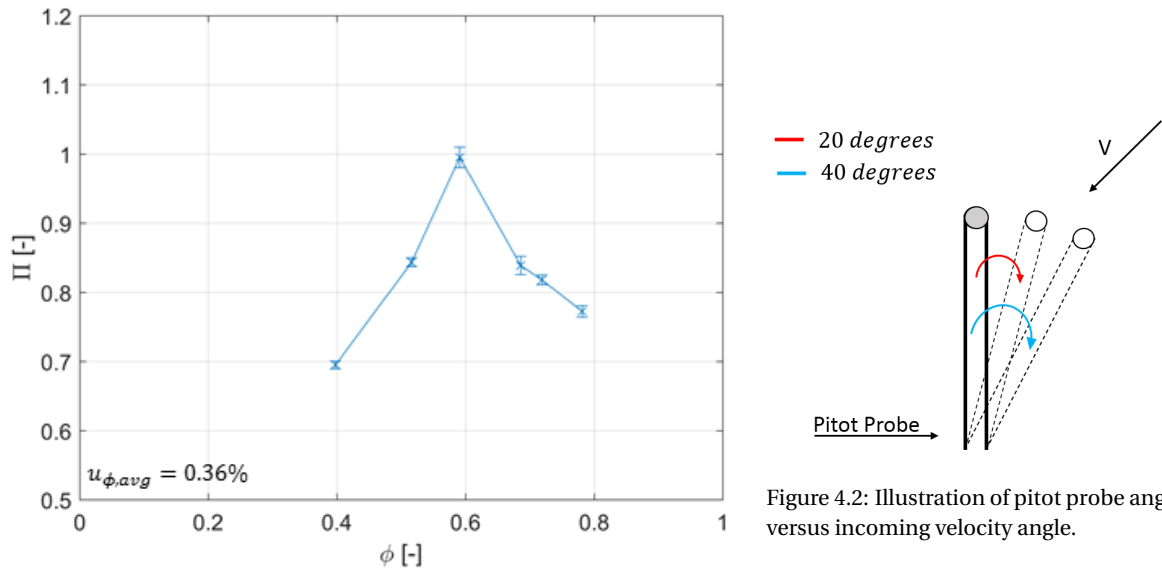


Figure 4.2: Illustration of pitot probe angle versus incoming velocity angle.

Figure 4.1: Normalized fan characteristic map of the uninstalled fan.

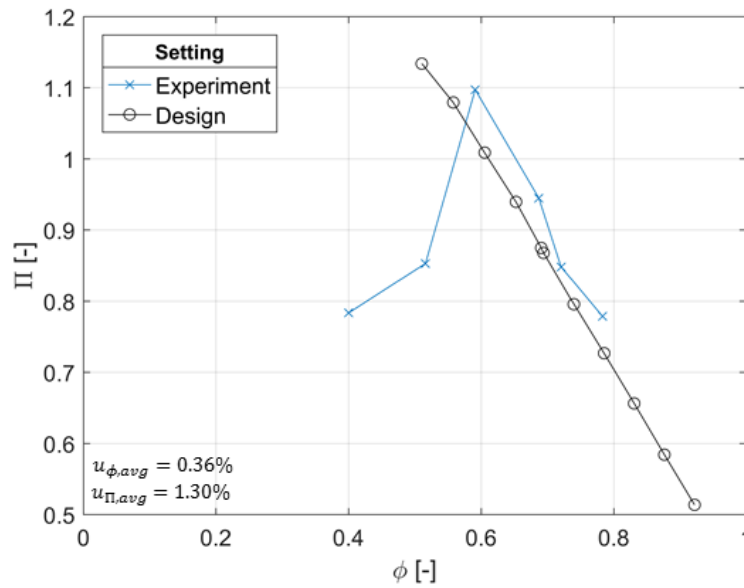


Figure 4.3: Corrected fan characteristic map versus design fan characteristic map

Comparing figures 4.1 and 4.3 shows that the experiment has covered 75% of the stable part of the design fan characteristic map presented in figure 4.3. The fan characteristic map shows that the design condition behaves as expected, within 5.68% of the design value. Table 4.1 shows the remaining design point offsets.

One can see that the stable area of operation is smaller in the actual campaign than in the design case. The peak blade loading in the design case was found at $\phi = 0.5$ and has shifted to $\phi = 0.6$ in the experiment. The discrepancy in stall margin is caused by the inability of CFX turbo, with $k - \omega$

SST solver, to identify the tip losses. In the experiment, tip losses have been accounted for as an important source of loss. The design curve shown in figure 4.3 is a straight line and therefore ideal. Losses are thus not taken into account while they are present in real life.

Π [-]	Design ϕ [-]	Experimental ϕ [-]	$\Delta\phi$ [%]
1.09	0.59	0.54	9.26
0.94	0.69	0.65	5.68
0.85	0.72	0.71	2.12
0.78	0.78	0.75	4.39

Table 4.1: Difference in flow coefficient between CFD design and uninstalled fan test rig corrected fan map data.

Figure 4.1 shows that the compensated fan characteristic map has a better trend shape than the original shown in figure 4.3. The compensated map has been constructed by combining 20 and 40-degree angle data, taking the maximum blade loading for each radial location. This method shows that the actual blade loading is higher than was expected from the design. The primary cause of this rise is the overall shift in flow coefficient discussed above.

It can be concluded that the CFX turbo design simulation cannot capture the actual fan performance. The simulation cannot predict the surge margin and slightly underpredicts the flow coefficient, which matches the blade loading. However, this shift is close to the allowed 5% offset of experimental data and should thus not be considered detrimental. The presented fan characteristic map comparison shows the importance of conducting a real-life experiment to map the actual fan performance. Since the map is sensitive to changes in probe angle, it is recommended to use a five-hole pitot probe to obtain more accurate data in future research.

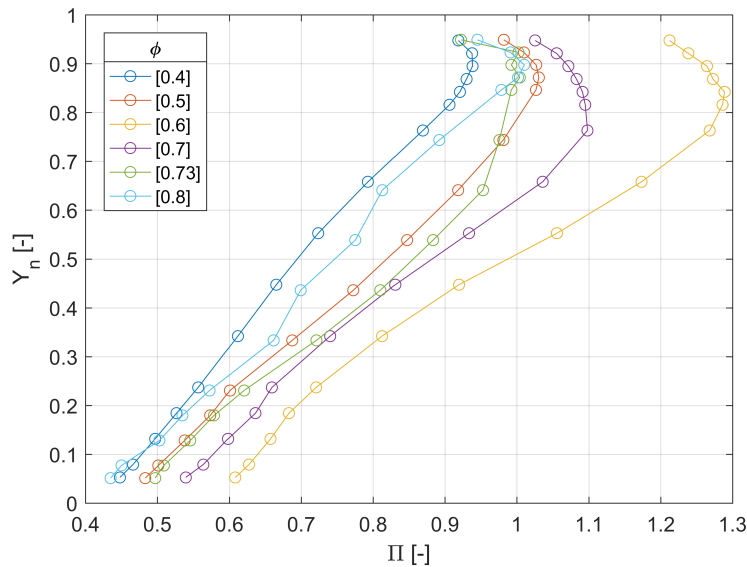


Figure 4.4: Fan blade loading coefficient profiles at various flow coefficient settings.

The fan characteristic maps presented previously are constructed by computing the mass averaged blade loading coefficient from the radial blade loading distribution. The profile of this blade loading is an essential metric of comparison for evaluating installed and tail-on cases and is used as an input for the numerical simulation discussed in section 6.2.

Figure 4.4 shows the corrected uninstalled blade loading profiles with respect to the blade height. From figure 4.4, one can see that blade loading of the tip region changes significantly with the flow coefficient setting, up to 37.39%. The hub region also sees a substantial variation in blade loading, with a maximum shift of 39.87%. Even though the hub and tip region seem to be equally affected by the change in flow coefficient, the blade profiles do show some change in shape. At the design blade loading, $\phi = 0.7$, one can see a fuller curve in the upper part of the blade, $Y_n > 0.6$, whereas the off-design conditions show a sharper curve in that region.

4.2. Azimuthal Variation

In order to check if the assumption of an axisymmetric flow used in the previous sections is correct, azimuthal velocity variation and blade loading maps have been created. Figure 4.5 shows the upstream variation in wall velocity as monitored by the static pressure probes. An almost perfect azimuthal symmetry has been recorded, showing that the incoming flow is behaving axisymmetric. On the map shown in figure 4.6, the azimuthal variation of the mass averaged blade loading of the setup is plotted. The measurements have been taken at design flow coefficient, $\phi = 0.7$. The probe has been radially traversed at various azimuthal locations to identify any fluctuations with respect to location. The readings have been taken with an uncertainty margin of 5%, induced by the manual process of measuring.

Figure 4.6 shows that the flow can be regarded as axisymmetric. The maximum variation in the plot is only 4.89%, which falls within the uncertainty range. The azimuthal position of the probe does not affect the results, and the axisymmetric assumption holds downstream as well.

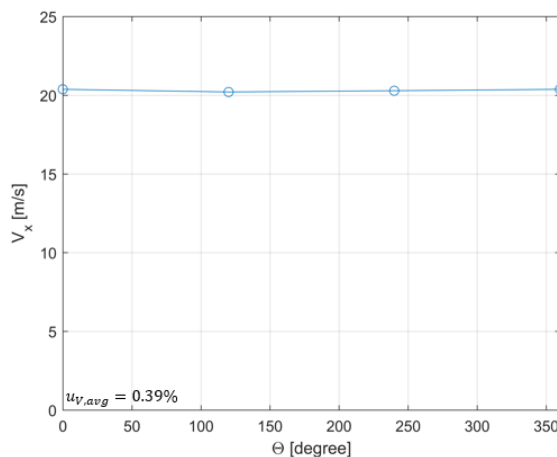


Figure 4.5: Azimuthal variation in velocity at fan inlet (station 1).

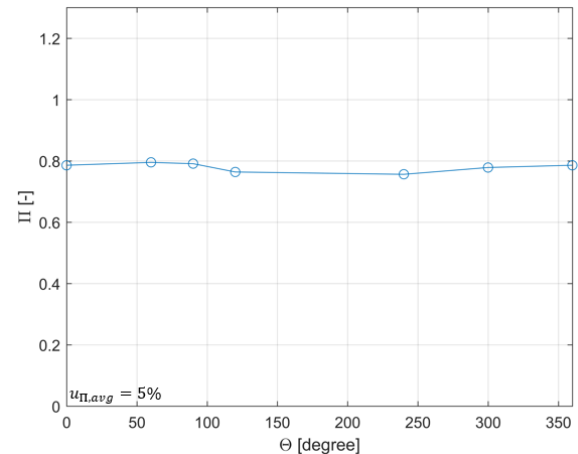


Figure 4.6: Azimuthal variation in blade loading coefficient at fan exit (station 3).

4.3. Installation Effects

One of the goals of this work is to investigate the effect of installation in a propulsive fuselage concept configuration on the fan performance. In order to be able to quantify the effect the installation has on performance, the uninstalled data will have to be compared to installed data. Data on the installed fan performance is available from the work of B. Della Corte [17]. As stated in section 3.1, comparing the uninstalled and installed data grants an insight into the changes in the behaviour of the fan due to installation in a propulsive fuselage concept and can be used to single out problem areas.

In this section, the blade loading coefficient and the flow coefficient are used to determine the

changes in the fan's performance. Performance in this section is thus translated to the capacity of momentum creation and mass flow generation of the fan.

Before any comparison is made, it is important to introduce the two cases and examine their main differences. In figure 4.8, the uninstalled fan case is shown, as was introduced in section 3.2. In figure 4.7, the installed fan test case of B. Della Corte [17] is shown.

The installed case was running at a flow coefficient of 0.7, where $V_x = V_\infty = 20 \frac{m}{s}$. As shown in figures 4.7 and 4.8, the propulsive fuselage concept used in the installed case features a highly curved fuselage, which is used to introduce a large boundary layer to the flow. In the installed setup, the flow was tripped to ensure the transition to a turbulent boundary layer. The second big difference with respect to the uninstalled fan test rig is the introduction of the shroud. The flow will thus encounter a diverging inlet before it enters the fan. At the fan's exit, the flow meets the converging exit between fuselage and shroud, which again can affect the overall fan performance.

Since the uninstalled fan test rig features a constant area duct, it is a good case for comparison to monitor the change in fan performance due to the propulsive fuselage installation.

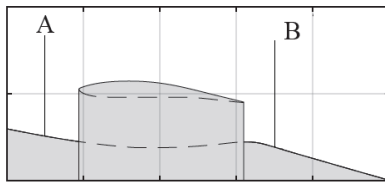


Figure 4.7: Experimental installed setup [17].

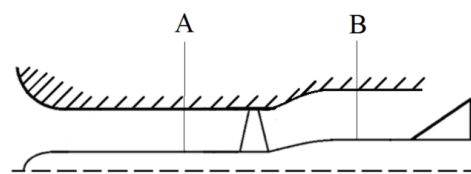


Figure 4.8: Experimental uninstalled setup.

As stated in section 4.2, it can be assumed that the uninstalled fan setup has an axisymmetric nature. The same assumption is made for the collection of the installed data. Because of this assumption, blade loading profiles can be constructed to compare the averaged radial behaviour of the fan in both cases. Equations 3.11 and 3.10 are used to calculate the blade loading and flow coefficient.

The first case of comparison is that of the inlet, indicated as station A in figures 4.7 and 4.8. Measurements at location A will provide the inlet profile of the fan. For the inlet comparison, use will be made of the variation in flow coefficient with respect to the radial location. The radial location has been normalised with the use of equation 4.1, where the radial traversing distance has been divided by the blade height.

$$Y_n = \frac{r}{R_{blade}} \quad (4.1)$$

Figure 4.9 shows the radial distribution of the flow coefficient for the powered and unpowered installed cases and the powered uninstalled case. Both cases are presented at an aimed flow coefficient of 0.7. For the uninstalled case, an average flow coefficient of 0.68 is reached.

One can see that the inlet profile reached in the uninstalled case is reasonably uniform. The wall and hub boundary layers protrude 9.7% and 7.3% into the measuring domain, as shown in figure 4.9. The boundary layer does not create a significant shift in flow coefficient and is thus not expected to impact the fan performance.

However, the effect of the boundary layer on the flow coefficient of both installed cases is more significant. In the bare fuselage case, the configuration is measured without shroud and no fan power. One can see that the flow coefficient drops significantly to 0.46 area averaged at the fan inlet. When considering the powered case, the fan's upstream effect on the incoming boundary layer increases

the average flow coefficient to 0.49. The upstream influence of the shroud also shows at $Y_n = 1.2$. The figure shows that the fan, including the shroud, was completely engulfed in the boundary layer created by the propulsive fuselage concept in the installed case.

Comparison of the installed and uninstalled flow coefficient profiles shows that the fan deals with a drop of 27.66% in flow coefficient, in the case of boundary layer ingestion. In theory, this would bring the fan into the unstable part of the fan map presented in section 4.1.

From this comparison, it can be concluded that boundary layer ingestion can significantly reduce the inlet flow coefficient, having a more distinct impact on the hub section of the fan.

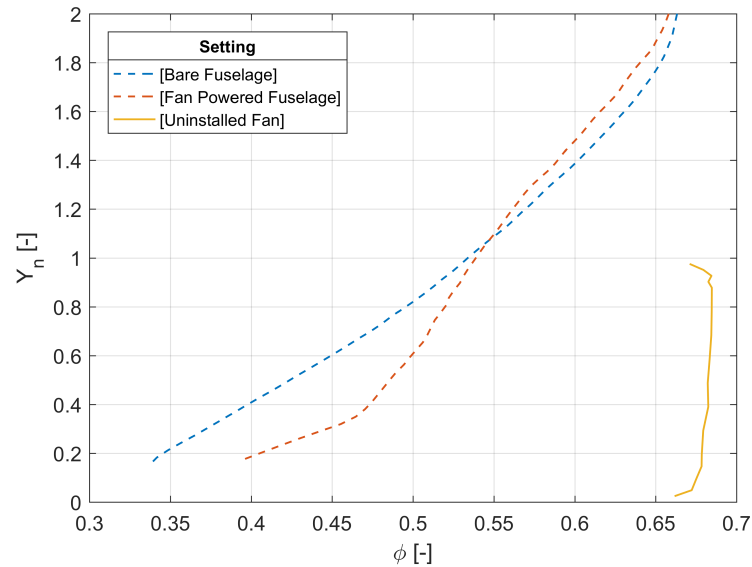


Figure 4.9: Radial variation in inlet flow coefficient, installed versus uninstalled.

The following comparison evaluates the flow at station B. This comparison uses the radial distribution of the blade loading to monitor changes with respect to the addition of momentum to the flow. Following the previous evaluation of the inlet flow coefficient, the comparison will show the installed and uninstalled performances at $\phi = 0.5, 0.6$, and 0.7 . The reasoning behind this is to assess the impact of the incoming flow coefficient with respect to the set flow coefficient. The value of 0.6 has been added to evaluate how the actual blade loading differs with respect to the maximal achievable blade loading.

Figure 4.10 shows the radial blade loading distributions with respect to the normalized radial position of equation 4.1. When comparing the uninstalled profiles of the $\phi = 0.5$ and 0.7 cases, one can see that the average blade loading changes from 0.853 to 0.945 . The profile is shifted to the right, increasing the overall blade loading. The shape of the profile differs significantly as well. The fuller blade loading curve in the upper half of the $\phi = 0.7$ curve is the effect of a more optimal operation mode, as can be found in the fan characteristic map of figure 4.3. The fuller curve in the tip region has a large impact on the mass averaged blade loading for the fan since, at the outer ring, more mass flow is coming through.

The comparison of the installed case with the uninstalled cases clearly shows that the stream tube height has been reduced by 10.25% due to the installation in the propulsive fuselage configuration. Here, the stream tube is defined as the height of the propulsive jet spanning up to the shroud's slipstream. The stream tube contraction significantly impacts the mass averaged blade loading since the profile covers a smaller area. Due to the reduction in stream tube radius, the mass averaged

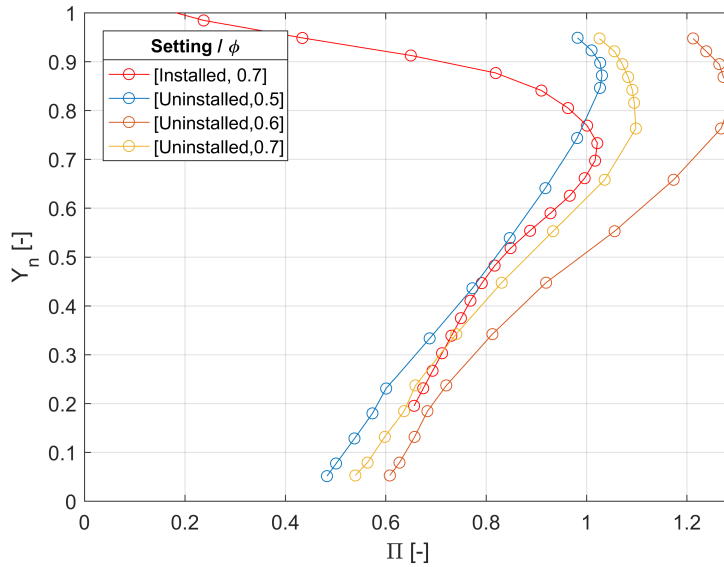


Figure 4.10: Radial variation in exit blade loading coefficient, installed versus uninstalled.

blade loading of the installed case has dropped to 0.755. The latter influences the fan’s performance since less momentum can be added to the flow for the same energy input. When taking the same data set for the $\phi = 0.5$ case, one can see that the difference in blade loading between the two is 15.75%. Note that only the upper 80% of the data is available, and thus only this part has been averaged.

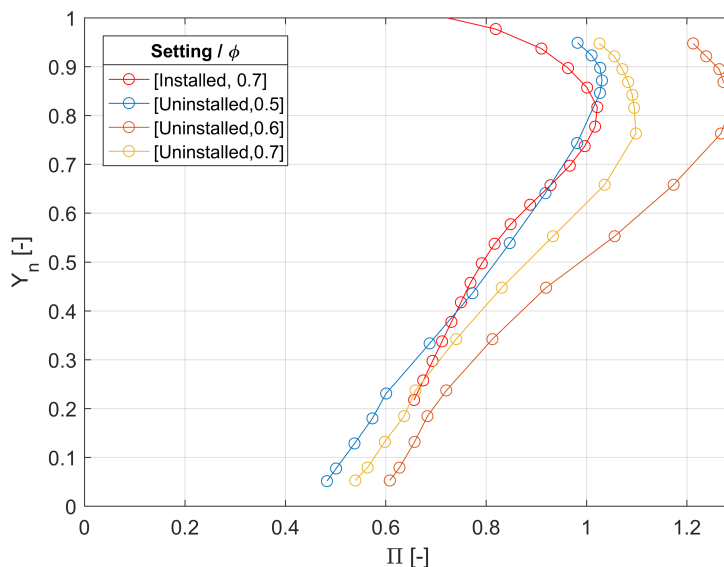


Figure 4.11: Radial variation in exit blade loading coefficient, installed versus uninstalled, corrected for stream tube height.

Since the radius of the stream tube in the uninstalled case is equal to that of the blade height, it is easy to normalise the data. In the installed case, the shroud slipstream caused the stream tube radius to contract, complicating the profile comparison. In figure 4.11 the blade height of equation

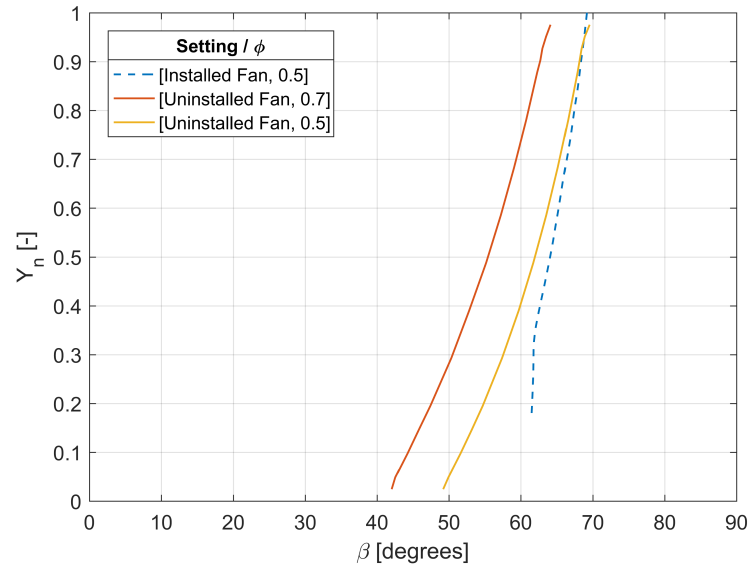


Figure 4.12: Radial variation of incoming incidence angle, installed versus uninstalled.

4.1 has been replaced by the stream tube height to be able to compare the behaviour of the blade loading profiles in greater detail.

In the stream tube normalised comparison of the blade loading distribution, one can see that the installed case indeed behaves similarly to the uninstalled $\phi = 0.5$ case, as was predicted in the inlet comparison. There is still some effect of the shroud wake or slipstream in the tip region, but this is much less pronounced. One can see that the hub region performs better than expected in the installed case. For the available data points between $Y_n = 0.2$ and 0.4 , the difference in blade loading is 4.78%. The performance is increased up until the $\phi = 0.7$ curve.

The increased incidence angle of the flow, due to the incoming boundary layer, causes this shift in blade loading. Figure 4.12 shows the radial distribution of the incidence angle of the flow at the fan inlet. Here one can see a radial increase in incidence angle, with an increased variation at the hub. In the middle region, $Y_n = 0.4$ to 0.8 , the blade loading only differs by 0.09%. The total mass averaged difference in blade loading between the installed and $\phi = 0.5$ uninstalled blade loading is 2.2%.

The latter comparison shows that the installation of the fan in the propulsive fuselage concept decreases the effective slipstream height. Since work is expressed as $\frac{Pa}{m^3}$, the effective work added to the flow reduces due to the reduction in stream tube height with respect to the ideal case. The drop in mass averaged blade loading is 15.75% due to the inclusion of the shroud.

The comparison also shows that installing the fan in a propulsive fuselage concept model benefits the blade loading of the 0.2 to 0.4 y_n region. Unfortunately, the data retrieved from the installed case does not offer enough insight into the profile development towards the fuselage surface.

In figure 4.9, the boundary layer is more pronounced in the region beneath $Y_n = 0.4$. Figure 4.11 shows that the hub blade loading is increased up to this radial position. The fan's available hub section data in this region performs the same as under the $\phi = 0.7$ condition. The increase in incidence angle in the hub section increases the blade lift and thus the blade loading. It is recommended to research the hub section in more detail to investigate how this trend develops towards the wall of the fuselage.

After analysing the in- and outflow profiles of the flow coefficient and blade loading, data shows that the incoming flow coefficient dictates the fan performance. While designing a fan and fuselage

combination, one has to remain on the stable side of the fan characteristic map. It is vital to consider the upstream interaction between the fan and boundary layer and its effect on the operating point in the fan characteristic map.

As stated in section 3.1, the actuator volume used in the numerical part of this thesis uses the pressure profiles obtained from the uninstalled test setup as an input. Section 5.4 will cover the method for obtaining the polynomial functions.

4.4. Tail Installation

The last element introduced in section 3.1 that needs to be covered is the effect of the incoming tail wake on the fan performance. The installed case will be compared to the uninstalled set up where a NACA 0012 tailpiece has been placed upstream in the tube, as shown in figure 4.13.

The installed tailpiece has been designed to create a wake that matches the installed experiment's tail wake. Use was made of the Envisiontech resin printer to create a seamlessly fitted piece in both the tube and the hub section. In this section, the blade loading coefficient from equation 3.11 will be used as the primary performance metric.

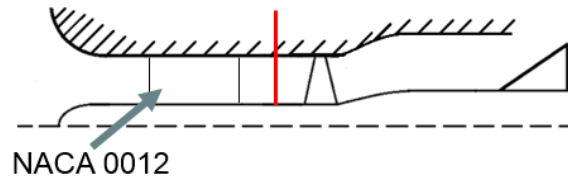


Figure 4.13: Schematic representation of tail position and measurement location in uninstalled fan rig.

The first part of the evaluation focuses on how the tail inclusion changes the fan's inflow profile. A pitot probe has been longitudinally traversed to measure the wake intensity of the flow. Measurements are taken directly behind the tailpiece as indicated in figure 4.13.

The 75% radial position has been selected for traversing since it indicates the mass averaged blade loading best. Since the velocity profiles upstream of the fan are practically uniform, it is assumed that this uniformity also holds for the wake created by the tailpiece. The wake data will thus be extrapolated over the radius of the inflow profile to use in the blade loading equation.

Figure 4.14 shows the wake intensity regarding the tail-mounted cases of the uninstalled fan test rig and the wind tunnel propulsive fuselage. The metric of comparison here is $C_{p,i}$, defined in equation 4.2, where $V_{x,i}$ is the inlet velocity of the fan. The normalised x component represents the wake width divided by the fuselage diameter.

$$C_{p,i} = \frac{p_{t,3} - p_{t,\infty}}{0.5\rho V_{x,i}^2} \quad (4.2)$$

One can see that the normalised width of the tail wakes in figure 4.14 is not equal and that the wake intensities differ. In the installed case, the total pressure in the flow close to the tail does not return to ambient, whereas in the uninstalled case, it does. When only comparing the parts where the wake starts to increase in intensity, the wake width differs by 37.66%. Ranging from $x_n = -0.0077$ to 0.0077 in the installed case, and $x_n = -0.0045$ to 0.0051 in the fan test rig.

The increase in wake intensity is 199% at its peak. A mistake in the tailplane design caused a mismatch in wake intensity. Namely, the wrong normalisation values were taken into account. The

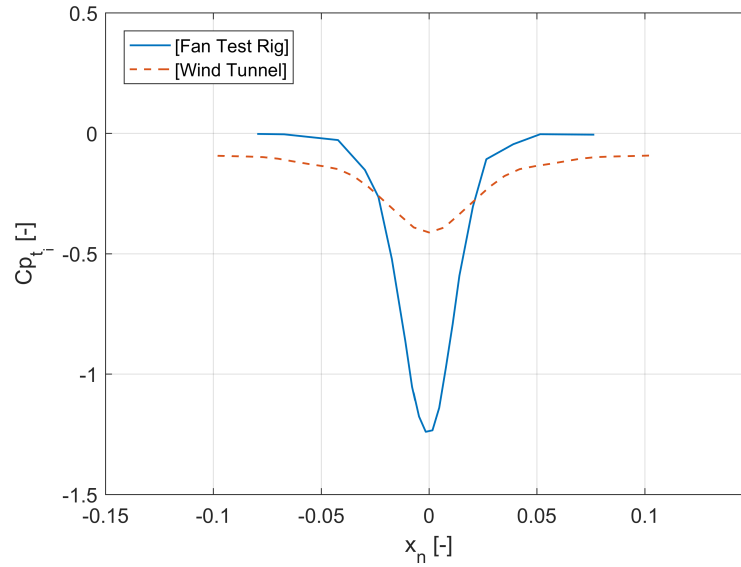


Figure 4.14: Total pressure coefficient profile of tail wake versus normalized wake width. A comparison between wind tunnel and fan test rig data.

comparison in this section will thus not be comparable to the installed case data. Nevertheless, the data obtained can give a valuable insight into the effect of tail installation on the fan's performance. Note that this tail-on case is not included in the numerical analysis because of the inability to compare the two cases.

In order to monitor the effect of the tail wake onto the azimuthal blade loading variation, the mass averaged blade loading has been mapped for various positions, as is shown in figure 4.15. Figure 4.15 also shows the azimuthal variation of the uninstalled case without tail, as was presented in section 4.2.

One can see that the blade loading variation does not change along the circumference of the domain, except for the measuring point downstream of the wake. The difference between the blade loading outside the wake is, on average 1.22%. This deviation falls within the uncertainty margin of 5% of the measurements.

The total pressure measured behind the wake is not affected by the inclusion of the tailpiece. This causes a peak in blade loading measured directly behind the wake, as is shown in figure 4.16, where only the variation in total pressure downstream is depicted. The wake has lowered the inlet total pressure while not affecting the downstream total pressure reading. The fan blade loading has therefore increased by 109.6% at this location. Table 4.2 gives a summary of the change in mass averaged blade loading differences.

Θ [°]	0	60	90	120	240	300
$\Delta\Pi$ [%]	+109.6	-3.21	-1.53	+2.75	-2.36	-1.77

Table 4.2: Azimuthal variation in mass averaged blade loading between tail-on and tail-off case.

A more detailed comparison of the blade loading is shown in figures 4.17 and 4.18, where the profiles of the 0° and 90° azimuthal positions are displayed, respectively. The first figure to discuss is figure 4.18. Here one can see that there is no significant difference in the blade loading profiles outside the wake.

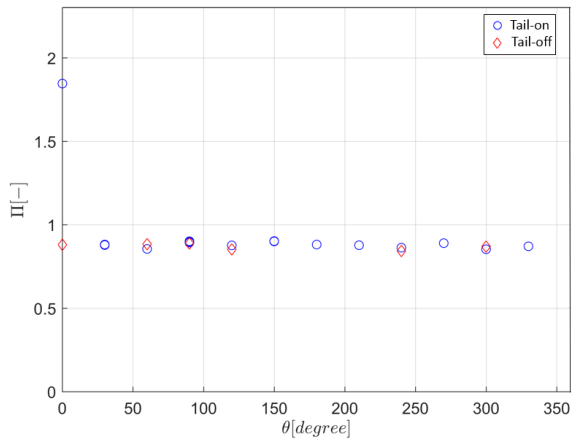


Figure 4.15: Azimuthal mass averaged blade loading variation, tail-on versus tail-off.

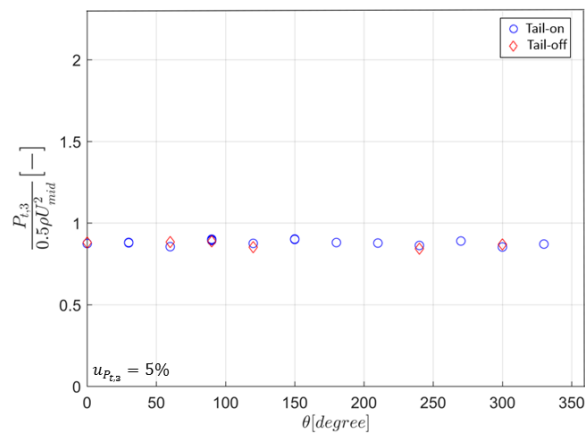


Figure 4.16: Azimuthal mass averaged downstream total pressure variation, tail-on versus tail-off.

In figure 4.17, the radial distribution of the difference at the location behind the wake is shown. Here one can see that the profile has increased by 109.6% in total. At the hub section, from $Y_n = 0$ to 0.3, the profile is most affected (by 149.3%). The tip section, ranging between $Y_n = 0.7$ and 1, is increased by 98%. Figure 4.19 supports the last findings, the incidence angle has been increased along the span of the blade, and the increase in incidence angle is indeed higher at the hub than for the tip region.

As stated previously, the results in this section stem from the fact that the total pressure downstream has not varied. Two specific points mentioned in the previous results call for a speculative discussion. The first point is the fact that the location of the wake now dictates the azimuthal location of the peak in blade loading. Since it was established that the swirl angle of the flow is around 20 to 40 degrees, it seems unlikely that the peak blade loading would be measured precisely downstream of the tail wake. The second point relates to the measurement position. The pitot probe has been traversed one fan diameter behind the fan trailing edge (76.15 mm). The wake has been measured 20 mm before the fan. The fan is thus most surely impacted by the wake, as shown in the flow visualisation of figure 4.20. Traversing measurements positioned closer to the trailing edge of the fan should be considered to rule out if the fan is benefitting from the local disturbance or if the results presented are a result of wake filling caused by viscous diffusion. Nonetheless, the incoming tail wake does not cause an overall deterioration of momentum addition to the flow.

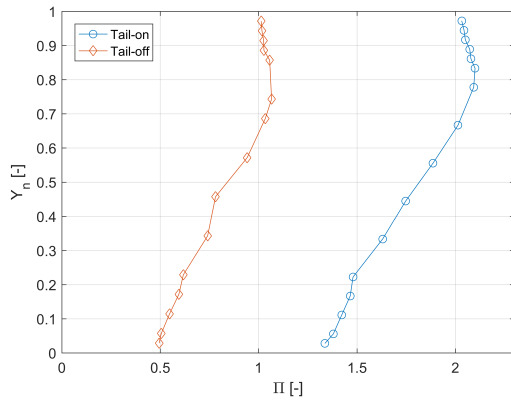


Figure 4.17: Radial variation in exit blade loading coefficient at $\theta = 0$, tail-on versus tail-off.

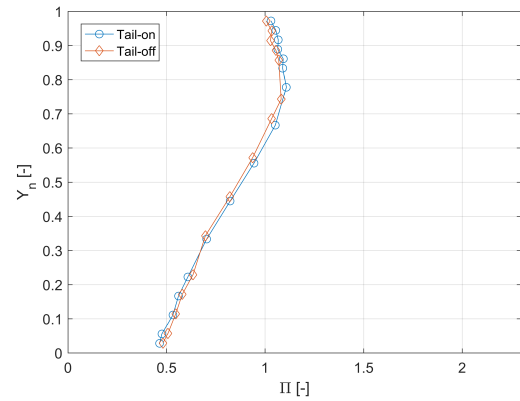


Figure 4.18: Radial variation in exit blade loading coefficient at $\theta = 90$, tail-on versus tail-off.

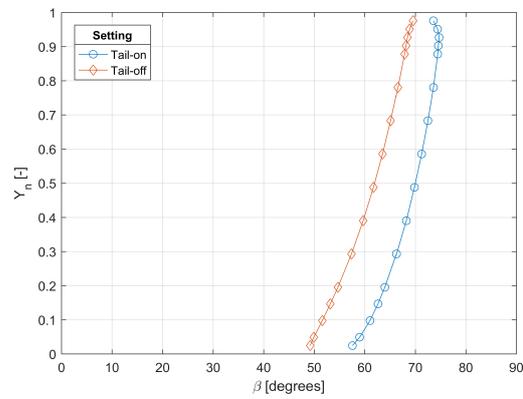


Figure 4.19: Radial variation of blade incidence angle, tail-on versus tail-off.

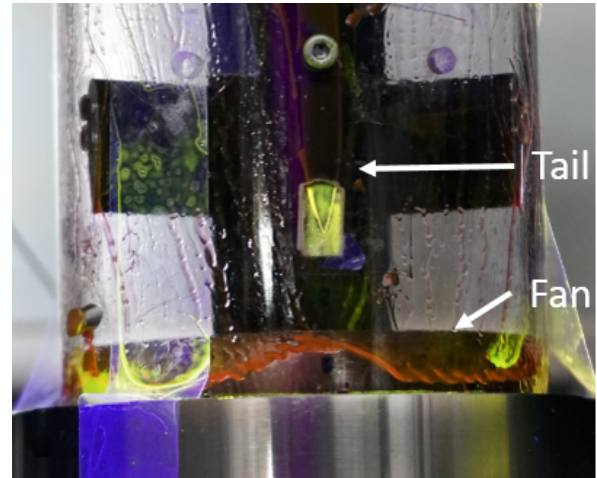


Figure 4.20: Oil flow visualisation of tail wake effect on the fan's tip section.

5

Propulsive Fuselage Concept Numerical Setup

Numerical simulations can provide a valuable tool to analyze a boundary layer ingestion configuration. CFD is a flexible tool that can be used to analyze different setup elements in a limited amount of time. This chapter discusses the numerical simulations performed during this thesis. First, section 5.1 presents the purpose of the numerical simulations. The model and meshing methods are presented in section 5.2, followed by a sensitivity study of the solver settings in 5.3. Section 5.4 discusses the inclusion of the actuator volume. This chapter will be concluded with an introduction of the normalized power balance terms in section 5.5, which will be used for the propulsive fuselage concept analysis.

5.1. Purpose of Simulations

This section will introduce a numerical investigation of the propulsive fuselage concept performance and how the propulsor influences it. This numerical investigation shows the difference between the propulsive fuselage concept operating under installed and uninstalled fan conditions. In the uninstalled case, the actuator volume of the propulsive fuselage concept uses the uninstalled fan data as an input. The uninstalled case gives an insight into the performance of the propulsive fuselage when the fan is not affected by the incoming boundary layer or interactions with fuselage and shroud. In chapter 4, the difference between installed and uninstalled fan performance has been assessed. By comparing the two cases, the losses present due to the incoming boundary layer can be identified.

The numerical simulations answer the research question by serving as a fair comparison for the experimental data. Only the fan's performance changes in terms of momentum source and its radial distribution. The information gained from the simulations will serve multiple purposes, as listed below:

- Assess the difference in boundary layer profiles at installed and uninstalled fan operation.
- Assess the effect of uninstalled fan operation on power balance terms.
- Conclude if the actuator volume approach based on the uninstalled fan data is valid for boundary layer ingestion research.

The first goal of the simulations is to compare the behaviour of the propulsive fuselage concept with an uninstalled actuator volume, based on experimental data, with that of a fan operating in wind tunnel conditions. The delta between the two cases shows the effects of the reduction in momentum source caused by the installation of the fan in the propulsive fuselage concept. Important indicators to assess how the fan behaviour has changed are the axial velocity perturbation ratio $\frac{u}{V_\infty}$ at the inlet and the total pressure coefficient at the outlet. One can see that these terms are similar to the flow coefficient and blade loading coefficient but are now normalized with the free stream velocity.

By comparing the change in the inlet profile, one can assess the upstream effect of a fan operating in installed or uninstalled conditions. A comparison of the profiles at the propulsor outlet shows how the propulsive jet is influenced by the change in fan operation.

The second point on the list is to assess the effect of fan performance on the propulsive fuselage performance. This will be done by comparing the power balance terms of the simulations and the wind tunnel experiment. Discrepancies between the power balance terms indicate which flow phenomena play a significant role in the performance of the propulsive fuselage. By monitoring the effect of the fan performance on the propulsive fuselage performance, the influence of the fan on the propulsive fuselage can be studied. The knowledge gained can help to investigate the strengths and weaknesses of the propulsive fuselage concept.

The last goal of the numerical part of this research is to investigate if the chosen actuator volume approach is sufficient for research in a propulsive fuselage setup. The actuator volume has been selected for this research because the incoming boundary layer should not influence the propulsor in the CFD simulations. If the results of the actuator volume approach a satisfactory, it would reduce the need for an expensive test setup and allow for flexible investigation of the propulsive fuselage concept at varying flight conditions.

Overall, the simulations performed in this research will answer the research question through an investigation of the effect of the fan on the propulsive fuselage performance. With the information gathered from the points mentioned above, conclusions can be formulated on the effect of fan installation on the boundary layer and propulsive jet of the propulsive fuselage. These points can contribute to a discussion of the strengths and weaknesses of the propulsive fuselage configuration.

5.2. Model & Meshing

The validation case for the numerical simulations will be the experimental setup shown in figure 5.1. 3D models of the CENTERLINE and VGM (variable geometry model) aircraft configurations are used to construct the CAD geometry for this research. The VGM is an adaptable wind tunnel model that can be easily converted into different configurations, as has been used earlier in the works of van Arnhem et al. and Kulkarni et al. [31, 58].

The aft body of the CENTERLINE configuration, including the nacelle, is used for the CAD geometry. This geometry is fitted with the front fuselage of the VGM model, as is shown in figure 5.2.

The geometries of the CAD and wind tunnel models do not match because the CENTERLINE wind tunnel model used in previous tests is not modular, while the VGM was. The latter causes the experimental setup to have the fuselage of the VGM with the aft configuration of the CENTERLINE model. The CAD model used in this research uses a modified body to match the scaled length and diameter of the CENTERLINE configuration. In the wind tunnel experiment [17], a different fuselage has been used, which has corresponding slenderness, $\frac{L_f}{d_f}$ [45]. The wind tunnel body slenderness is

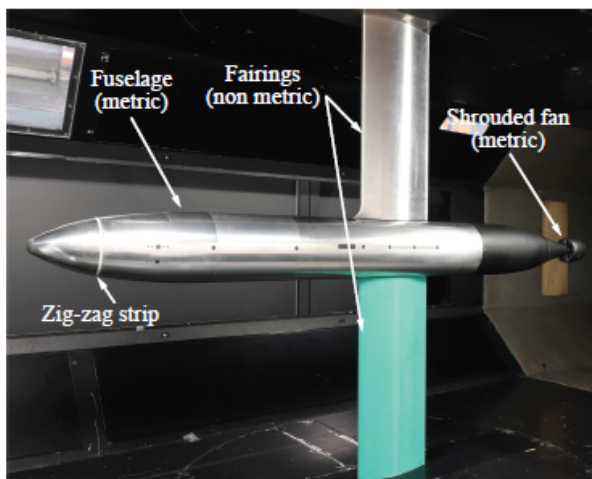


Figure 5.1: Graphical representation of test setup used by B. Della Corte [15].

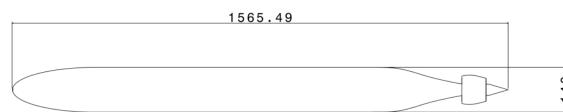


Figure 5.2: Dimensions numerical geometry input [mm].

11.1, while the CAD model slenderness is 11.18.

After importing the CAD model into ANSYS, it is 'cleaned up' in ANSYS Spaceclaim. 'Cleaning up' means that sharp edges and bad faces present in the geometry are removed or repaired to ensure a better basis for meshing. Construction of the enclosure for the fluid domain around the model takes place in Spaceclaim. The enclosure shape matches that of the LTT wind tunnel used in the experiment. The enclosure has an octagonal inlet of 1.25 by 1.8 meters. A representation of the wind tunnel inlet and enclosure size can be found in Appendix C. It has been decided to use the walls of the actual configuration to provide a good validation case that matches the experimental setup's domain. The enclosure walls are modelled without shear stresses to omit the influence of boundary layer formation.

After making the necessary modifications in Spaceclaim, the space discretization of the models takes place in Ansys Meshing. The meshing of the domain has been completed on 180-degree geometries to save computational costs. The problem is assumed to be symmetric, allowing for this approach in all cases with zero side-slip angles.

An unstructured mesh is used to reduce the computational cost of the simulations. The reduced amount of cells of an unstructured grid, with respect to a structured grid, with high flexibility and minor adverse effects on accuracy, offer a good trade-off, especially for complex shapes [22].

The general meshing approach followed in this research was to set up a mesh that captures the boundary layer's flow phenomena in sufficient detail. An iterative process showed that a rather fine grid, above 20 million elements, was needed to minimize the effects of numerical diffusion in the simulations. The unstructured grid was divided into different regions, enabling the mesh to be more refined near the body and in the wake, optimizing the simulation for accuracy and computational time. One of the elements used to refine the boundary layer is an inflation layer around the bodies of interest. This inflation layer satisfies the $y^+ < 1$ condition. As shown in figure 5.3, this will aid in accurately refining the viscous sublayer and subsequent elements of the boundary layer. The initial value needed for the first cell height was calculated with the use of equations 5.1 and 5.2. After running a simulation, the actual y^+ values could be monitored in ANSYS-post to conclude if another iteration on the first cell height was necessary. Table 5.1 shows the resulting first layer cell heights.

$$y^+ = \frac{yu^*}{\nu} \quad (5.1)$$

$$u^* = \sqrt{\frac{\tau_w}{\rho}} \quad (5.2)$$

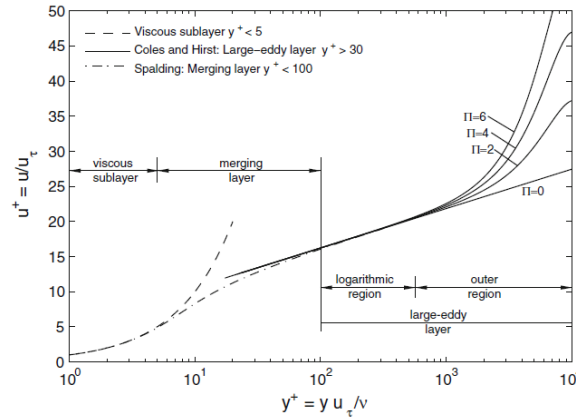


Figure 5.3: Velocity distribution for a turbulent boundary layer [59].

Element	First cell layer height [μm]
Fuselage	14
Shroud	20

Table 5.1: First cell layer height of the prism layers.

During the mesh refinement, the skewness and orthogonality of the mesh elements needed to be monitored. The previous means that the orthogonality should be as close as possible to 1 and the skewness above 0.5 [3, 4]. The formulations of skewness and orthogonality can be found in equations 5.3 and 5.4 respectively.

In equation 5.3, θ_{max} denotes the largest cell angle, θ_{min} the smallest cell angle and θ_e the angle for an equiangular cell. In equation 5.4, vector \vec{A}_i denotes the face normal vector of the cell and \vec{e}_i the vector from the face centroid to the centroid of each edge. All meshes in this work have a minimal amount of low-quality cells.

$$\text{Skewness} = \text{MAX} \left[\frac{\theta_{max} - \theta_e}{180 - \theta_e}, \frac{\theta_e - \theta_{min}}{\theta_e} \right] \quad (5.3)$$

$$\text{Orthogonal Quality} = 1 - \frac{\vec{A}_i \cdot \vec{e}_i}{|\vec{A}_i| |\vec{e}_i|} \quad (5.4)$$

A mesh refinement study has been completed to see if the drag coefficient of the solution converges to the correct solution by reducing the mesh element size. The reduction of the mesh element size was achieved by scaling the local refinements from the baseline case with a pre-defined percentage. In order to monitor the effects of mesh refinement on the outcome of the simulations, the drag coefficient output of the simulations has been compared to reference drag coefficient values. The used reference drag coefficients originate from the experimental setup used by B. Della Corte, a 2D axisymmetric simulation used in the validation of the work of B. Della Corte [15], and an ESDU reference fuselage with the transition point set to the same axial position as it occurs in the simulations, namely 0.18 m. The simulation used for the mesh convergence study consisted out of a Spalart-Allmaras simulation with the most optimal settings found in the sensitivity study, which

will be discussed in section 5.3.

Table 5.2 displays the results of the mesh convergence study performed. It can be observed from the results in this table that the solution is converging. The experimental and 2D axisymmetric cases are the best reference cases because they represent the wind tunnel experiment's actual and validation data. The aim is, however, to be as close to the actual experimental case as possible.

In table 5.2 it is clearly shown that the results of the simulations fall within a reasonable range of the experimental data. Absolute mesh convergence could not be reached because of the lack of computational power. However, when comparing the first coarse step and first and second refinement cases, one can easily see that the results are converging sufficiently.

Case (Cd)	Δ Cell Size	Mesh Elements	Δ Cd Experiment	Δ Cd 2D	Δ Cd ESDU
□ ESDU (0.1333)	-	-	-7.62%	-5.33 %	-
□ 2D (0.1404)	-	-	-2.7%	-	+5.33 %
□ Experiment (0.1443)	-	-	-	+2.7%	+7.62%
Coarse 1 (0.1023)	+50%	13.092.769	28.45%	-27.14%	-30.30%
Baseline (0.1352)	-	21.804.130	-5.47%	-3.70%	+1.42 %
Refinement 1 (0.1352)	-10%	23.132.391	-5.46%	-3.70%	+1.42 %
Refinement 2 (0.1353)	-20%	25.290.080	-5.37%	-3.63%	+1.50 %

Table 5.2: Results of the mesh convergence study. The □ indicates a reference Cd value. ESDU is the value obtained from the ESDU reference fuselage. 2D is the value obtained from a 2D axisymmetric simulation [15]. Experiment denotes the value obtained from the reference wind tunnel experiment [15]. The first column indicates the change in cell size with respect to the baseline. Column two presents the total amount of elements in the grid. The Δ Cd columns indicate the percentage change of the Cd value to the respective value indicated in the row.

The previously discussed mesh convergence study has been conducted on a mesh with only an enclosure without a body of influence. First, a global indication of the mesh convergence with local refinements had to be investigated before adding a refinement zone. In order to be able to capture the behaviour of the flow in more detail, the use of a body of influence might prove beneficial. Figure 5.4 displays the inclusion of the body of influence.

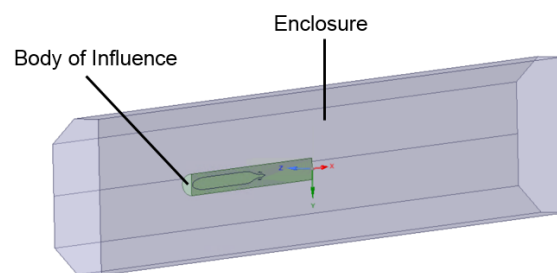


Figure 5.4: Graphical representation of the mesh enclosure with a body of influence.

Table 5.3 shows the mesh convergence results with the body of influence included, which is refined along with the other mesh components. It can be seen that the inclusion of the body of influence has a positive effect on the outcome of the simulation. The difference with the 2D axisymmetric case is lowered by 0.64%, and the difference with the experiment is less than 5%.

The case of mesh refinement 2, with a body of influence, has been chosen to be the mesh to run the final simulations with since it gives the best matching results. Sensitivity studies have been com-

pleted in less refined meshes, such as the baseline case, because of the computational efficiency of these meshes, allowing for more flexibility in debugging and troubleshooting.

Case (Cd)	Δ Cell Size	Mesh Elements	Δ Cd Experiment	Δ Cd 2D	Δ Cd ESDU
□ ESDU (0.1333)	-	-	-7.62%	-5.33 %	-
□ 2D (0.1404)	-	-	-2.7%	-	+5.33 %
□ Experiment (0.1443)	-	-	-	+2.7%	+7.62%
Baseline (0.1352)	-	21.804.130	-5.47%	-3.70%	+1.42 %
Refinement 1 (0.1352)	-10%	23.132.391	-5.46%	-3.70%	+1.42 %
Refinement 1 + BOI (0.1360)	-10%	25.370.977	-4.92%	-3.13%	+1.98 %
Refinement 2 (0.1353)	-20%	25.290.080	-5.37%	-3.63%	+1.50 %
Refinement 2 + BOI (0.1362)	-20%	30.775.477	-4.76%	-2.99%	+2.18 %

Table 5.3: Results for the mesh convergence study including a body of influence (BOI). The □ indicates a reference Cd value. ESDU is the value obtained from the ESDU reference fuselage. 2D is the value obtained from a 2D axisymmetric simulation [15]. Experiment denotes the value obtained from the reference wind tunnel experiment [15]. The first column indicates the change in cell size with respect to the baseline. Column two presents the total amount of elements in the grid. The Δ Cd columns indicate the percentage change of the Cd value to the respective value indicated in the row.

5.3. Sensitivity Study

On top of the mesh convergence study, a sensitivity study has been performed. This study identifies which settings influence the results most. The drag coefficients of the converged solutions have been compared to the reference values mentioned previously.

Settings that could influence the simulation results are the choice of turbulence model, turbulence intensity setting, curvature correction, and the inclusion of Sutherland's law for air viscosity. Other factors can also play a role in acquiring correct results, but they were set to be constant. For example, the inflow velocity and ambient temperature are constant since they are needed to portray a specific scenario. Other values, like constants within the turbulence model or wall roughness height, have been set to default. The previous is because it would complicate the sensitivity study while adding little knowledge about the problem. In future research, one could choose to extend the sensitivity study with more parameters.

In table 5.4 one can see the results of the sensitivity study which has been performed for the different turbulence models. The turbulence models which are investigated are Spalart-Allmaras and $k - \omega$. These models were chosen because they have been widely used in boundary layer ingestion research [8, 15, 25, 30, 33].

The Spalart-Allmaras method is a robust method that handles attached flows very well [28]. Therefore, it seems to be a good option to model the boundary layer flow with this method. As mentioned in the work of Spalart and Allmaras, this model is not intended for use in a homogeneous turbulent flow, but rather in thin shear layers such as the boundary layer [52]. The Spalart-Allmaras method is computationally very efficient since it only deals with one equation. It is also specially developed for the aerospace industry, and its main objective was to predict shock or boundary layer behaviour at smooth surfaces. Using the Spalart-Allmaras method for the viscous sublayer and mixing layer will thus often yield good results as long as the flow does not separate or reattach [28, 52]. Equations 5.5 and 5.6 show how the eddy viscosity in the model is predicted. In this formulation, the left-hand side of equation 5.5 shows the transport equation for the turbulent viscosity $\tilde{\nu}$. On the right-hand side of the equation, \tilde{S} is the strain tensor, ν the molecular viscosity, d represents the distance to the wall, and U is the velocity. In the tripping functions f_{t_1} and f_{t_2} , ω represents vorticity and χ the

turbulence intensity. The default constants used can be found in appendix D.

$$\frac{D\bar{v}}{Dt} = c_{b1}[1 - f_{t2}]\bar{S}\bar{v} + \frac{1}{\sigma}[\nabla((v + \bar{v})\nabla\bar{v}) + c_{b2}(\nabla\bar{v}^2)] - [c_{w1}f_w - \frac{c_{b1}}{k^2}f_{t2}]\left[\frac{\bar{v}}{d}\right]^2 + f_{t1}\Delta U^2 \quad (5.5)$$

$$f_{t1} = g_t \exp\left(-c_{t2}\frac{\omega_t^2}{\Delta U^2}[d^2 + g_t^2 d_t^2]\right) \quad (5.6)$$

$$f_{t2} = c_{t3} \exp(-c_{t4}\chi^2) \quad (5.7)$$

One can also choose to use the strain-based Spalart-Allmaras model supplied by Ansys. In the model discussed previously, the vorticity and strain rate are the same. In the strain-based formulation, however, the vorticity and strain rate are independent of one another [5]. The latter model performs well when the effect of rotation on turbulence needs to be taken into account.

The second family of turbulence models, found in table 5.4, is that of $k - \omega$. As stated in the work of Wilcox, 'two-equation models are complete, i.e., can be used to predict properties of a given turbulent flow without prior knowledge.' [62]. In the $k - \omega$ equations, k is the transport equation for turbulence kinetic energy and ω the transport equation for the turbulence dissipation rate [28]. The turbulence dissipation rate is the rate of transferred kinetic energy from large eddies to smaller eddies; hence it is an effective model to approximate a turbulent flow [62].

In order to create the $k - \omega$ SST model, the $k - \omega$ model needs to be combined with the $k - \epsilon$ model. The latter is the case because the $k - \omega$ model has considerable deficiencies in the wake part of the flow, which the $k - \epsilon$ model has not. On the other hand, the $k - \epsilon$ model renders bad results near the wall and is thus not optimal for approximating boundary layers. Combining the two gives a better approximation of the total flow [39]. However, a weakness of this model is that the model may become vulnerable when facing large pressure gradients in the flow.

In order to model the flow, the viscous sublayer and logarithmic region will be modelled using the $k - \omega$ relations. The $k - \epsilon$ relations are used to model the wake, and free stream region [39]. The relations for the $k - \omega$ SST model are given in equations 5.8 and 5.9 [39]. Equations 5.10 and 5.11 are the necessary additions to the eddy viscosity of the model to create the shear stress, transport model. In equation 5.8, k denotes the kinetic turbulent energy, τ_{ij} the Reynolds stress tensor, ω the specific dissipation rate, and μ the molecular eddy viscosity. Equation 5.9 uses ν_t as eddy viscosity, other constants used in formulas 5.8, 5.9, 5.10, and 5.11 are given in appendix D.

$$\frac{D\rho k}{Dt} = \tau_{ij} \frac{\delta u_i}{\delta x_j} - \beta^* \rho \omega k + \frac{\delta}{\delta x_j} [(\mu + \sigma_k \mu_t) \frac{\delta k}{\delta x_j}] \quad (5.8)$$

$$\frac{D\rho \omega}{Dt} = \frac{\gamma}{\nu_t} \tau_{ij} \frac{\delta u_i}{\delta x_j} - \beta \rho \omega^2 + \frac{\delta}{\delta x_j} [(\mu + \sigma_\omega \mu_t) \frac{\delta \omega}{\delta x_j}] + 2\rho(1 - F_1)\sigma_\omega \frac{1}{\omega} \frac{\delta k}{\delta x_j} \frac{\delta \omega}{\delta x_j} \quad (5.9)$$

$$\nu_t = \frac{a_1 k}{\max(a_1 \omega; \Omega F_2)} \quad (5.10)$$

$$F_2 = \tanh\left(\max\left(2\frac{\sqrt{k}}{0.09\omega y}; \frac{500\nu}{y^2\omega}\right)\right) \quad (5.11)$$

When assessing the results presented in table 5.4, one can see that the regular Spalart-Allmaras model outperforms the other turbulence models. Both $k-\omega$ models over or underestimate the drag coefficient quite significantly. The strain-based Spalart-Allmaras model is underpredicting the drag coefficient more than the regular model, probably due to the overall decreased eddy viscosity production of the model [5]. The Spalart-Allmaras model has therefore been chosen as the primary turbulence model for this campaign.

Case (Cd)	Δ Cd Experiment	Δ Cd 2D	Δ Cd ESDU
□ ESDU (0.1333)	-7.62%	-5.33 %	-
□ 2D (0.1404)	-2.7%	-	+5.33 %
□ Experiment (0.1443)	-	+2.7%	+7.62%
SA (0.1352)	-5.47%	-3.70%	+1.42 %
SA, Strain Based (0.1344)	-6.01%	-4.27%	+0.82 %
K- ω (0.1264)	-11.61%	-9.97%	-5.18 %
K- ω SST (0.1594)	+11.45%	-13.53%	+19.58 %

Table 5.4: Results of the sensitivity analysis for turbulence model selection. The □ indicates a reference Cd value. ESDU is the value obtained from the ESDU reference fuselage. 2D is the value obtained from a 2D axisymmetric simulation [15]. Experiment denotes the value obtained from the reference wind tunnel experiment [15]. The Δ Cd columns show the percentage change of the Cd value to the respective value indicated in the row.

In Ansys Fluent, the user has the option to change the turbulence intensity of the simulation. Since the turbulence intensity can impact the results, a sensitivity study has been set up.

The chosen parameters for this study are the ANSYS Fluent default setting of 0.3, a much smaller value of 0.03 and a much bigger value of 3. Moreover, an estimation of the actual turbulence intensity needed was made with the use of equation 5.12, where the estimated Reynolds number of the lab-scale problem was used [53].

$$\frac{v_t}{\nu} = 2 \times 10^{-7} Re_c \quad (5.12)$$

Although the impact of changing the turbulence intensity is minor, maximal deviations of 0.44% with respect to one another, there seems to be a small local optimum at the calculated value of 0.8. Since this value performs best and has the most solid theoretical background, it is used for future simulations. For simulations at different free stream velocities, the value will be altered according to equation 5.12.

The last variables subjected to a sensitivity study are the inclusion of curvature correction and Sutherland's law for ideal gas density. The reason for the selection of curvature correction is that the 3D geometry used introduces some curvatures along the model wall, especially in the aft body and nacelle or shroud region. The curvature correction option modifies the turbulence production term in order to account for streamline curvature, and rotational effects [6, 54].

The choice to test Sutherland's law stems from the fact that it is a more 'correct' way of modelling the viscosity of an ideal gas, in this case, air. By incorporating Sutherland's law, the effects of temperature are taken into account while determining the viscosity, as is shown in equation 5.13. Note that T_0 and μ_0 are reference values at standard sea-level conditions. S is known as the Sutherland

Case (Cd)	Δ Cd Experiment	Δ Cd 2D	Δ ESDU
□ ESDU (0.1333)	-7.62%	-5.33 %	-
□ 2D (0.1404)	-2.7%	-	+5.33 %
□ Experiment (0.1443)	-	+2.7%	+7.62%
0.3 baseline (0.1352)	-5.47%	-3.70%	+1.42 %
0.03 (0.1352)	-5.47%	-3.70%	+1.42 %
0.8 calculated (0.1358)	-5.02%	-3.28%	+1.88 %
3 (0.1353)	-5.37%	-3.63%	+1.5 %

Table 5.5: Results of sensitivity analysis for turbulence intensity setting. The □ indicates a reference Cd value. ESDU is the value obtained from the ESDU reference fuselage. 2D is the value obtained from a 2D axisymmetric simulation [15]. Experiment denotes the value obtained from the reference wind tunnel experiment [15]. The Δ Cd columns show the percentage change of the Cd value to the respective value indicated in the row.

constant, and T denotes the temperature of the flow [7, 40].

$$\mu = \mu_0 \left(\frac{T}{T_0} \right)^{1.5} \left(\frac{T_0 + S}{T + S} \right) \quad (5.13)$$

Table 5.6 shows the effect of including curvature correction or Sutherland's law in the numerical simulation. Cases 1 and 2 show the inclusion or exclusion of the curvature correction, respectively. The same holds for case 3, which shows the difference in the inclusion of Sutherland's law. The last case, number 4, demonstrates the drag coefficient while both options are enabled.

The results show that Sutherland's law is beneficial for the model, whereas the curvature correction only creates a diverging solution for the drag coefficient. When both features are enabled, they seem to interfere with one another. Therefore, Sutherland's law will be enabled during simulations while curvature correction will be disabled.

Case (Cd)	Δ Cd Experiment	Δ Cd 2D	Δ Cd ESDU
□ ESDU (0.1333)	-7.62%	-5.33 %	-
□ 2D (0.1404)	-2.7%	-	+5.33 %
□ Experiment (0.1443)	-	+2.7%	+7.62%
Case 1 (0.1260)	-12.68%	-10.26%	-5.48 %
Case 2 (0.1356)	-6.03%	-3.42%	+1.72 %
Case 3 (0.1358)	-5.89%	-3.28%	+1.87 %
Case 4 (0.1262)	-12.54%	-10.11%	-5.33 %

Table 5.6: Results of the sensitivity analysis for curvature correction and Sutherland's law. The □ indicates a reference Cd value. ESDU is the value obtained from the ESDU reference fuselage. 2D is the value obtained from a 2D axisymmetric simulation [15]. Experiment denotes the value obtained from the reference wind tunnel experiment [15]. The Δ Cd columns show the percentage change of the Cd value to the respective value indicated in the row.

After concluding the sensitivity study, it can be shown that many parameters need to be monitored to verify the solution. The sensitivity study shows that the Spalart-Allmaras turbulence model with the calculated turbulence intensity level yields the best results. Using this model in combination with Sutherland's law brings the solution even closer to the experimental results.

5.4. Actuator Volume

As stated in section 4.3, a data-based polynomial input is used to model the propulsor. The previous means that the polynomial input is derived from the uninstalled fan data instead of calculating an input based on assumptions. Since the behaviour can be assumed axisymmetric, the actuator volume can be supplied with a single polynomial function. The latter greatly simplifies the numerical setup and reduces computational effort.

The actuator volume has been implemented by creating a separate mesh zone supplied with a momentum and energy source.

As shown in figure 5.5, the actuator volume has been placed at the exact location as the fan in the experimental setup. The volume of the actuator volume has the dimensions of the fan, namely a diameter of 75 mm and a chord length or depth of 17 mm.

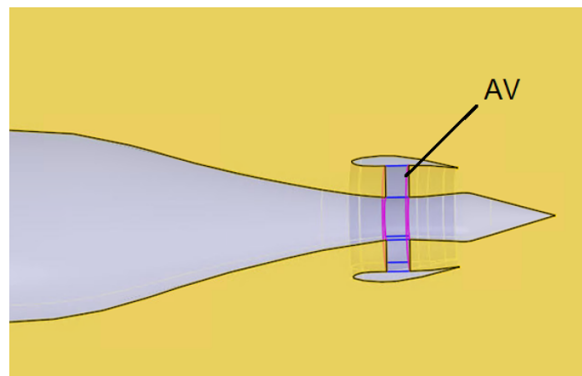


Figure 5.5: Graphical representation of the actuator volume.

The polynomial functions used to feed the actuator volume model were extracted from the uninstalled fan test data presented in section 4.3. The uninstalled fan test data was scaled to match the inlet velocity of the experimental simulation. The scaling was performed using the dynamic pressure from the installed and uninstalled inlet sections. Fifth order polynomials have been used to capture the momentum source profile. The high order of polynomial functions was selected to create a polynomial input representing the actual momentum source in sufficient detail.

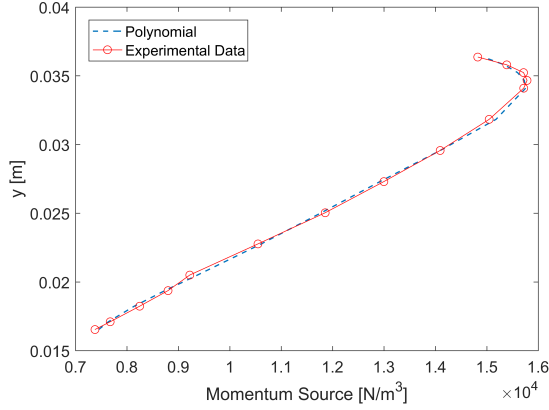
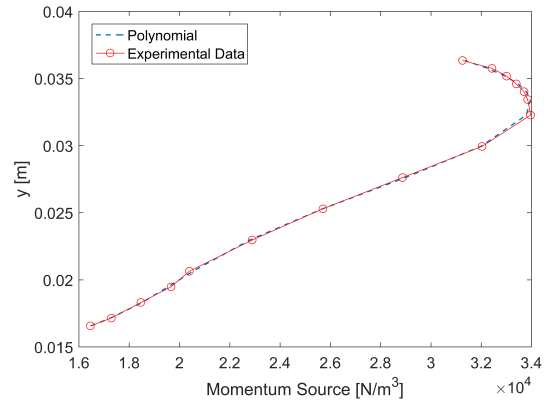
Values for the polynomial coefficients were obtained through the use of the polyfit function in Matlab. Table 5.7 shows the values of the coefficients for the polynomials used in this research. Figures 5.6 and 5.7 show the overlap between the polynomial and experimentally obtained momentum source for a setting of $\phi = 0.5$ and $\phi = 0.7$.

ϕ [-]	p1	p2	p3	p4	p5	p6
0.5	3.76e+05	-7.84e+07	6.58e+09	-2.69e+11	5.46e+12	-4.38e+13
0.7	-3.81e+05	7.67e+07	-5.81e+09	2.13e+11	-3.73e+12	2.46e+13

Table 5.7: Input coefficients for polynomial functions.

The actuator volume is supplied with an axial momentum source. The effects of swirl, introduced by the fan, are therefore not taken into account. The propulsor is thus modelled as if ideal stator vanes are included.

The actuator volume also contains an energy source term in the form of equation 5.15, where the polynomial function of the momentum source is given by equation 5.14. The previous is because the inclusion of Sutherland's law drops the assumption of a constant density and viscosity, enabling

Figure 5.6: Polynomial function overlap at $\phi = 0.5$.Figure 5.7: Polynomial function overlap at $\phi = 0.7$.

the use of the energy equation.

$$M_{source}(r) = p_1 + p_2 r + p_3 r^2 + p_4 r^3 + p_5 r^4 + p_6 r^5 \quad (5.14)$$

$$E_{source}(r) = u(r) * M_{source}(r) \quad (5.15)$$

5.5. Normalized Power Balance Terms

The power balance method, described in section 2.2, will be used to assess the change in performance of the numerical and experimental data acquired. In the reference work of B. Della Corte, the power balance terms have been normalized, making them fit for comparison with cases at different flow settings. In this section, the normalized power balance terms introduced by B. Della Corte are discussed [17].

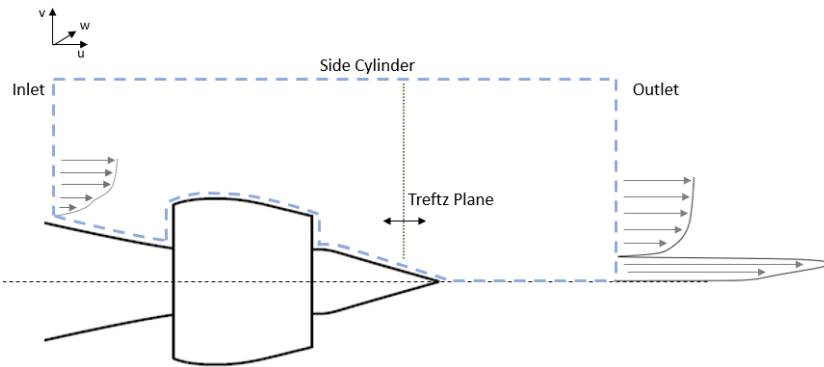


Figure 5.8: Schematic representation of control volume used for the power balance analysis.

All power terms presented are normalized by dividing the power balance terms of Drela, presented in section 2.2, by $q_\infty V_\infty S_{ref}$.

While evaluating section 2.2, it becomes clear that for the control volume case shown in figure 5.8, only P_k or the propulsor mechanical energy will be a contributing factor in the power balance analysis of equation 2.15. Note that this control volume is the one that is used in the analysis of the power terms in later sections.

Equation 5.16 introduces the normalized total mechanical power outflow. C_ϵ is composed of the

axial momentum flux C_{Fx} and the kinetic energy flux $C_{\dot{E}}$, presented in equations 5.17 and 5.18, this is similar to equation 2.16. Here, C_{Fx} is derived from equation 2.21.

$$C_{\dot{E}} = C_{Fx} + C_{\dot{E}} \quad (5.16)$$

$$C_{Fx} = \frac{1}{S_{ref}} \int_0^{L_{TP}} \int_0^{2\pi} \left(C_{pt} + \left(\frac{u}{V_\infty} \right)^2 - \left(\frac{v}{V_\infty} \right)^2 - \left(\frac{w}{V_\infty} \right)^2 \right) r d\theta dr \quad (5.17)$$

$$C_{\dot{E}} = C_{\dot{E}_a} + C_{\dot{E}_r} + C_{\dot{E}_t} + C_{\dot{E}_p} \quad (5.18)$$

As shown in equation 5.18 and 2.16, the kinetic energy flux is divided into isolated power terms. The axial kinetic energy deposition rate is given in equation 5.19 and is derived from equation 2.17. The radial and tangential kinetic energy deposition rates of equations 5.20 and 5.21, originate from the transverse deposition rate given in 2.18. The pressure work term presented in equation 5.22 is related to equation 2.19 of Drela.

$$C_{\dot{E}_a} = \frac{1}{S_{ref}} \int_0^{L_{TP}} \int_0^{2\pi} \left(\frac{U}{V_\infty} \frac{u^2}{V_\infty^2} \right) r d\theta dr \quad (5.19)$$

$$C_{\dot{E}_r} = \frac{1}{S_{ref}} \int_0^{L_{TP}} \int_0^{2\pi} \left(\frac{U}{V_\infty} \frac{v^2}{V_\infty^2} \right) r d\theta dr \quad (5.20)$$

$$C_{\dot{E}_t} = \frac{1}{S_{ref}} \int_0^{L_{TP}} \int_0^{2\pi} \left(\frac{U}{V_\infty} \frac{w^2}{V_\infty^2} \right) r d\theta dr \quad (5.21)$$

$$C_{\dot{E}_p} = \frac{1}{S_{ref}} \int_0^{L_{TP}} \int_0^{2\pi} \left(\frac{u}{V_\infty} C_p \right) r d\theta dr \quad (5.22)$$

The normalization of power balance terms executed by B. Della Corte offers an elegant solution to compare the power terms of different cases. In section 6.1, the normalization will be verified with numerical data gathered at different free stream velocities.

6

Performance of the Propulsive Fuselage Concept

This chapter will focus on the results obtained from the computational fluid dynamic simulations presented in the previous chapter.

The chapter will start with the validation of the numerical model by comparing its bare fuselage results to the experimental bare fuselage data in section 6.1. This section also includes the verification of the normalisation methods used. Section 6.2 continues by investigating the propulsive fuselage concept's boundary layer and power balance terms. In this study, the differences between the powered numerical and experimental cases will be discussed.

6.1. Bare Fuselage Comparison

This section will cover the analysis of the bare fuselage cases. The bare fuselage is described as a shroud-less fuselage, as presented in figure 6.1. The performance of the fuselage itself is plotted to understand the installation effects imposed on the fan and to map the differences among the numerical and experimental approaches.

In this section, the normalisation methods of B. Della Corte will be verified. The difference between CFD analyses and experimental data for the bare fuselage will be introduced, and the simulation's limitations will be addressed.

Two CFD simulations have been compared to verify the total pressure coefficient and the normalised axial velocity component used in this report. One was set at a free stream velocity of $34 \frac{m}{s}$ and the other to $20 \frac{m}{s}$. The $20 \frac{m}{s}$ case was selected as it represents the setting of the experimental results. The $34 \frac{m}{s}$ case was selected since it represents the $\phi = 0.7$ setting for the uninstalled test rig data.

All profiles discussed in this section have been compared to see if the normalisation functioned adequately. Comparison of the boundary layer profiles shows that the normalisation application resulted in a shift of 6% in total pressure coefficient at the inlet. This shift is mainly caused by the physical boundary layer height discrepancy between the numerical and experimental data. Observation of the power balance terms revealed no significant changes. Small shifts took place in the values of the axial deposition rate and the pressure work rate. However, these terms cancelled each other out in the total kinetic energy deposition rate. Therefore, it can be decided that this normalisation can compare data recovered at different free stream velocity settings. Graphical representations of the data comparisons mentioned in this section are presented in Appendix E.



Figure 6.1: Axisymmetric body without shroud.

6.1.1. Boundary Layer Analysis

The boundary layer profiles presented in this section give an insight into the aerodynamic behaviour of the simulated cases with respect to the experimental ones. The total pressure coefficient, defined in equation 6.1, is used to estimate the boundary layer's physical height. Equation 6.1 is also used to map the boundary layer profile. The axial velocity perturbation ratio $\frac{u}{V_\infty}$ indicates the velocity retardation in the boundary layer, which is a relevant term in the power balance terms shown in section 5.5.

$$C_{p_t} = \frac{p_t - p_{t_\infty}}{q_\infty} \quad (6.1)$$

Figure 6.2 shows the first comparison of the bare fuselage case, where the total pressure coefficient of the flow inside the control volume is compared at $\frac{x}{L_{fus}}$ 0.91 and 0.97. These locations match the propulsor inlet and outlet axial positions of the powered case.

The numerical and experimental data correspond well as they show similar trends with little offset. The boundary layer height, indicated as $\frac{p_t}{p_{t_\infty}} = 0.99$, shows a considerable difference shifting from 0.64 to 0.59 for the experimental and numerical case respectively at $\frac{x}{L_{fus}} = 0.97$. The difference in the fuselage radius between the experimental and numerical geometries causes this shift in boundary layer height, as explained in section 5.2. Since the aft section shape and sizing are the same for both geometries, the change in boundary layer height results from the steeper slope encountered by the flow towards the aft section in the experimental case.

Figure 6.3 compares the axial velocity perturbation component of the boundary layer for the experimental and numerical bare fuselage cases. The axial velocity perturbation component is normalised by dividing it with the free stream velocity.

Figure 6.3 shows that the numerical and experimental data coincide well. The effect of the boundary layer height is still visible in this plot, but the overall shift in the mean trend line is -0.0206 in $\frac{u}{V_\infty}$ for the $\frac{x}{L_{fus}} = 0.91$ case, which is a difference of 12.74% with respect to the experimental data. At $\frac{x}{L_{fus}} = 0.97$ the difference between the experimental and numerical data is comparable at 16.92%.

Regarding boundary layer investigation, the numerical and experimental cases show a difference mainly caused by the change in the boundary layer height.

6.1.2. Power Balance Analysis

The power balance terms introduced in section 5.5 are another good merit of comparison to determine how the numerical simulations performed with respect to the experimental data. In figure 6.4 the axial momentum flux is plotted against the axial location $\frac{x}{L_{fus}}$ of the flow, where 1 depicts the tip of the fuselage.

As a consequence of the shift in total pressure coefficient, a mean difference of 7.3% in C_{Fx} can be observed between the numerical simulation and the experimental data at the inlet section between $\frac{x}{L_{fus}}$ 0.9 and 0.94. The numerical data seems to be influenced by the curvature of the control volume,

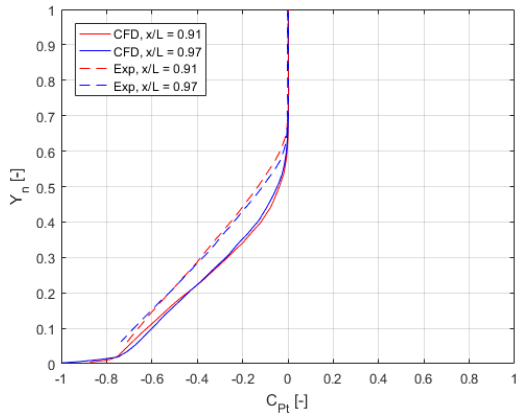


Figure 6.2: C_{p_t} boundary layer profiles of the bare fuselage.

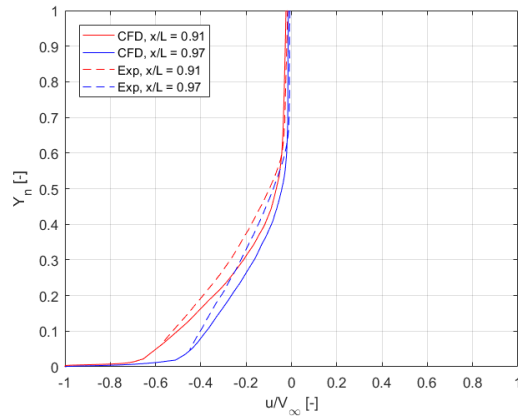


Figure 6.3: $\frac{u}{V_\infty}$ boundary layer profiles of the bare fuselage.

as shown in the region from $\frac{x}{L_{fus}} = 0.93$ to 0.97 . The difference in the Trefftz plane height is the cause of this variation. The numerical Trefftz plane reaches up to the fuselage wall, while the experimental Trefftz plane starts further from the fuselage wall due to PIV reflection issues.

Figure 6.5 displays the difference between mechanical energy flux and kinetic energy deposition rate for both cases. The mean difference in $C_{\dot{E}}$ is 0.0027, which shows that the total deposition rate is predicted well in the simulation. The mean difference in $C_{\dot{e}}$ is 6.3%, which can be attributed to the same reasons as the difference in C_{F_x} .

It can be concluded that the numerical and experimental data can be compared at both boundary layer and power balance level. The differences between the models are relatively small and can be explained by the differences in the geometries, such as fuselage radius and span of the Trefftz plane. A recommendation is to have matching geometries in the future to generate a better analysis. The numerical case can add to the existing data in terms of the control volume by adding information on flow phenomena occurring in the boundary layer close to the fuselage wall.

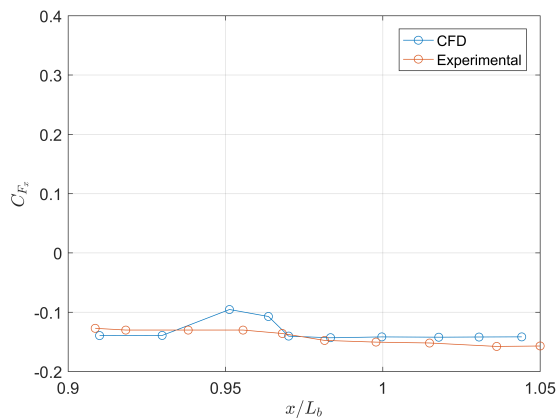


Figure 6.4: Axial variation in C_{F_x} , bare fuselage.

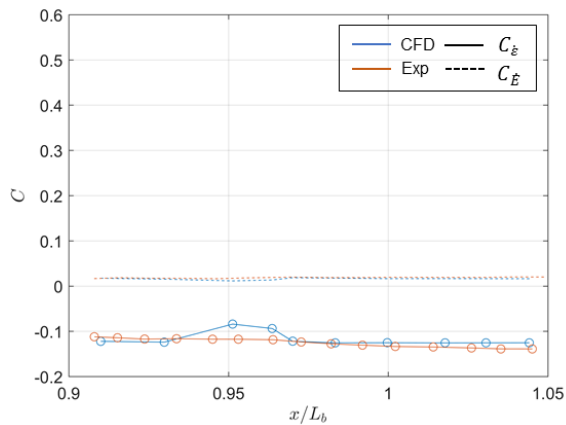


Figure 6.5: Axial variation in $C_{\dot{E}}$ and $C_{\dot{e}}$, bare fuselage.

6.2. Effect of Uninstalled Fan Operation

The numerical models introduced in chapter 5 are used to study the difference between a propulsive fuselage, where the fan operation is influenced by the incoming boundary layer and the one where the fan operation is unaltered. The actuator volumes of the CFD simulations have been supplied with data from the uninstalled fan test to mimic the unaltered fan operation case. In this chapter, the thrust settings of $\phi = 0.5$ and $\phi = 0.7$ are used to investigate how the fan influences the propulsive fuselage aerodynamic flow field and power balance performance.

The setting of $\phi = 0.5$ has been selected because it reflects the true inflow condition the fan is operating in, as was established in section 4.3. The $\phi = 0.7$ condition was selected because it is the design condition of the fan. Examples of contour plots of the CFD simulation for the $\phi = 0.5$ case can be found in Appendix F.

6.2.1. Boundary Layer Analysis

The boundary layer analysis presented in this section shows the difference in boundary layer behaviour between the simulations and experimental data.

Figure 6.6 shows the difference between the inlet boundary layer total pressure profiles taken at $\frac{x}{L_{fus}} = 0.91$. The figure shows that the inlet total pressure profile is not affected by the change in ϕ setting of the propulsor. However, the numerical values do see a shift with respect to the experimental data. The boundary layer height has been reduced from $Y_n = 0.5867$ (experimental) to $Y_n = 0.5355$ (numerical).

There is an overall shift in the upstream effect of the propulsor on the total pressure profile. This shift ranges from -0.591 to -0.488 for the experimental and numerical cases, respectively.

The reason behind this variation has already been determined in section 6.1.1, due to the difference in fuselage radius, the boundary layer height has slightly shifted.

The difference concerning the bare fuselage data presented in section 6.1.1 will be evaluated to gain an understanding of how the experimental and numerical upstream interactions behave. Figure 6.7 shows the experimental and numerical inlet total pressure profiles for both the powered and unpowered cases. BF denotes bare fuselage, and PF represents the powered fuselage, including the fan setting.

The experimental data shows a shift in boundary layer height between the bare and powered case of 14%. The shift in the numerical data is 5.7%, showing that the boundary layer height is more prone to change in the experimental case. The interaction of the fan with the upstream boundary layer differs as well for the two cases. In the experimental case, a mass averaged shift of 4.6% in C_{pt} is measured, showing the minor influence of the fan on the boundary layer. The numerical data, however, shows a shift of 11.7% in the total pressure profile. Moreover, the boundary layer profile shape has been altered, mainly in the Y_n 0 to 0.2 region.

In terms of total pressure distribution, the boundary layer is not affected by the fan setting. The previous can prove beneficial when analysing the inflow velocity profile to dictate which stable thrust setting should be selected for the fan. However, the uninstalled fan operation increases the momentum in the boundary layer, showing that the fan in undisturbed conditions significantly affects the incoming boundary layer shape and intensity.

Figure 6.8 shows the inlet boundary layer comparison for the axial velocity perturbation ratio. In the region from $Y_n = 0$ to 0.3, there is a slight difference in axial velocity perturbation ratio due to the fan setting. As expected, the higher ϕ setting has a slightly more accelerating effect on the boundary layer. However, this upstream effect of 1.2% is disproportionate to the increase in blade loading imposed on the fan (10.7%). The shift in axial velocity perturbation due to the change in fan setting

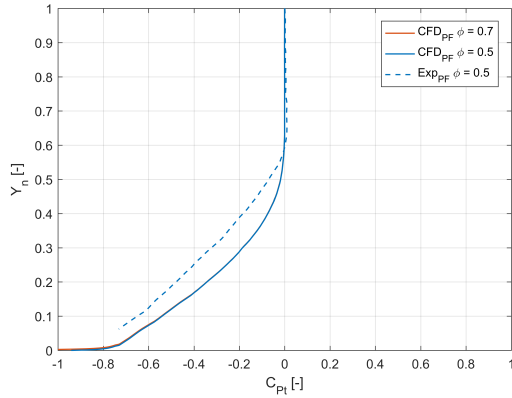


Figure 6.6: C_{Pt} boundary layer profiles at $\frac{x}{L_{fus}} = 0.91$, powered case.

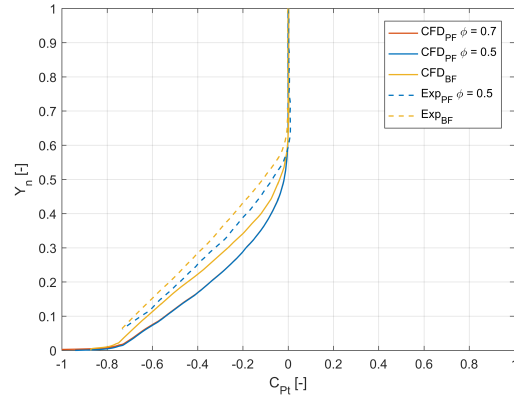


Figure 6.7: C_{Pt} boundary layer profiles at $\frac{x}{L_{fus}} = 0.91$ including powered and bare fuselage data.

is limited to $Y_n = 0.3$. The previous shows that the fan influences the boundary layer only up to the shroud onset. The flow's hub region, up to $Y_n = 0.2$, is affected more by the change in fan setting than the tip region, $Y_n = 0.2$ to 0.3 . The plot shows a slight perturbation in axial velocity at $Y_n = 1$; this perturbation is returning to zero at $Y_n = 2.5$.

Again, the shift with the experimental data due to the non-corresponding fuselage diameters causes the boundary layer profiles to be compared with the bare fuselage results. Figure 6.9 shows the complete inlet comparison of the axial flow data.

In both the experimental and numerical cases, the shape factor of the boundary layer decreases due to the propulsor's upstream influence. In the experimental setup, the shape factor shifts from 1.5 to 1.29 for the bare and powered case, respectively. In the numerical case, it shifts from 1.65 to 1.24. This decrease in shape factor can lead to lower power saving as stated by Smith [51] but leads to more stable operation due to the less adverse pressure gradient. The upstream fan interaction causes the boundary layer to be accelerated.

The upstream influence of the numerical propulsor is quite significant, as the velocity perturbation ratio exceeds the experimental data by 31%. For the axial velocity, it is recommended to take the upstream effect into account while designing the propulsive fuselage concept configuration.

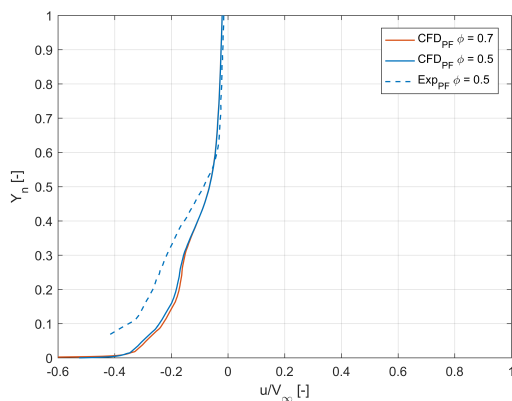


Figure 6.8: $\frac{u}{V_\infty}$ boundary layer profiles at $\frac{x}{L_{fus}} = 0.91$, powered case.

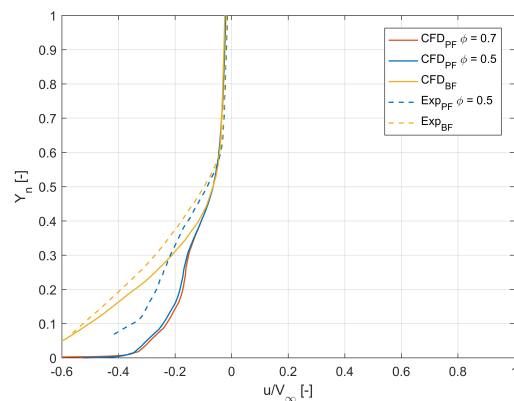


Figure 6.9: $\frac{u}{V_\infty}$ boundary layer profiles at $\frac{x}{L_{fus}} = 0.91$ including powered and bare fuselage data.

The next part of the boundary layer analysis focuses on the outlet of the fan at $\frac{x}{L_{fus}} = 0.97$.

Figure 6.10 shows the radial total pressure distribution at the shroud exit. The plot shows the expected difference in momentum added to the flow due to the change in the fan setting. The difference in total pressure due to the variation in fan setting is negligible in the viscous sublayer of the flow. The discrepancy is minor in the hub region and increases to 6.94% at its maximum at the location of $Y_n = 0.1862$. This behaviour was expected since the most significant difference in blade loading was already shown to be at 80% of the stream tube height in section 4.3, which relates to $Y_n = 0.1862$ in the fuselage diameter scaling. The interaction with the shroud wake is the same for both profiles. Since the inlet profile of the boundary layer is the same for both cases, the nacelle which is engulfed in the boundary layer sees the same acceleration over the top of the shroud, creating a similar wake.

The comparison of the numerical and experimental data at $\phi = 0.5$ shows the effect of the difference in the fan operation. One can see that the experimental profile experiences a reduction in momentum addition to the flow. The overall difference in total pressure addition to the flow due to installation is 10.9%. The tip region is most affected by the incoming boundary layer, with a reduction of 16.5% in maximal C_{p_t} . The experimental data converges to the undisturbed numerical performance in the region closest to the hub, up to $Y_n = 0.5$. As was stated in section 4.3, the most inboard region of the fan produced more thrust under the influence of the higher incidence angle of the boundary layer flow.

Figure 6.10 also shows the discrepancy in boundary layer flow over the shroud. This difference is caused by the boundary layer tripping at the shroud's onset in the wind tunnel. The effect of the shroud slipstream remains more or less the same for the experimental and numerical cases.

Figure 6.11 shows the variation in axial velocity perturbation ratio at the outlet position. Most statements of the previous comparison of the total pressure distribution still hold. However, one can see that the experimental profile's shape differs from that of the numerical profiles. As stated in section 5.4, the actuator volume only adds axial momentum addition to the flow. When evaluating the velocity of the flow in the axial direction, the experimental case will underperform. The decrease in axial velocity is a combination of reduced momentum addition to the flow and the generation of tangential velocity due to the swirl induced by the fan and rotating aft body.

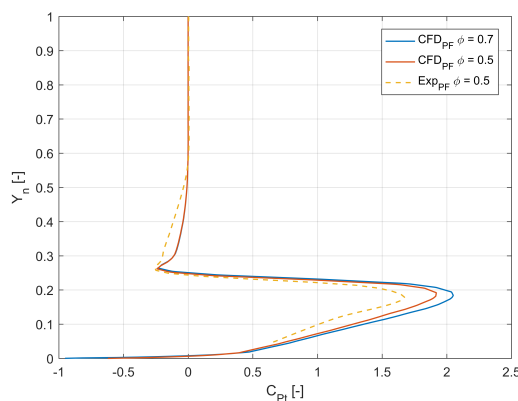


Figure 6.10: C_{p_t} boundary Layer Profiles at $\frac{x}{L_{fus}} = 0.97$.

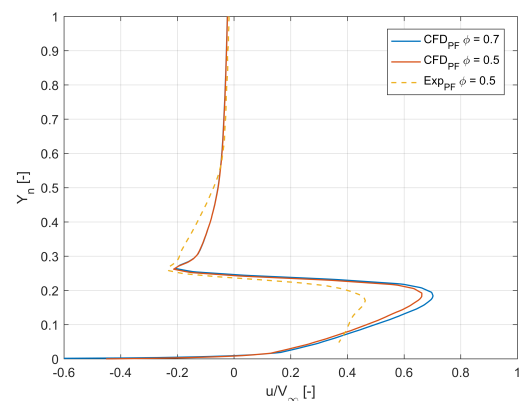


Figure 6.11: $\frac{u}{V_{\infty}}$ boundary Layer Profiles at $\frac{x}{L_{fus}} = 0.97$.

The boundary layer analysis performed in this section shows the effects of the installation of a fan on the aerodynamic flow field of a propulsive fuselage. It has been shown that the upstream flow field is not affected by a change in the fan setting. The actuator volume does increase the upstream interaction with the boundary layer. This interaction should be taken into account in the design process of the fan.

This section has also shown that the installed fan case deals with a decrease in momentum addition

to the flow. The hub region of the fan is less affected due to its operation in the high incidence angle sub-layers.

6.2.2. Power Balance Analysis

The normalised power balance method introduced in section 5.5 will be used to quantitatively analyse the effect of the fan installation on the propulsive fuselage concept.

The first term of equation 5.16 to be evaluated is the axial momentum flux distribution in the flow. Figure 6.16 shows C_{F_x} with respect to the axial location of the flow. Three lines have been plotted, one for the experimental data and one for both ϕ settings of 0.5 and 0.7. The reasoning for this selection is the same as presented in the previous section.

Figure 6.16 shows that the inlet section data of the experimental and numerical simulations differ significantly. This shift, with respect to the bare fuselage case of figure 6.4 can be explained by the fact that the presence of the propulsor has an upstream effect on the boundary layer, in this case increasing the drag upstream. The section spanning the outside of the shroud shows similar behaviour for both the experimental and numerical cases. The latter shows that the boundary layer height may influence the radial distribution of axial velocity and total pressure around the shroud but only slightly increases the drag.

From $\frac{x}{L_{fus}} = 0.97$ onward, the effect of the propulsor on the jet stream becomes visible. The thrust delivered by the numerical propulsor exceeds the experimental propulsor by at least 332%. This large increase is caused by the experimental data operating at a very low thrust. In the numerical case, the thrust present in the wake also dissipates less strongly than in the experimental case.

The difference between the two thrust settings in the numerical simulations is as expected, with a difference of 10.2%. The main reason for the significant increase in axial momentum thrust in the numerical case is that the propulsor only adds axial momentum to the flow, while the experimental propulsor deals with a large amount of swirl and vortex formation in the wake. The previous shows that for a boundary layer ingestion case, one should carefully look at the design of the stator vanes as well as other methods to avoid vortex formation.

The next term of equation 5.16 to evaluate is $C_{\dot{E}}$ or the total kinetic energy deposition rate. As shown in equation 5.18, the deposition of kinetic energy can be divided into four groups. The four groups are the axial, radial, and tangential deposition rate and pressure work.

Figure 6.13 shows the axial deposition rate of equation 5.19. This deposition rate is always positive, except when flow reversal occurs [38]. The numerical cases deposit more axial kinetic energy into the flow closer to the fan inlet. The stronger upstream interaction of the fan with respect to the experimental case causes the increased axial deposition rate.

In the shroud section, no significant changes are identified. Behind the shroud, a large difference can be found in the propulsive jet. The curvature of the fuselage body influences the axial deposition of kinetic energy in the flow in both cases. The mean increase in axial kinetic energy deposition rate of the $\phi = 0.5$ case with respect to the experimental case is 306%, which is in the same range as the increase in axial momentum flux.

The difference between the two numerical fan settings is 16%, and thus more than the increase in axial momentum flux. The comparison of $C_{\dot{E}_a}$ in the jet stream shows that with an increase of C_{F_x} , the axial deposition axial kinetic energy deposition rate does not behave linearly with the change of axial momentum. The behaviour of $C_{\dot{E}_a}$ is also influenced by the curvature of the aft body.

Figure 6.15 shows the axial variation of the radial kinetic energy deposition rate or $C_{\dot{E}_r}$, equation 5.20, in the numerical and experimental cases. The inlet section of the graph shows the increased upstream effect the uninstalled fan performance has on the flow, in this case increasing the radial

deposition of kinetic energy by 47% at $\frac{x}{L_{fus}} = 0.91$ with respect to the experimental data. There is a small shift between the two thrust settings, with a comparable difference to the increase in axial momentum flux at 8.9%.

This behaviour shows that the upstream effect of the ideal propulsor seems to behave quite linearly. The radial kinetic deposition rate is similar in the experimental and numerical cases, both in the shroud and jet wake regions. Most of the radial kinetic energy deposition into the flow is caused by the curvature of the streamlines induced by the shroud or fuselage. Therefore, the momentum excess of the numerical cases causes a slight increase in radial kinetic energy deposition rate.

The last of the deposition rates to discuss is the tangential kinetic energy deposition rate, $C_{\dot{E}_t}$. Figure 6.15 shows the experimental and numerical data derived from equation 5.21. No tangential kinetic energy deposition occurs for both cases in the inlet and shroud section of the plot. The latter because no rotation has been introduced to the flow. However, the tangential kinetic energy deposition is very high in the jet stream of the experimental case. The fan has added the rotation in the jet stream because no stator vanes were used in the experimental setup. The increase in tangential kinetic energy deposition rate over the aft body in the experimental data is created because the aft cone is rotating, contributing as an energy source to the system. The actuator volume does not introduce this rotation and thus does not contribute to the tangential kinetic energy deposition rate.

The total mechanical power outflow from equation 5.16, and the total kinetic energy deposition rate, have been mapped in figure 6.17. Therefore, the comparison in this plot gives a good indication of where losses occur in the propulsive fuselage concept.

The first term to evaluate is $C_{\dot{E}}$, which is the summation of the previously discussed disposition terms and is equal to the mechanical power output of the flow minus the axial momentum flux. This term consequently shows the losses within the system. The larger the summation of $C_{\dot{E}}$, the less boundary layer ingestion benefit can be achieved. Figure 6.17 shows that the inlet section creates some losses which, as previously discussed, are induced by the upstream interaction of the fan with the boundary layer which increases $C_{\dot{E}_a}$, $C_{\dot{E}_r}$, and $C_{\dot{E}_p}$. The cumulative losses in the inlet section are dependent on the fan; the uninstalled propulsor has a larger upstream effect, thus increasing the kinetic energy deposition rates with respect to the experimental case.

As expected, the total shroud losses are small and do not differ between the experimental and numerical cases. The difference in $C_{\dot{E}}$ between the numerical and experimental data is 12.8% for the $\phi = 0.7$ case at $\frac{x}{L_{fus}} = 0.96$, and only 0.8% for the $\phi = 0.5$ case. The kinetic energy deposition rates of the uninstalled propulsor and experimental case are thus similar at the outlet of the $\phi = 0.5$ cases. The decomposition of the contributing factors, however, differs. In the experimental case, the tangential kinetic energy deposition rate is the main contributor due to the absence of a swirl recovery system. At the same time, the numerical terms are raised by the momentum excess present in the flow.

Figure 6.17 shows that uninstalled fan operation reduces the losses in the system, mainly due to an absence of the fan and aft body rotation induced swirl. However, the fan setting does affect the amount of kinetic energy deposited into the flow. The losses in the $\phi = 0.7$ case are 15% higher than in the $\phi = 0.5$ case. The increase in axial kinetic energy deposition rate is the main contributor to this difference.

Figure 6.17 also maps the total mechanical power output in the flow, $C_{\dot{e}}$. The inlet and shroud sections $C_{\dot{e}}$ again behave very similarly in both the numerical and experimental case. In the propulsive jet, a discrepancy can be found due to the increase in C_{F_x} . The mean difference between the experimental and numerical $\phi = 0.5$ cases amounts to 107%. The difference due to the fan setting is 11.5%. The comparison of $C_{\dot{e}}$ clearly shows that in total more mechanical power is added to the flow due to the uninstalled fan operation, and the energy in the flow is more evenly distributed than in the

experimental case. Turning back to figures 6.16 and 6.15, one can see that most of the energy output is related to the tangential deposition rate, thus creating a less even curve. The sharp decrease in $C_{\dot{e}}$ for the experimental case in the wake shows that most of the energy in the flow is being deposited.

As stated earlier, $C_{\dot{E}}$ and C_{F_x} give an indication of the boundary layer ingestion benefit. Figure 6.18 shows a representation of the terms of equation 5.16, evaluated behind the trailing edge of the fuselage. This comparison indicates how the evaluated cases perform with respect to each other at the onset of the fuselage wake at $\frac{x}{L_{fus}} = 1.05$.

The presented data indicates that drag is generated in the fuselage wake of the experimental case. For both numerical cases, a momentum excess is produced. However, the kinetic energy dissipation terms are much lower. The fraction of the total mechanical power dissipated in the wake will be used to compare the performance of each case, $\frac{C_{\dot{E}}}{C_{\dot{e}}}$. For the experimental case, this leads to a percentage of -110% because drag has been generated, lowering the total available power in the flow. The values for the numerical $\phi = 0.5$ and $\phi = 0.7$ cases are 20.3% and 21.2% respectively, showing that the lower thrust setting is slightly more efficient.

The latter is supported by an analysis of the propulsive jet of the bare and powered cases. The numerical data adds 57% more mechanical power output to the flow due to the momentum excess. However, the kinetic energy deposition rate is reduced by 27%, showing that the operation is much closer to the bare fuselage's ideal boundary layer ingestion operation.

It can be concluded that the main effect of the uninstalled propulsor is the increase of axial momentum addition with a decrease in total kinetic energy deposition rate. The absence of kinetic energy deposition primarily causes the decrease of the total kinetic energy deposition rate. Moreover, an increase in axial kinetic energy deposition was observed because of the momentum excess in the propulsive jet. Another observation is that the fan significantly influences the inlet section of the propulsive fuselage concept, increasing upstream deposition rates.

The reduction in axial momentum added to the flow in the experimental case can be attributed to the reduced aerodynamic performance of the and fan scaling of the numerical case. The losses caused by the reduced fan performance have a smaller contribution than the losses due to the swirl. The propulsive fuselage with the uninstalled propulsor input itself is most efficient at a lower thrust setting. In the numerical cases, the flow's axial kinetic energy deposition rate plays the most prominent role.

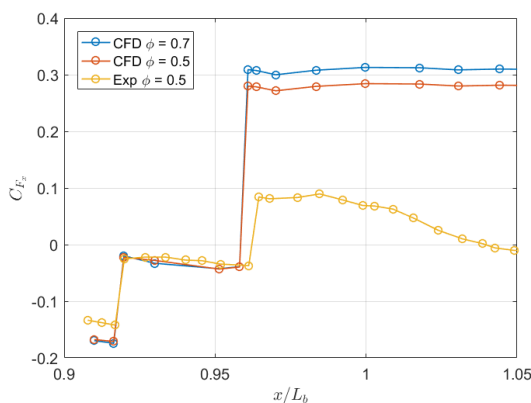


Figure 6.12: Axial variation of axial momentum flux C_{F_x} .

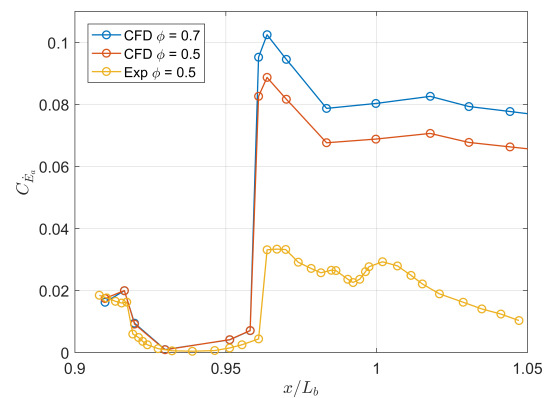


Figure 6.13: Axial variation of axial kinetic energy deposition rate $C_{\dot{E}_a}$.

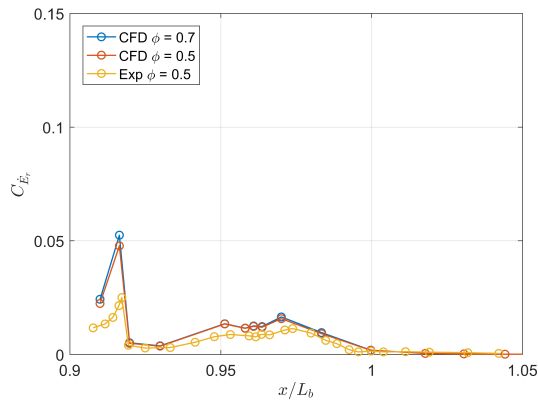


Figure 6.14: Axial variation of radial kinetic energy deposition rate $C_{\dot{E}_r}$.

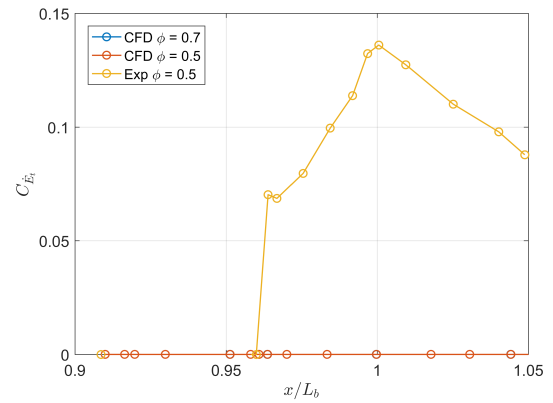


Figure 6.15: Axial variation of tangential kinetic energy deposition rate $C_{\dot{E}_t}$.

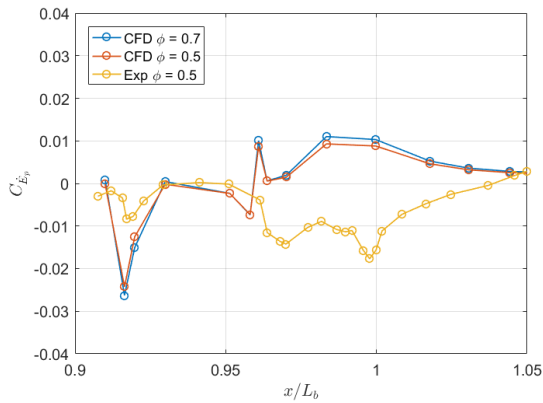


Figure 6.16: Axial variation of pressure work $C_{\dot{E}_p}$.

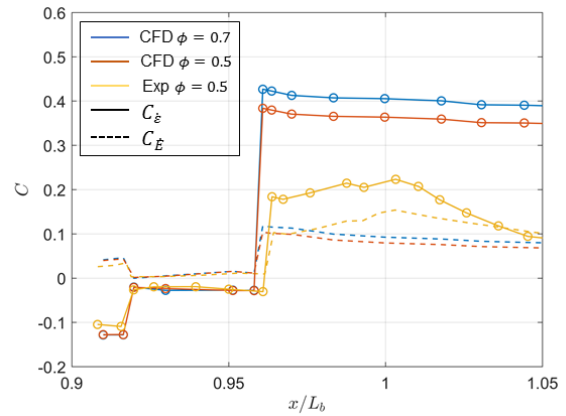


Figure 6.17: Axial variation of total mechanical power output, $C_{\dot{E}}$ and total kinetic energy deposition $C_{\dot{E}}$.

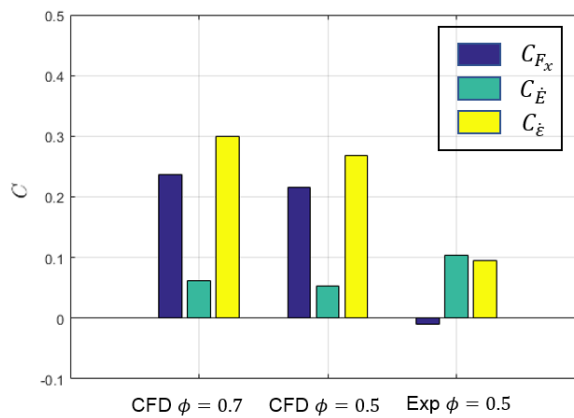


Figure 6.18: Evaluation of composition of the total mechanical power output to the flow at $\frac{x}{L_{fus}} = 1.05$.

7

Conclusions & Recommendations

The final chapter of this report will focus on the conclusions of the performed thesis work and recommendations for further research. The first section will answer the research question and sub-questions. Section 7.2 presents a summary of the observations supporting the conclusions of section 7.1. The last section, 7.3, will cover lessons learned and recommendations for those who wish to investigate fan installation in boundary layer ingestion concepts.

7.1. Conclusions

This research has investigated the effects of the interaction between a fan and a propulsive fuselage. Use was made of two sub-questions to answer the research question.

The first sub-question which has been answered is; '*How does the incoming boundary layer influence the fan's inflow conditions and its addition of work to the flow?*'. The performed research has shown that the main effect of the boundary layer on the fan's inflow condition is the shift of the fan operating point and the introduction of a non-uniform inflow condition. The work addition to the flow has been affected by an overall decrease in blade loading (-2.2%) at the operating point, with an increase in blade loading in the hub section (4.8%).

The second sub-question is; '*How does the fan operation influence both the boundary layer and propulsive jet of the propulsive fuselage concept?*'. Changes in the uninstalled fan operating point cause little to no shift in upstream boundary layer interaction. Moreover, the change in operating point caused an increase in axial momentum flux in the propulsive jet (10.2%), resulting in higher axial kinetic energy deposition (16%) and pressure work (8.3%). The uninstalled fan operation causes a considerable drop in kinetic energy deposition rate in the propulsive jet compared to the wind tunnel operation(-27%). Furthermore, the numerical case increases total mechanical power output into the flow with 57% compared to the experimental case.

The research question can be answered by combining the previous sub-questions and observations made in this chapter. *What effect does the flow interaction between a fan and a propulsive fuselage concept have on their respective aerodynamic performance?* The main effects resulting from the flow interaction between the fan and propulsive fuselage are;

- The fan has a significant upstream influence on the axial velocity component decreasing the boundary layer's shape factor and changing the fan's operating point.
- The fan's upstream influence varies with its momentum addition to the flow, increasing drag and kinetic energy deposition rates upstream of the fan.

- The incoming boundary layer imposes a non-uniform inflow condition on the fan, shifting the fan's operating condition and lowering the blade loading.
- The boundary layer's inboard region significantly increases blade loading in the fan's hub section.
- A momentum excess disproportionately increases the axial kinetic energy deposition rate and increases pressure work in the propulsive jet of the propulsive fuselage concept.
- The increase in total kinetic energy deposition rate is mostly influenced by tangential and axial components, which are affected by the difference in installed or uninstalled fan operation.

Concluding, the fan is indeed affected by the incoming boundary layer. The consequences are, however, minor in low-speed operation. The fan operation, in its turn, influences the boundary layer and propulsive jet. Upstream influences have to be taken into account while optimising the fan. Furthermore, the jet wake should be monitored closely to reduce kinetic energy deposition caused by momentum excess.

7.2. Observations

This thesis was split into two main parts to answer the research question, '*What effect does the flow interaction between a fan and a propulsive fuselage concept have on their respective aerodynamic performance?*'. The first part investigates the effect of the flow interaction between the fan and the propulsive fuselage concept. The second is the study of uninstalled fan operation versus installed fan operation on the propulsive fuselage concept performance.

Uninstalled Fan Test Rig

An uninstalled fan test rig has been developed to compare the behaviour of the fan under the influence of uniform and non-uniform inflow conditions. The uninstalled fan has been compared to its numerical design; this led to the following observations:

- The fan test rig functioned properly in its constant area duct configuration.
- The flow entering the fan and leaving the fan are both axisymmetric.
- The design blade loading was achieved at a higher flow coefficient (5.36%).
- The non-uniform distribution of the swirl angle caused the accuracy of the pressure measurements to decrease.
- The CFX turbo simulation with $k - \omega$ SST solver underpredicted the stall margin of the fan.

Effect of Installation in a Propulsive Fuselage

The effect of installation in a propulsive fuselage concept on the fan performance has been studied by comparing the installed and uninstalled fan data. Comparison of the radial distribution of the in and outflow parameters resulted in the following observations:

- Installation in a propulsive fuselage concept causes the fan operation point to drop from $\phi = 0.7$ to $\phi = 0.5$.
- Comparing at $\phi = 0.5$, the mass average blade loading drops by 2.2%.
- Comparing at $\phi = 0.5$, the inboard section of the blade experiences a rise of 4.78% in blade loading.

Effect of Tail Installation

The effect of an incoming wake on the fan performance has been investigated by placing a NACA 0012 airfoil upstream of the fan in the uninstalled fan test rig. The following observations originate from this investigation:

- The NACA 0012 tailpiece created a wake that does not represent the wind tunnel installed tail wake.
- The total pressure downstream showed no significant variation caused by the incoming tail wake.
- The high local increase in blade loading (109.6%) resulted from the drop in total pressure upstream of the fan combined with a constant total pressure downstream of the fan.
- Further investigation of the total pressure downstream of the fan is needed to determine the effect of the wake on the fan blade loading.

Numerical Setup

The second part of this thesis investigated the effect of the fan operation on the propulsive fuselage concept performance. The latter investigation used the uninstalled fan data as actuator volume input for numerical simulations. The following observations describe the design of the model:

- A high-quality mesh has been generated to perform simulations (+ 30 million elements).
- A prism layer of $y^+ \leq 1$ was used for boundary layer refinement.
- The Spalart-Allmaras turbulence model performed best in the sensitivity study.
- Verification of normalisation methods was successful.
- The bare fuselage behaviour has successfully been validated with experimental data.

Boundary Layer Analysis

An actuator volume was implemented in the simulations, which used data from the uninstalled fan. This actuator volume is used to assess the effect of the fan operation on the propulsive fuselage performance. The experimental data taken at $\phi = 0.5$ and the numerical data at $\phi = 0.5$ and $\phi = 0.7$ has been used for both the boundary layer and power balance analysis. In this way, the difference in performance between installed and uninstalled fan operation could be compared at different operating conditions. The following observations are a result of the boundary layer analysis performed on the gathered data:

- The uninstalled fan increases the upstream total pressure by 11.7%. This shows a rise in upstream influence compared to the installed case where the increase was 4.6%.
- A decrease in boundary layer shape factor was observed, with a more substantial decrease in the numerical case.
- An increase in upstream axial velocity perturbation of 31% was observed in the uninstalled case compared to the experimental case.
- The uninstalled case has increased the total pressure addition by 10% compared to the installed case.
- Inboard the installed fan, an increase in momentum addition was observed.

Power Balance Analysis

Following the boundary layer analysis, the same cases described in the previous section are used in the power balance analysis. The power balance analysis of the flow showed a qualitative analysis of the propulsive fuselage performance for the numerical and experimental cases. The percentage deltas are high in the propulsive jet because the reference case is close to zero. The following observations resulted from this analysis:

- The axial momentum flux increased by 332% while comparing the numerical data to the experimental data in the propulsive jet.
- An increase in the upstream influence of the uninstalled fan was observed, for example, through the increase of radial kinetic energy deposition of 47%.
- Comparison of the delta between the bare and powered configurations for the installed and uninstalled data showed that the uninstalled case deals with an increase of 57% in total mechanical power output into the flow while reducing the total kinetic energy deposition rate by 27%.
- Variation of the flow coefficient shows non-linear behaviour where an increase in momentum excess results in a higher increase in axial kinetic energy deposition rate.

7.3. Recommendations for Future Research

The research presented in this thesis has contributed to the knowledge available on the interaction effects between the boundary layer and boundary layer ingesting fan and the effect of fan performance on the propulsive fuselage concept performance.

In the following, practical recommendations on the experimental and numerical methods and phenomena that could be studied in future research will be given.

Recommendations for further research on uninstalled fan rig testing:

- Measurements have been less accurate due to the use of an individual pitot probe. In future research, a five-hole pitot probe should be used.
- Measurements proved to be slowed down by using a manual traversing system. In terms of accuracy and efficiency, it is recommended to use an automatic traversing system
- Due to time limitations, no use was made of PIV for the fan test rig. In order to gain more insight into the flow's three-dimensional behaviour, it is recommended to include this measurement technique in future research.
- For recording the rotational speed of the fan, the MGMpro monitoring tool was used. This program tends to terminate during operation, which wastes precious measuring time. It is recommended to use a laser or encoder to record the rotational speed.
- For the data retrieved in the experiment of B. Della Corte [17] it is recommended to map the total pressure of the flow field near the fuselage with a five-hole pitot probe. The missing data could prove beneficial in further understanding why the fan performance is increased in the hub section.
- For the tail wake investigation, the total pressure in the flow should be monitored closer to the trailing edge of the fan. This can help identify the actual effect of the wake on the fan and eliminate any influences of wake filling.

The second set of recommendations follows from the second part of the thesis, which focused on a numerical model of the propulsive fuselage concept with isolated fan input.

- Since swirl is the main factor of loss in the experimental setup, it would be helpful to expand the actuator volume model with an introduction of swirl to perform a modular study of the different loss sources in greater detail.
- As stated in the introduction of this report, the aim was to qualitatively investigate the flow interactions between the propulsive fuselage and the fan. It is recommended to scale the simulations to full flight conditions to investigate the propulsive fuselage performance quantitatively.
- The upstream fan interaction has proven to be influenced by fan performance. It is recommended to research how the fan operating condition can be determined, which also influences the inflow condition.

A

Uninstalled Fan Performance in a Constant Diameter Duct

With the experimental setup introduced in chapter 3, multiple campaigns have been run to investigate the uninstalled behaviour of the fan in order to be able to compare it to the installed behaviour measured by B. Della Corte. In this appendix, the results of measurements with the constant diameter tube setup as presented in chapter 3 will be discussed.

A.1. Fan Behaviour

A fan behavioural map of the setup is shown in figure A.1. The coloured lines on the map display the different area settings of the variable exit. The black lines show the speed lines, indicating that the line represents a constant rotational speed setting. In a typical fan map, an example can be found in the work of Hünecke [29], one would expect to see a decrease in pressure ratio while the corrected mass flow is increasing. Hence, the work delivered by the fan reaches an optimum to then decrease with increasing flow capacity. A somewhat diverging solution is found in the experimental data instead of identifying a clear optimum in the graph. All which can be said is that the divergence intensity seems to reduce slightly while a lower rotational speed of the fan is being used.

To further investigate where the unusual behaviour of the presented map comes from, a non-dimensional fan characteristic map has been created, as is shown in figure A.2. The non-dimensional data allows for a better comparison of this case with that of S. Tambe et al. [55] and simulations performed by B. Della Corte. The fan performance in figure A.2 is displaying the same behaviour as found in figure A.1, but now the concave trend line is more explicit.

Note that this graph only shows the speed trend line and that there is hardly any influence of the change in rotational speed on the solution, as expected when normalizing the solution. Only when the nozzle exit is fully open a change can be observed in the form of a higher uncertainty margin. The latter fluctuation could be induced by improper positioning of the exit nozzle during the experiment, which is supported by the fact that this is the only data point with considerable fluctuation in the flow coefficient, namely 3.48%.

Comparing figures A.2 and A.3 shows that the design operating conditions of the fan were not reached throughout the achievable mass flow range of the experiment. Both the flow coefficient and blade loading coefficient prove to be much lower than the design indicated. The maximal flow coefficient reached was 43% lower than the design point. The design blade loading coefficient has been reached; however, since the flow coefficient seems to go into hysteresis at the values where higher pressure rise coefficient values are used, these results will not be considered in the comparison.

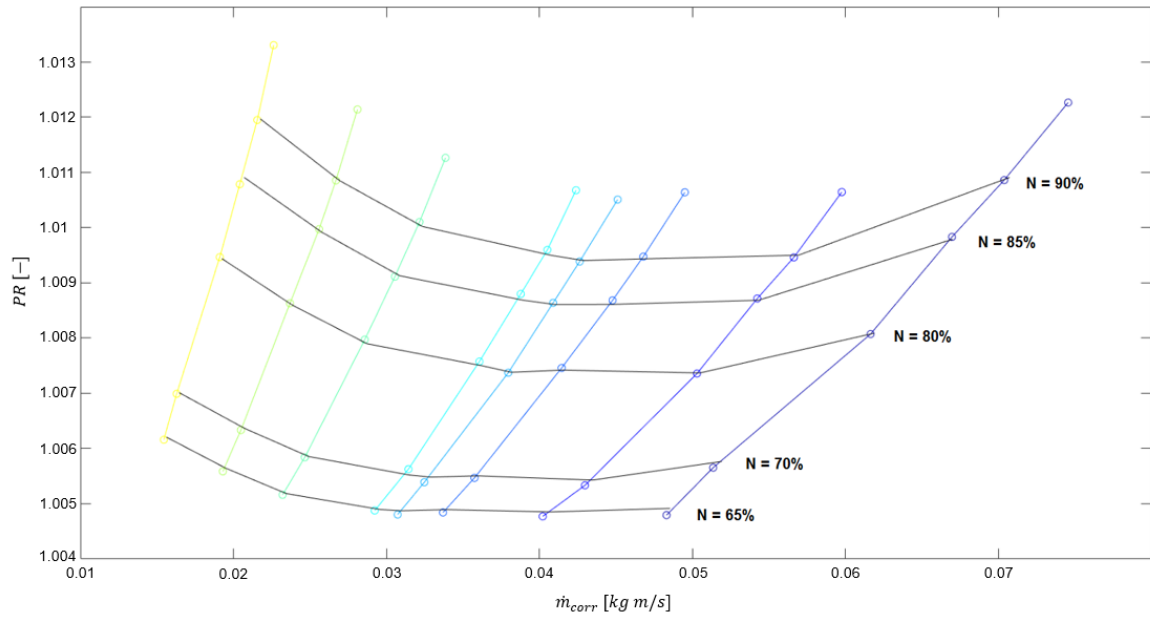


Figure A.1: Initial uninstalled fan test rig compressor map.

A side note is that in a simulation, one can force the mass flow to a pre-defined quantity, whereas in the experiment, the fan needed to create this by operating in favourable conditions. The fan was not able to reach the required flow coefficient, which can be the cause of the unexpected low blade loading coefficient as seen in equations 3.4, 3.10 and 3.11.

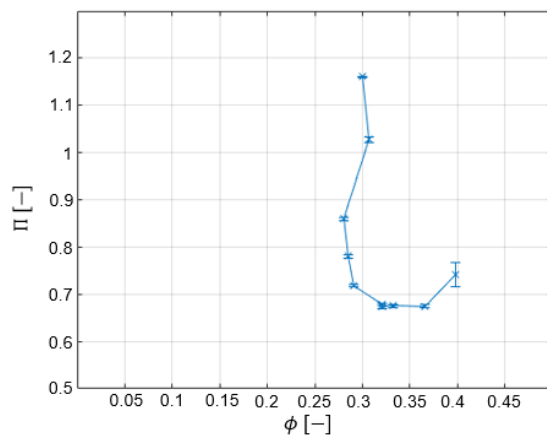


Figure A.2: Normalized fan performance map of uninstalled fan test rig.

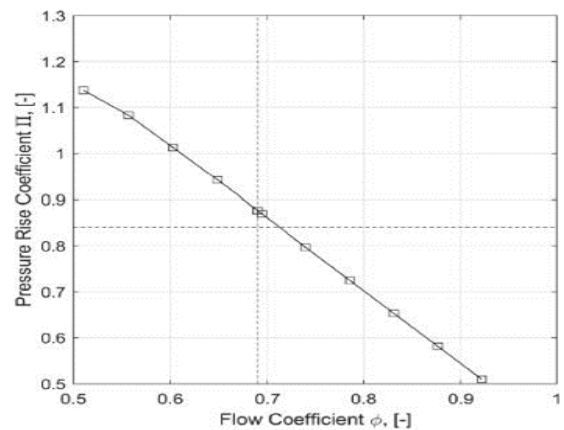


Figure A.3: Normalized fan performance map CFX data (Personal communication B.Della Corte).

A.2. Flow Symmetry

As indicated in section 3.3, static pressure ports have been used to monitor symmetry in the flow at stations 1 and 3 at three azimuthal positions, see figure 3.6. This check was only performed at the $\phi = 0.4$ or open exit area condition, assuming that the behaviour remained constant throughout the experiment. In figure A.5 the results of the comparison at station 1 are shown. It can be seen that

the $\Delta P_{s,wall}$ changes with varying flow coefficient; however, the azimuthal location at which it is measured does not have an effect. The highest measured difference is 2% between position 1 and 2 at 90% of the maximal rotational speed, which is well under the 5% experimental margin, and thus the behaviour upstream in the tube at this condition can be deemed symmetric.

In figure A.6 the same comparison as before is made, but now the static pressure ports downstream of the fan are considered. One can immediately see that position 1 is showing an offset with respect to stations 2 and 3. Here the most significant gap is found at a 95% RPM setting where a 33.87% difference was found. Table A.1 shows a quantification of the plots presented.

First, it was suggested that the pressure port was malfunctioning due to not being precisely flush with the wall. However, the cause is probably inherent to the system since the values remained the same after fixing the port.

As shown in figure A.4, multiple downstream components can create stall cells, such as the struts and the electrical drive cable hub. This stall can lead to a flow blockage with upstream effects, which are picked up by ports b and c. These points are near the blockage's vicinity and located an equal distance away from the disturbance. Since port 'a' is positioned opposite of the disturbance, likely, it does not deal with the same flow disturbance as ports b and c. It is thus clear that the flow downstream is not symmetrical as was expected.

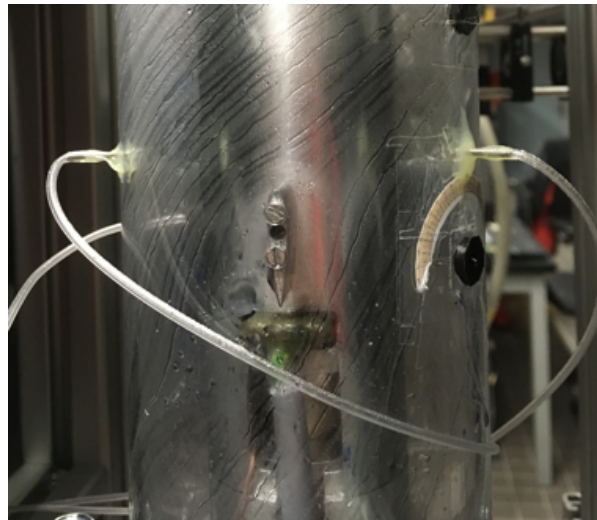


Figure A.4: Illustration of downstream stall cell.

Axial Location	RPM [%]	a/b [-]	a/c [-]	c/b [-]
Upstream	95	1.0167	1.0088	0.9922
Upstream	90	1.0200	1.0100	0.9902
Upstream	85	1.0153	1.0106	0.9954
Upstream	65	1.0140	1.0138	0.9999
Downstream	95	0.6989	0.6613	0.9462
Downstream	85	0.7096	0.6707	0.9452
Downstream	65	0.7153	0.6769	0.9464

Table A.1: Difference in wall static pressure at various RPM settings.

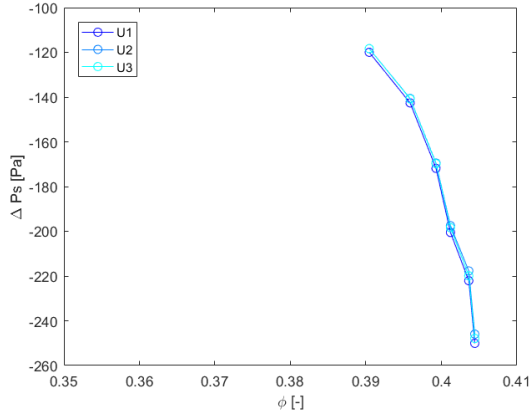


Figure A.5: Variation of static wall pressure at station 1.

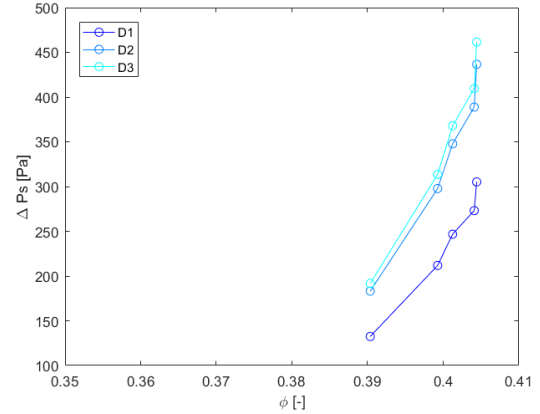


Figure A.6: Variation of static wall pressure at station 3.

A.3. Velocity Triangles

The velocity diagrams of the actual experiment have been compared to those of the design case to understand better the fan's behaviour in the previous two sections. The design case has a mass flow rate of $0.149 \frac{kg}{s}$ with an RPM of 16600. Note that the design case has a constant nacelle diameter equal to that of the hub and a constant tube diameter.

The velocity diagrams have been constructed with the help of basic geometric equations and the assumption that the tangential velocity of the blade is constant at the leading and trailing edge of the blade and that the axial velocity remains constant [18].

The comparison here mainly focuses on the inlet conditions since all relevant data was available from the experiment and the computational design. The calculations are performed at three different blade heights ranging from hub to tip, namely at 25%, 50%, and 75% blade height. The latter is essential to differentiate the behaviour of various blade sections since the blade is highly twisted.

In tables A.2, A.3, and A.4 a comparison is shown of the inlet data of multiple experimental measurement points with respect to the design case. The results show that the fan is not operating at an optimal inflow angle, indicating that the blade has stalled.

From the retrieved data, one can deduce that the fan's RPM setting has little effect on the change in blade inflow angle, max 0.96 degrees at $\phi = 0.4$ and radial position 0.25. The effect of the RPM setting on the blade angle is higher for a higher flow coefficient.

The setting of the variable exit does have a considerable effect on the change in inflow angle, max 22.03 degrees at RPM setting 0.9, blade height 0.25, and $\phi = 0.28$. The relation between the increased inflow angle and the variable exit setting leads to more evidence that the insufficient amount of mass flow leads to unfavourable behaviour, in this case, blade stall.

N [%]	0.7	0.7	0.7	0.9	0.9	0.9
Blade Height [%]	0.25	0.5	0.75	0.25	0.5	0.75
β_1 [°]	63.69	68.84	72.05	62.73	67.94	71.39
$\Delta\beta_1$ [°]	+15.6	+13.82	+12.18	+14.64	+11.52	+11.52

Table A.2: Difference in inflow angle for $\phi = 0.4$.

N [%]	0.7	0.7	0.7	0.9	0.9	0.9
Blade Height [%]	0.25	0.5	0.75	0.25	0.5	0.75
β_1 [°]	68.09	72.54	75.37	67.95	72.53	75.38
$\Delta\beta_1$ [°]	+20	+17.52	+15.5	+19.86	+17.51	+15.51

Table A.3: Difference in inflow angle for $\phi = 0.32$.

N [%]	0.7	0.7	0.7	0.9	0.9	0.9
Blade Height [%]	0.25	0.5	0.75	0.25	0.5	0.75
β_1 [°]	70.12	74.02	76.76	70.06	74.06	76.85
$\Delta\beta_1$ [°]	+22.03	+19	+16.89	+21.97	+19.04	+16.98

Table A.4: Difference in inflow angle for $\phi = 0.28$.

A.4. Discussion of Results

In order to explain why the plots from figure A.2 and A.3 differ so much, figure A.7 from the work of Uddin and Gravdahl [56] can be consulted. The behaviour of the fan used in the experiment seems to display the same trend as the operating conditions of the unstable regime presented in the latter figure.

Even though the unstable behaviour has not been detected during the experimental campaign, the previous sections provided evidence that supports that the suboptimal operation regime was indeed the cause of the unexpected behaviour of the data.

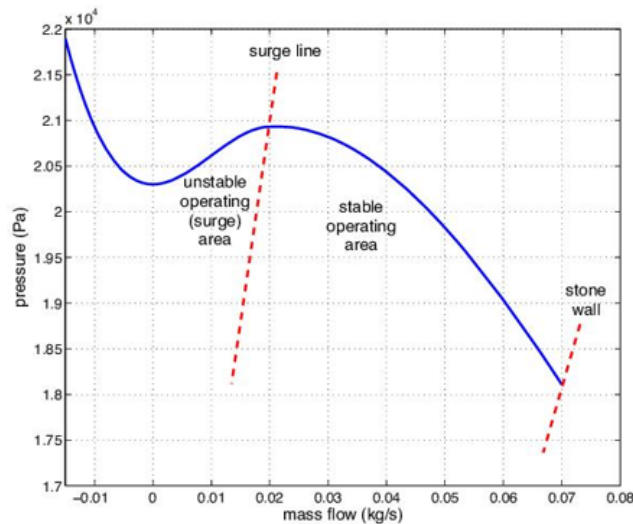


Figure A.7: Fan map including unsteady regime [56].

In the original test plan, PIV would be used to identify the swirl behaviour needed for the actuator disk model. The calibration of the PIV was successful. However, most of the tracer particles ended up sticking on the wall, as shown in figure A.8, this caused the PIV results to be useless. Pictures of the phenomena were taken for further research to discover how the flow behaved. Figure A.8 shows a 'rim' of fluid congregating upstream of the fan. A closer look at the streamlines on the tube shows that the flow on the tube wall was reversed. The reversal was present up until the upstream location of the 'rim'. The occurrence of this rim can indicate the tip stall of the blade, the upstream location of the rim changes with the setting of the variable exit. At the $\phi = 0.4$ condition, the rim is closest to

the fan at about 2 cm upstream of the fan. While reducing the flow coefficient by closing the variable exit, the rim moves away from the fan. At a flow coefficient of $\phi = 0.28$, it touches the trailing edge of the second set of upstream struts. The response of the rim to the mass flow reduction adds to the conclusion that a higher mass flow is needed to be able to get into the stable operating regime.



Figure A.8: Indication of flow reversal upstream of the fan.

Since it can be concluded that the fan has been operating in unstable conditions only, no other results will be presented since they will not contribute to further answering the research question. A second research campaign will have to be executed to retrieve the required data.

The test setup needs to be modified in order to reach the needed flow coefficient. In order to do so, the cause of the flow blockage needs to be identified.

A few recommendations are presented here to relieve the effects of blockage.

The first recommendation is to reduce the tube length of the setup. Since pressure losses in a pipe scale with its length and diameter as is shown in the Darcy–Weisbach equation A.1, it might be wise to reduce any unnecessary losses in the system. Here, λ is the friction coefficient of the material, L is the length of the tube, and D is the diameter. Other quantities include the density ρ and axial velocity V_x .

$$\Delta p = \lambda \frac{L}{D} \frac{\rho}{2} V_x^2 \quad (\text{A.1})$$

The second recommendation is to remove stall cells created by the downstream support struts. Since there are no stator vanes in the setup, the outgoing flow will be swirled. Since the support struts are placed at a zero-degree angle of attack with respect to the hub, the flow is coming into the strut at a very high inflow angle, namely 20 degrees. Aligning the strut with the flow can reduce or

remove the blockage caused by its stall cell. New struts have been 3D printed on the resin printer mentioned in section 3.2, thus having good surface quality. The struts are printed to fit a 20-degree angle of attack position with respect to the nacelle. The hub and tube curvature have been considered while printing to reduce tip or hub losses induced by the strut.

The third recommendation is closely related to the second. If recommendation two is deemed successful, removing the support strut altogether might be beneficial if the system's structural integrity allows for it. Removing the strut altogether would reduce any flow blockage caused by the strut, thus increasing the performance even more.

The last recommendation is to either reduce the nacelle area or increase the tube area downstream of the fan. This is because the flow is now being pushed through a converging duct. The previous leads to a contraction of streamlines and thus causes the flow to accelerate downstream of the fan. If the streamlines can remain constant, the effective area which can be varied is more extensive, leading to a broader range of flow coefficients that can be reached.

Decreasing the nacelle diameter will prove to be difficult since it sits tightly around the motor and is already sized to its minimum. Moving the motor more aft of the fan will be complex since the shaft extension will become too long, inducing the need for more bearings to reduce vibrations. It thus seems more feasible to enlarge the duct downstream of the fan. This could be done with a connector piece with the same slope as the nacelle. It expands to a duct with a diameter that will leave the same area for the flow to go through upstream. Said connector pieces can be manufactured from aluminium or can be 3D printed to save time and money.

In the second campaign which has been run, the recommendations mentioned previously have been implemented. Figure A.9 shows the result of the maximal reached flow coefficient of each of the proposed design changes.

The figure shows that the reduction of the tube length does not have a favourable effect on the flow coefficient. The assumption that friction losses are the cause of the reduction of mass flow is proved wrong. The shorter tube length probably caused blockage effects near the exit to be increased a bit due to the struts being closer to the exit.

The effect of tilting and removing the strut can be found on points 3 and 4. Where an increase in flow coefficient of 49.92% is reached. The assumption that the presence of the strut caused a large part of the flow blockage was correct.

The last recommendation is shown in point 5; increasing the effective trough flow area increases the flow coefficient by another 14.46%.

From the previous results, it can be concluded that configuration 5 is the optimal configuration. The mass flow has been increased by removing the cause of downstream flow blockage with the increase of effective duct area.

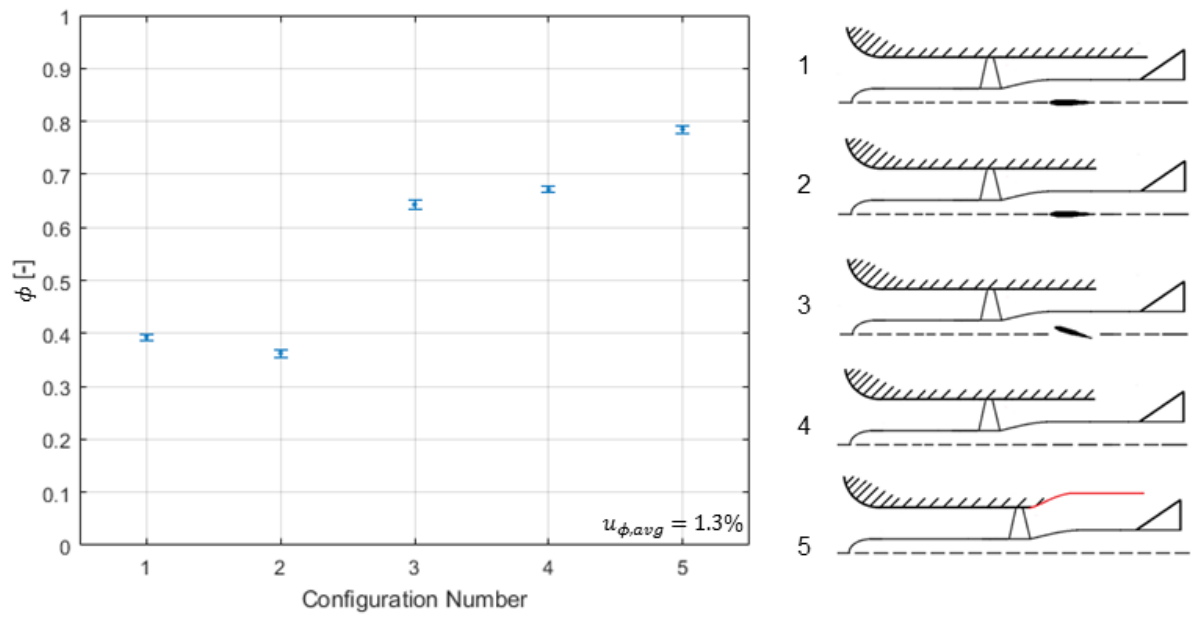
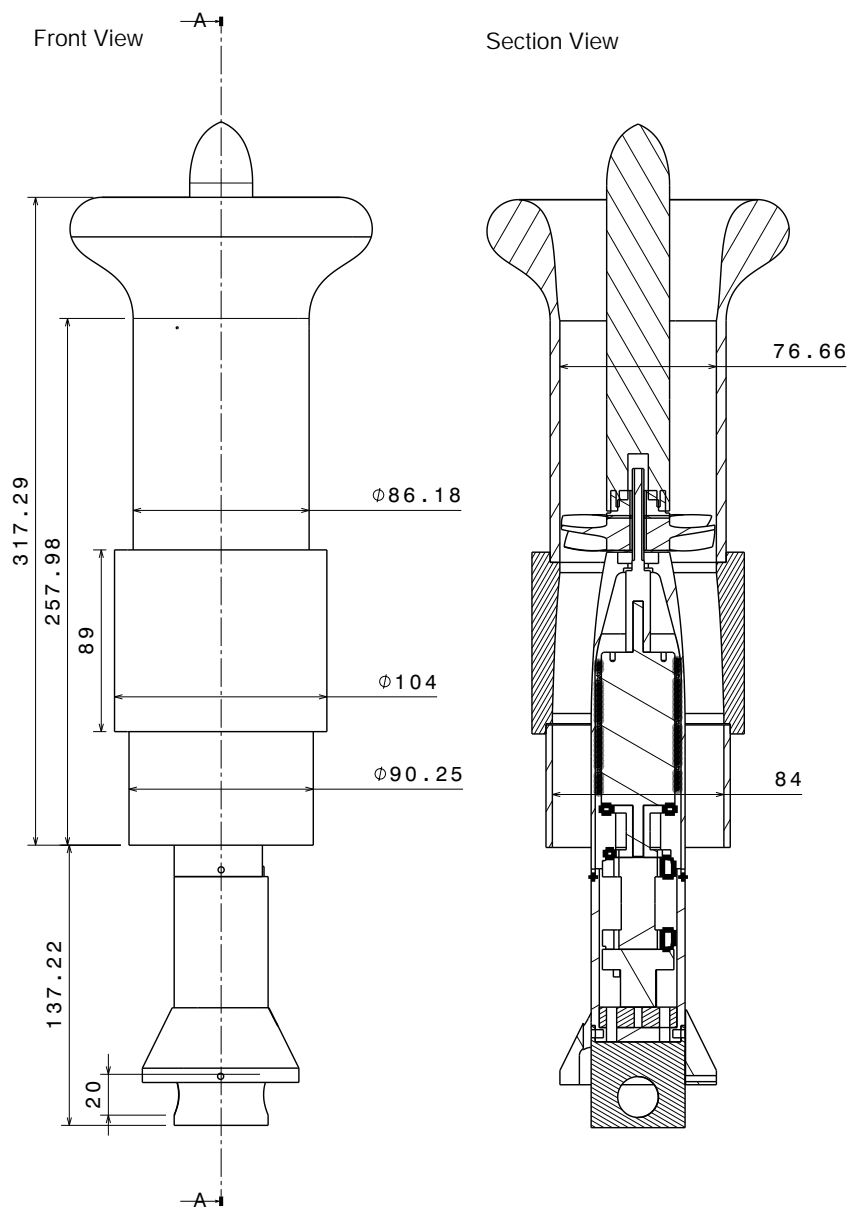


Figure A.9: Improvement in maximum achievable flow coefficient per recommendation.

B

Isolated Fan Test Rig Schematics



C

Enclosure Geometry

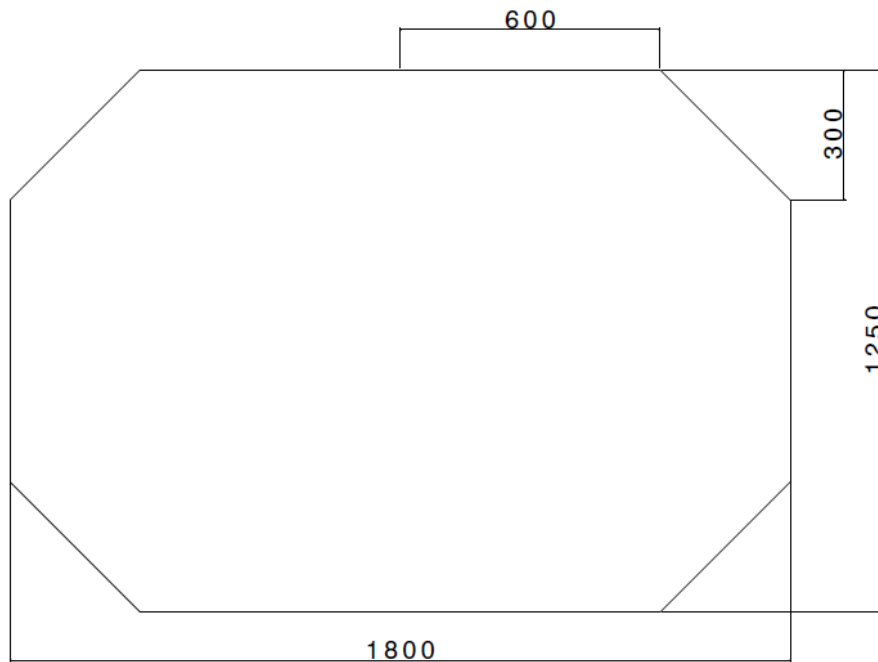


Figure C.1: Enclosure Inlet [mm].

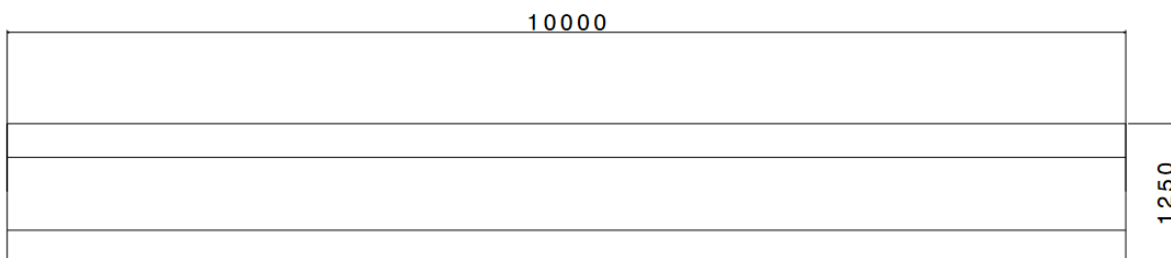


Figure C.2: Enclosure Side View [mm].

D

CFD Solver inputs

D.1. Default constants Spalart - Allmaras method

$$c_{b_1} = 0.1355$$

$$\sigma = 2/3$$

$$c_{b_2} = 0.622$$

$$k = 0.41$$

$$c_{w_1} = c_{b_1} / k + (1 + c_{b_2}) / \sigma$$

$$c_{w_2} = 0.3$$

$$c_{w_3} = 2$$

$$c_{v_1} = 7.1$$

$$c_{t_1} = 1$$

$$c_{t_2} = 2$$

$$c_{t_3} = 1.1$$

$$c_{t_4} = 2$$

$$g_t = \min(0.1, \frac{\Delta U}{\omega_t} \Delta x)$$

D.2. Default constants $k - \omega$ SST method

$$\sigma_{k_1} = 0.85$$

$$\sigma_{\omega_1} = 0.5$$

$$\beta_1 = 0.0750$$

$$a_1 = 0.31$$

$$\beta^* = 0.09$$

$$k = 0.41$$

$$\gamma_1 = \frac{\beta_1}{\beta^*} - \frac{\sigma_{\omega_1} k_1^2}{\sqrt{\beta^*}}$$

D.3. Default constants improved $k - \omega$ method

$$v_t = \frac{k}{\omega}$$

$$\beta^8 = \beta_0^* f_b$$

$$\beta = \beta_0 f_\beta$$

$$f_\beta = \frac{1 + 70 \chi_\omega}{1 + 80 \chi_\omega}$$

$$\chi_\omega = \left| \frac{\Omega_{ij} \Omega_{jk} S_{ki}}{(\beta_0^* \omega)^3} \right|$$

$$\chi_k = \frac{1}{\omega^3} \frac{\delta k}{\delta x_j} \frac{\delta \omega}{\delta x_j}$$

$$f\beta^* = \begin{cases} 1 & \text{if } \chi_k \leq 0 \\ \frac{1+680\chi_k^2}{1+400\chi_k^2} & \text{if } \chi_k \geq 0 \end{cases}$$

$$\alpha = 0.52$$

$$\beta_0^* = 0.09$$

$$\beta_0 = 0.072$$

$$\sigma^* = 0.5$$

$$\sigma = 0.5$$

$$F_1 = \tanh(\arg_1)$$

$$\arg_1 = \min \left[\max \left(\frac{\sqrt{k}}{0.09\omega y}, \frac{500\nu}{y^2\omega}, \frac{y\rho\sigma k}{CD_{k\omega}y^2} \right) \right]$$

E

Normalization Verification

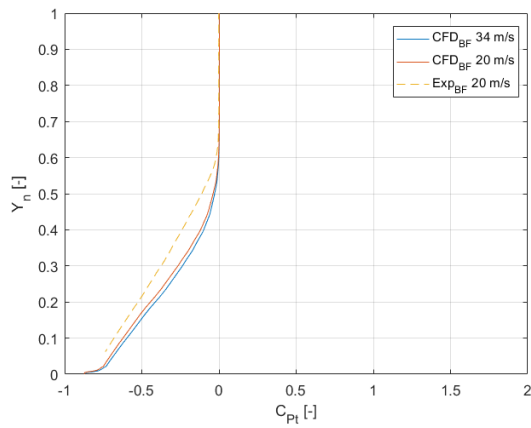


Figure E.1: Difference due to normalization in C_{P_t} , bare fuselage.

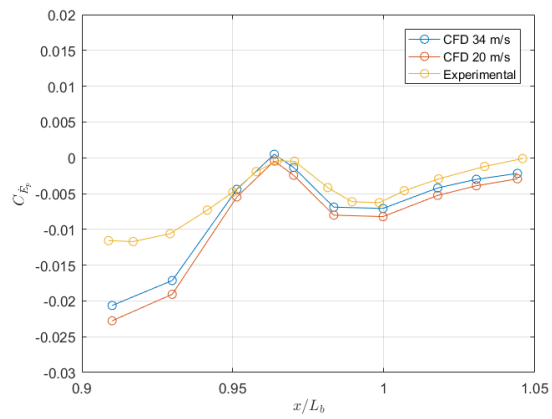


Figure E.2: Difference due to normalization in C_{E_p} , bare fuselage.

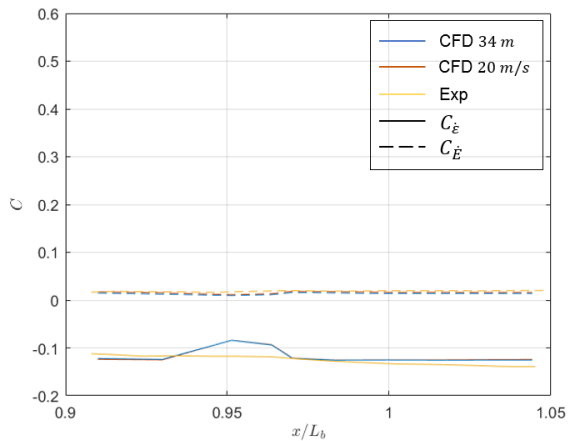


Figure E.3: Difference due to normalization in C_E and $C_{\tilde{E}}$, bare fuselage.

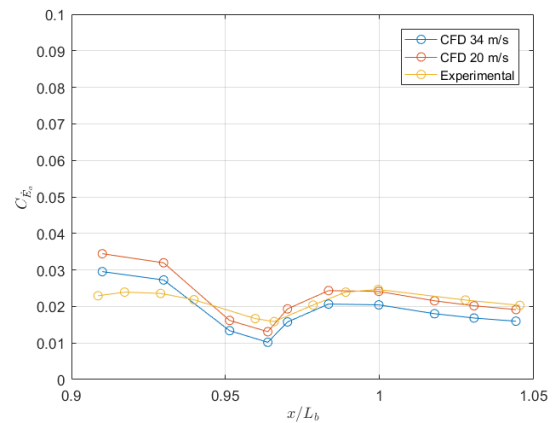


Figure E.4: Difference due to normalization in C_{E_a} , bare fuselage.

F

Numerical Flow Visualization

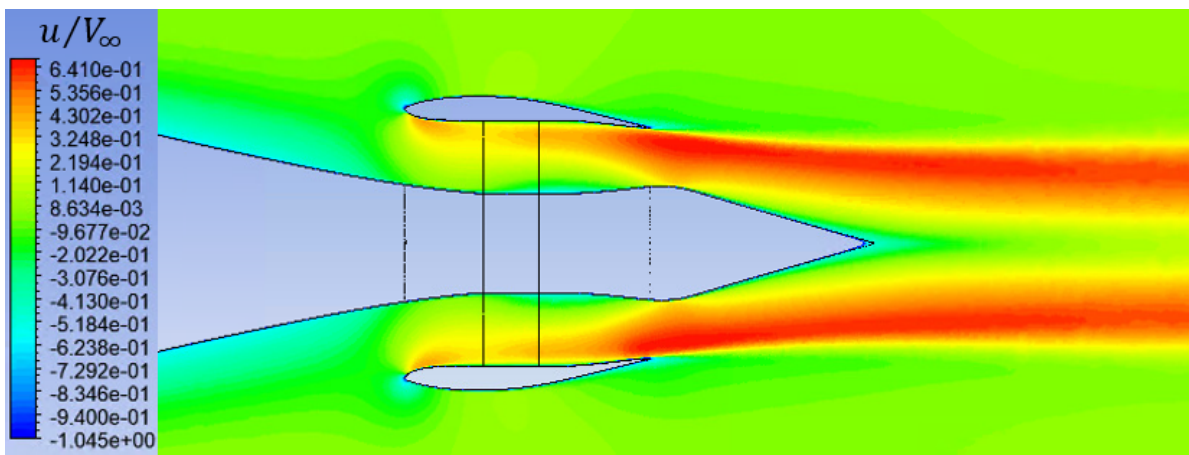


Figure E1: Contour plot of $\frac{u}{V_\infty}$ at $\phi = 0.5$.

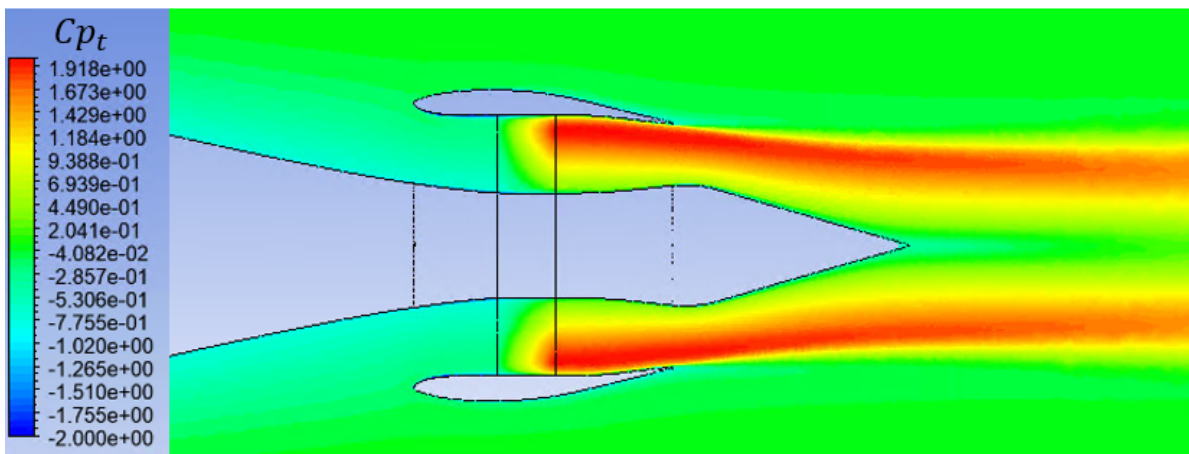


Figure E2: Contour plot of C_{p_t} at $\phi = 0.5$.

Bibliography

- [1] ACARE. Protecting the environment and the energy supply, June 2019. URL <https://www.acare4europe.org/sria/flightpath-2050-goals/protecting-environment-and-energy-supply-0>.
- [2] J. D. Anderson. *Fundamentals of Aerodynamics*. Mc Graw Hill, 5th si edition, 2011. ISBN 978-1-259-01028-6.
- [3] Ansys. Skewness, 2019. URL <https://ansyshelp.ansys.com/account/secured?returnurl=/Views/Secured/corp/v194/wb{ }msh/msh{ }skewness.html?q=skewness>.
- [4] Ansys. Othogonal Quality, 2019. URL <https://ansyshelp.ansys.com/account/secured?returnurl=/Views/Secured/corp/v194/wb{ }msh/msh{ }orthogonal{ }quality.html?q=orthogonal>.
- [5] Ansys. 4.2.4. Modeling the Turbulent Production, 2019. URL <https://ansyshelp.ansys.com/account/secured?returnurl=/Views/Secured/corp/v194/flu{ }th/flu{ }th{ }sec{ }spal{ }turb{ }prod.html>.
- [6] ANSYS. 4.18. Curvature Correction for the Spalart-Allmaras and Two-Equation Models, 2021. URL <https://ansyshelp.ansys.com/account/secured?returnurl=/Views/Secured/corp/v211/en/flu{ }th/flu{ }th{ }sec{ }curv{ }corr.html>.
- [7] Ansys. 8.4.2. Viscosity as a Function of Temperature, 2021. URL <https://ansyshelp.ansys.com/account/secured?returnurl=/Views/Secured/corp/v211/en/flu{ }ug/x1-7350009.4.2.html?q=sutherland>.
- [8] A. Arntz, O. Atinault, and D. Destarac. Numerical Airframe Aerodynamic Performance Prediction : An Exergy Point of View. *49th International Symposium of Applied Aerodynamics*, pages 1–10, 2014.
- [9] A. Arntz, O. Atinault, and A. Merlen. Exergy-Based Formulation for Aircraft Aeropropulsive Performance Assessment: Theoretical Development. *AIAA Journal*, 53(6):1627–1639, 2014. ISSN 0001-1452. doi: 10.2514/1.j053467.
- [10] O. Atinault, G. Carrier, R. Grenon, and C. Verbecke. Numerical and Experimental Aerodynamic Investigations of Boundary Layer Ingestion for Improving Propulsion Efficiency of Future Air Transport. (June 2013), 2013. doi: 10.2514/6.2013-2406.
- [11] P. Baskaran. *Aero-propulsive performance analysis of fuselage for boundary layer ingestion*. MSc thesis, TU Delft, 2019.
- [12] A. Betz. *Introduction to the theory of flow machines*. Pergamon Press, 1966.
- [13] B. T. Blumenthal, A. A. Elmilgui, K. A. Geiselhart, R. L. Campbell, M. D. Maughmer, and S. Schmitz. Computational investigation of a boundary-layer ingesting propulsion system for the common research model. *46th AIAA Fluid Dynamics Conference*, (June):1–33, 2016. doi: 10.2514/6.2016-3812.

- [14] A. Chaves. *Application of Power Balance Method to CFD*. MSc thesis, TU Delft, 2021.
- [15] B. Della Corte, A.A.V. Perpignan, M. Van Sluis, and A. Gangoli Rao. Experimental and Computational Analysis of Model – Support Interference in Low-Speed Wind-Tunnel Testing of Fuselage-Boundary-Layer Ingestion. 2019.
- [16] M. Darecki, C. Edelstenne, T. Enders, E. Fernandez, P. Hartman, J. Herteman, M. Kerkloh, I. King, P. Ky, M. Mathieu, G. Orsi, G. Schotman, C. Smith, and J. Wörner. Flightpath 2050. *Flightpath 2050 Europe's Vision for Aviation*, page 28, 2011. doi: 10.2777/50266. URL <http://ec.europa.eu/transport/modes/air/doc/flightpath2050.pdf>.
- [17] B. Della Corte, M. van Sluis, L.L.M. Veldhuis, and A. Gangoli Rao. Power Balance Analysis Experiments on an Axisymmetric Fuselage with Integrated Boundary-Layer-Ingesting Fan. *AIAA*, 2021.
- [18] S.L. Dixon and C.A. Hall. *Fluid Mechanics and Thermodynamics of Turbomachinery*. Butterworth-Heinemann, 6 edition, 2010. ISBN 978-1-85617-793-1.
- [19] Centerline Project EU. retrieved may, 2019. URL <https://www.centreline.eu/innovation/>.
- [20] K. A. Geiselhart, D. L. Daggett, R. Kawai, and D. Friedman. Blended wing body systems studies: boundary layer ingestion inlets with active flow control. *Nasa/Cr*, 212670(December), 2003.
- [21] J. E. Giuliani and J. Chen. Fan Response to Boundary-Layer Ingesting Inlet Distortions. *AIAA Journal*, 54(10):3232–3243, 2016. ISSN 0001-1452. doi: 10.2514/1.j054762. URL <https://doi.org/10.2514/1.J054762>.
- [22] F. Goetten, D. Felix, M. Marino, C. Bil, M. Havermann, and C. Braun. A review of guidelines and best practices for subsonic aerodynamic simulations using RANS CFD. *11th Asia-Pacific International Symposium of Aerospace Technology*, (December):227–245, 2019.
- [23] E.M. Greitzer, C.S. Tan, and M.B. Graf. *Internal Flow, concepts and applications*. Number SGEM2016 Conference Proceedings, ISBN 978-619-7105-16-2 / ISSN 1314-2704. Cambridge University Press, 2004. ISBN 978052134393.
- [24] E. J. Gunn and C. A. Hall. Aerodynamics of boundary layer ingesting fans. *Proceedings of the ASME Turbo Expo*, 1A:1–13, 2014. doi: 10.1115/GT2014-26142.
- [25] D. K. Hall, A. C. Huang, A. Uranga, E. M. Greitzer, M. Drela, and S. Sato. Boundary Layer Ingestion Propulsion Benefit for Transport Aircraft. *Journal of Propulsion and Power*, 33(5):1118–1129, 2017. ISSN 0748-4658. doi: 10.2514/1.B36321. URL <https://doi.org/10.2514/1.B36321><https://arc.aiaa.org/doi/10.2514/1.B36321>.
- [26] L. Hardin, G. Tillman, O. Sharma, J. Berton, and D. Arend. Aircraft System Study of Boundary Layer Ingesting Propulsion. Number August, pages 1–12, 2012. doi: 10.2514/6.2012-3993.
- [27] T. Hartuc. *Boundary Layer Ingestion, Theoretical and Experimental Research*. Literature survey, TU Delft, 2015.
- [28] S. Hickel. CFD I Lecture 5 - RANS, 2017. URL <https://brightspace.tudelft.nl/d21/1e/content/133552/viewContent/1044780/View>.
- [29] K. Hünecke. *Jet Engines*. The Crowood Press Ltd, 1997. ISBN 978 1 85310 834 1.

- [30] G. K. Kenway and C. C. Kiris. Aerodynamic Shape Optimization of the STARC-ABL Concept for Minimal Inlet Distortion. Number January, 2018. doi: 10.2514/6.2018-1912.
- [31] A. R. Kulkarni, G. La Rocca, and L. L.M. Veldhuis. Degree of similitude estimation for sub-scale flight testing. *AIAA Scitech 2019 Forum*, 2019. doi: 10.2514/6.2019-1208.
- [32] D. Hue R. Grenon B. Paluch L. Wiart, O. Atinault. Development of nova aircraft configurations for large engine integration studies, 2015. URL http://wpage.unina.it/fabrnico/SCAD2015/presentations/Atinault_Onera_SCAD2015.pdf.
- [33] B. J. Lee, M. S. Liou, and C. Kim. Optimizing a boundary-layer-ingestion offset inlet by discrete adjoint approach. *AIAA Journal*, 48(9):2008–2016, 2010. ISSN 00011452. doi: 10.2514/1.J050222. URL <https://doi.org/10.2514/1.J050222>.
- [34] R. H. Liebeck. Design of the Blended Wing Body Subsonic Transport. *Journal of Aircraft*, 41(1): 10–25, 2004. ISSN 00218669. doi: 10.2514/1.9084. URL <https://doi.org/10.2514/1.9084>.
- [35] C. Liu, E. Valencia, and J. Teng. Design point analysis of the turbofan-driven turboelectric distributed propulsion system with boundary layer ingestion. 230(6):1139–1149, 2016. doi: 10.1177/0954410015605546.
- [36] P. Lv. *Theoretical and Experimental Investigation of Boundary Layer Ingestion for Aircraft Application*. PhD thesis, 2019.
- [37] P. Lv and A. Rao. Conceptual Analysis of Boundary Layer Ingestion Towards Aircraft Propulsion Integration. *AIAA*, pages 1–15, 2013.
- [38] M. Drela. Power Balance in Aerodynamic Flows. *AIAA Journal*, 47(7):1761–1771, 2009. doi: 10.2514/1.42409.
- [39] F. R. Menter. Two-Equation Eddy-Viscosity Turbulence Models for Engineering Applications. 32(8), 1994. doi: 10.2514/3.12149. URL <https://doi.org/10.2514/3.12149>.
- [40] NASA. Air Viscosity; Sutherland’s Formula, 2014. URL <https://www.grc.nasa.gov/WWW/BGH/viscosity.html>.
- [41] A. C. Pardo and C. A. Hall. Aerodynamics of Boundary Layer Ingesting Fuselage Fans. *ISABE*, (ISABE-2019-24162), 2019.
- [42] A. Plas, M.A. Saregant, V. Madani, D. Chrichton, E.M. Greitzer, T.P. Hynes, and C.A. Hall. Performance of a Boundary Layer Ingesting Propulsion System. In *Archives*, number January, page 114, 2007. ISBN 1563478900. doi: doi:10.2514/6.2007-450. URL <http://dspace.mit.edu/handle/1721.1/35568>.
- [43] A. Plas, D. Crichton, M. Sargeant, T. Hynes, E. Greitzer, C. Hall, and V. Madani. Performance of a Boundary Layer Ingesting (BLI) Propulsion System. 2013. doi: 10.2514/6.2007-450.
- [44] L. Rosenhead. *Laminar Boundary Layers; An Account of the Development, Structure and Stability of Laminar Boundary Layers in Incompressible Fluids, together with a Description of the Associated Experimental Techniques*. Oxford at the Clarendon Press, 1963.
- [45] J. Roskam. Airplane Design Part II_ Preliminary Configuration Design and Integration of the Propulsion System (1997, DARcorporation), 1997.
- [46] S. Sato. *The Power Balance Method For Aerodynamic Performance Assessment*. PhD thesis, MIT, 2007.

- [47] M. Schobeiri. *Turbomachinery Flow Physics and Dynamic Performance*. Springer, 1 edition, 2005. ISBN 3-540-22368-1.
- [48] A. Seitz, F. Peter, J. Bijewitz, A. Habermann, Z. Goraj, M. Kowalski, A. C. Pardo, C. Hall, F. Meller, R. Merkle, O. Petit, S. Samuelsson, B. Della Corte, M. Van Sluis, G. Wortmann, and M. Dietz. Concept validation study for fuselage wake-filling propulsion integration. *31st Congress of the International Council of the Aeronautical Sciences, ICAS 2018*, 2018.
- [49] A. Seitz, A. Habermann, F. Peter, F. Troeltsch, A. C. Pardo, B. Della Corte, M. Van Sluis, Z. Goraj, M. Kowalski, X. Zhao, T. Gronstedt, J. Bijewitz, and G. Wortmann. Proof of Concept Study for Fuselage Boundary Layer Ingesting Propulsion. *Aerospace*, 2021. doi: <https://doi.org/10.3390/aerospace8010016>.
- [50] A. M. O. Smith and Howard E. Roberts. The Jet Airplane Utilizing Boundary Layer Air for Propulsion. *Journal of the Aeronautical Sciences*, 14(2):97–109, 1947. doi: 10.2514/8.1273.
- [51] L. Smith. Wake Ingestion Propulsion Benefit. page 10, Sacramento, 1991. AIAA. doi: AIAA-91-2007-CP.
- [52] P. R. Spalart and S. R. Allmaras. A One-Equation Turbulence Model for Aerodynamic Flows Boeing Commercial Airplane Group 30th Aerospace Sciences. *AIAA*, 30, 1992. doi: AIAA-92-0439.
- [53] P. R. Spalart and C. L. Rumsey. Effective Inflow Conditions for Turbulence Models in Aerodynamic Calculations. *AIAA Journal*, 45(10):2544–2552, 2007. doi: 10.2514/1.29373.
- [54] P. R. Spalart and M. Shur. On the Sensitization of Turbulence Models to Rotation and Curvature. *Aerospace Science and Technology*, 1(5):297–302, 1997. ISSN 12709638. doi: 10.1016/S1270-9638(97)90051-1.
- [55] S. Tambe, U. B. Oseguera, and A. Gangoli Rao. Performance of a Low Speed Axial Fan Under Distortion: An Experimental Investigation. In *ASME Turbo Expo 2020*, pages 1–11, 2020.
- [56] N. Uddin and J. T. Gravdahl. Two general state feedback control laws for compressor surge stabilization. *24th Mediterranean Conference on Control and Automation, MED 2016*, (June): 689–695, 2016. doi: 10.1109/MED.2016.7536063.
- [57] A. Uranga, M. Drela, E. M. Greitzer, D. K. Hall, N. A. Titchener, M. K. Lieu, N. M. Siu, C. Casses, A. C. Huang, G. M. Gatlin, and J. A. Hannon. Boundary Layer Ingestion Benefit of the D8 Transport Aircraft. *AIAA Journal*, 55(11):3693–3708, 2017. ISSN 0001-1452. doi: 10.2514/1.J055755. URL <https://arc.aiaa.org/doi/10.2514/1.J055755>.
- [58] N. van Arnhem, R. de Vries, R. Vos, and L. L. Veldhuis. Aerodynamic Performance of an Aircraft Equipped with Horizontal Tail Mounted Propellers. (June), 2019. doi: 10.2514/6.2019-3036.
- [59] R. Vos and S. Farokhi. *Introduction to Transonic Aerodynamics*. 2015. ISBN 9789401797467. doi: 10.1007/978-94-017-9747-4.
- [60] J. Welstead and J. L. Felder. Conceptual Design of a Single-Aisle Turboelectric Commercial Transport with Fuselage Boundary Layer Ingestion. Number January, page 17, 2016. doi: 10.2514/6.2016-1027.
- [61] J. Welstead, J. Felder, M. Guynn, B. Haller, S. Jones M. Tong, I. Ordaz, and B. Mason J. Quinlan. Overview of the nasa starc-abl (rev. b) advanced concept, 2017. URL <https://ntrs.nasa.gov/search.jsp?R=201700056122019-05-02T11:21:28+00:00Z>.

-
- [62] D. C. Wilcox. *Turbulence Modeling for CFD (First Edition)*. 1994. ISBN 0963605100.
- [63] Z. Yang, H. Lu, T. Pan, and Q. Li. Numerical Investigation on the Influences of Boundary Layer Ingestion on Tip Leakage Flow Structures and Losses in a Transonic Axial-Flow Fan. *Journal of Fluids Engineering*, 2021.
- [64] A. Yildirim, J.S. Gray, C.A. Mader, and J.R.R.A. Martins. Performance Analysis of Optimized STARC-ABL Designs Across the Entire Mission Profile. *AIAA SciTech Forum*, 2021.